UNIVERSITY OF CALIFORNIA
RIVERSIDE

Synthesis, Characterization and Performance of Cathodes for Lithium Ion Batteries

A Dissertation submitted in partial satisfaction
of the requirements for the degree of

Doctor of Philosophy

in

Materials Science and Engineering

by

Jianxin Zhu

March 2014

Dissertation Committee:

Dr. David Kisailus, Chairperson
Dr. Alexander Balandin
Dr. Mihri Ozkan

This Dissertation of Jianxin Zhu is approved:

Committee Chairperson

University of California, Riverside

Acknowledgements

First, I would like to express my heartiest gratitude and deep appreciation to my advisor Professor David Kisailus. He is a great mentor, has a generous personality, broad knowledge and supportive leadership, nurturing me towards my career goals. I am also thankful to my committee members Professor Alexander Balandin and Professor Mihri Ozkan for their help and advice on my dissertation. I would also like to thank Professor Juchen Guo for his collaborative help with battery performance. His generous help and expertise helped me to collect and analyze electrochemical performance data.

I am very thankful to many past and current members in Professor Kisailus' group for providing a rich working experience, intellectual stimulation and friendship: Dr. Dongsheng Li, Dr. Qianqian Wang, Dr. Nichola Kinsinger, Wenting Hou and Chris Salinas. Special thanks to the undergraduate students who have worked on this project, including Thinh Vo, Kim-Kim Nguyen, Richard Lu, Joseph Fiore, Anthony Michael Lira, Kevin Yoo, Akhila Denduluri, and Ibrahim El-halees.

I thank Dr. Krassimir N. Bozhilov, Stephen McDaniel and Mathias Rommelfanger for their kind assistance in using the facilities in CFAMM at UCR. I also want to thank Professor Javier Garay for allowing me to use his equipment (roller mill) during my research, Professor Alexander Balandin and Sylvester Ramirez for the thermal conductivity measurements, Professor Yushan Yan and Laj Xiong for the TGA/DSC data collection, Dr. IIkeun Lee for the XPS measurements, Dr. Sanjaya Senanayake and Dr. Wenqian Xu at Brookhaven National Laboratory for *in-situ* synchrotron XRD

experiments. My thanks also go to my friends Dr. Qiao Zhang, Dr. Tao Wu, Dr. Fan Zuo, Dr. Xiang Zhao, Dr. Rui Liu and Chengyin Fu for their valuable help.

Most importantly, none of this would have been possible without the love and patience of my family. I would like to express my heart-felt gratitude to my parents Xuecun Zhu and Dongyue Zhang, my parents-in-law Fanyou Guo and Aizhen Li, and my husband Shirui Guo for everything they have done for me.

Finally, I would like to take the opportunity to thank all persons who have ever helped me before.

Dedication

To my husband Shirui and my little princess Angela

ABSTRACT OF THE DISSERTATION

Synthesis, Characterization and Performance of Cathodes for Lithium Ion Batteries

by

Jianxin Zhu

Doctor of Philosophy, Graduate Program in Materials Science and Engineering
University of California, Riverside, March 2014
Dr. David Kisailus, Chairperson

Lithium ion batteries provide a high energy density, higher voltage as well as a long shelf life compared to traditionally used lead acid, NiMH and NiCd batteries. Thus, they are a very promising energy storage system for our daily life. As one of the most important components in a battery, cathode materials have been investigated intensively in recent years as they play a key role in determining the cell voltage and discharge capacity in a battery. Both layered $Li(Ni_{1/3}Co_{1/3}Mn_{1/3})O_2$ (NCM) and olivine-structured $LiFePO_4$ (LFP) materials are promising cathode candidates. However, these cathodes also have some disadvantages that have hindered further commercialization. The main issue with NCM is its rapid performance decay upon cycling. In addition, LFP is hindered by a low rate capacity and low lithium ion diffusivity.

We studied the crystal growth behavior and performance of both $Li(Ni_{1/3}Co_{1/3}Mn_{1/3})O_2$ and $LiFePO_4$ cathodes in order to develop synthesis-structure-function relationships. Three different crystal growth behaviors were observed for the NCM annealing process: surface, volume and grain boundary diffusion. Further exploration of the mechanism of NCM performance decay revealed that microstructural changes were related to the strain accommodation ability in this system and that

nanostructured materials were more stable during cycling. In the LFP synthesis, we observed both oriented attachment (OA) and Ostwald ripening (OR) during growth in a triethylene-glycol system. Both polycrystalline and single crystalline particles evolved as a function of a time-dependent pH change. Thus, the lithium ion diffusion rate of $LiFePO_4$ was improved by tailoring the morphology and size though our modification of the precursor environment, revealing that polycrystalline LFP displayed better performance than single crystalline particles. Finally, the electronic conductivity of $LiFePO_4$ was successfully increased via a polymer solution coating method. By producing more uniform, thin and coherent coatings on $LiFePO_4$ particles, we were able to produce batteries with significantly less carbon (i.e., 0.41 wt.%) while has comparable performance (discharge capacity of 80mAh/g at 2C) compared to traditionally synthesized carbon-coated $LiFePO_4$ with higher carbon loadings (ca. 2.64 wt.%). This will enable us to produce batteries with higher active material loading and therefore, significantly larger energy densities.

TABLE OF CONTENTS

Acknowledgements iv

Dedication vi

ABSTRACT OF THE DISSERTATION vii

TABLE OF CONTENTS ix

Chapter 1. 1

Introduction 1

1.1 History of batteries 2

1.2 Lithium ion batteries 5

1.2.1 Basic concepts of lithium ion batteries 5

1.2.2 Materials used in lithium ion batteries 7

1.3 Anode materials used in lithium ion batteries 9

1.4 Cathode materials used in lithium ion batteries 13

1.4.1 Layered structures 14

1.4.2 Spinel structures 17

1.4.3 Olivine structures 19

1.4.4 Other types 24

1.5 Objectives 26

1.5.1 Specific objectives for NCM 27

1.5.2 Specific objectives for $LiFePO_4$ 28

Chapter 2. 30

Crystal Growth of $Li[Ni_{1/3}Co_{1/3}Mn_{1/3}]O_2$ as a Cathode Material for High-Performance Lithium Ion Batteries 30

2.1. Introduction 31

2.2. Experimental Section 33

2.3. Results and Discussion 35

2.3.1 XRD 35

2.3.2 TGA-DSC 38

2.3.3 Microstructural Analysis 39

2.4. Growth Mechanisms 44

2.5. Conclusions 48

Chapter 3. 50

Crystal Structure and Size Effect on the Performance Degradation of $Li[Ni_{1/3}Co_{1/3}Mn_{1/3}]O_2$ as a Cathode Material for Lithium Ion Batteries 50

3.1. Introduction 51

3.2. Experimental Section 53

3.2.1 Material synthesis 53

3.2.2 Material characterization 53

3.2.3 Electrochemical performance 54

3.3. Results and Discussion 55

3.3.1 Characterization of synthesized $Li[Ni_{1/3}Co_{1/3}Mn_{1/3}]O_2$ 55

3.3.2 Electrochemical performance 58

3.3.3 Discussion of performance degradation..... 62

3.4. Conclusions..... 68

Chapter 4. 70

Solvothermal Synthesis, Development and Performance of..... 70

$LiFePO_4$ Nanostructures 70

4.1 Introduction..... 72

4.2 Experimental Section..... 74

4.2.1 Synthesis of lithium iron phosphate..... 74

4.2.2 Material characterization 75

4.2.3 Electrochemical performance 75

4.3 Results and Discussion 76

4.3.1 Formation and nanostructural evolution of $LiFePO_4$..... 76

4.3.1.1 Precursor..... 76

4.3.1.2 Formation of $Fe_3(PO_4)_2 \cdot 8H_2O$ (vivianite, VTE) and nucleation of $LiFePO_4$... 77

4.3.1.3 Oriented assembly of polycrystalline $LiFePO_4$ (LFP) particles. 81

4.3.1.4. Ostwald ripening of polycrystalline LFP 84

4.3.1.5 Development of single crystalline LFP 87

4.3.2 Electrochemical performance 89

4.4 Conclusions 92

4.5 Acknowledgement 93

Chapter 5. 94

Conformal Carbon Coating of $LiFePO_4$ via 94

Polymer Solution Method 94

5.1 Introduction 96

5.2 Experimental Section 98

5.2.1 Annealing of $LiFePO_4$ powders 98

5.2.2 Synthesis of carbon-coated $LiFePO_4$ 98

5.2.3 Material characterization 99

5.2.4 Electrochemical performance 100

5.3 Results and Discussion 101

5.3.1 Annealing parameters investigation 101

5.3.1.1 Pristine $LiFePO_4$ annealing study 101

5.3.1.2 PEG and sucrose annealing study 105

5.3.2 Carbon-coated $LiFePO_4$ from PEG (sample A) 108

5.3.2.1 Mixture of PEG solution and $LiFePO_4$ suspension 108

5.3.2.2 Carbon-coated LFP from PEG 109

5.3.3 Carbon-coated $LiFePO_4$ from sucrose (sample B) 111

5.3.4 Electrochemical performance of $LiFePO_4$ 115

5.3.4.1 CV curve 115

5.3.4.2 Charge/discharge capacities 117

5.4 Conclusions 118

Chapter 6. 120

Conclusions 120

References 126

LIST OF FIGURES

Figure 1. Schematic of a copper-zinc voltaic pile. The copper and zinc were separated by cardboard..... 3

Figure 2. Ragone plot showing energy density and power density for various electrical energy storage devices.[4] 5

Figure 3. Illustration of the working principle of a lithium ion battery using $LiCoO_2$ as the cathode and graphite as the anode. 6

Figure 4. Structure of a prismatic lithium ion cell. 8

Figure 5. Specific capacity comparison among different anode materials for lithium ion battery[6] 10

Figure 6. (a) Crystal structure of $LiCoO_2$ having the O3 layered structure;[12] (b) Drawn with lithium ions horizontally between CoO_2 octahedra, lattice parameters a= b= 2.8138 Å and c= 14.0516 Å. (c) Projection along the [110] zone axis shows lithium, cobalt and oxygen atoms in columns.[30] 15

Figure 7. Crystal structure of spinel $LiMn_2O_4$ (blue: oxygen ions; brown: lithium ions; green: manganese ions). 18

Figure 8. Crystal structure of spinel $LiFePO_4$. It contains FeO_6, LiO_6 octahedra and PO_4 tetrahedra..... 20

Figure 9. Voltage in various phosphates versus gravimetric capacity. The blue dashed lines are the energy density curves at 600 and 800 Wh/kg. The red dashed line indicates the upper voltage considered as safe area against electrolyte decomposition.[93] 21

Figure 10. Curved trajectories for Li ion migration between sites in the [010] direction The diffusion path lies out of the x-y plane.[98] 22

Figure 11. Ideal olivine structure shows M1 and M2 sites. M1 is the smaller site and M2 is the bigger site. 23

Figure 12. Crystal structure of a typical tavorite-structured material, $LiFe(PO_4)F$. Brown FeO_6 octahedra, yellow PO_4 tetrahedra, red spheres: O, and blue spheres: F. The green-and-white spheres represent partially occupied lithium sites, with the occupancy given by the fraction of the sphere shaded green.[28] 25

Figure 13. Crystal structure of the silicate Li_2FeSiO_4, Li ions at sites 1, 2, 3 and 4 are labeled and colored differently.[107] 26

Figure 14. Schematic of $LiNi_{1/3}Co_{1/3}Mn_{1/3}O_2$ two steps (co-precipitation and annealing method) synthesis..... 34

Figure 15. XRD pattern of $[Ni_{1/3}Co_{1/3}Mn_{1/3}](OH)_2$ precursor..... 35

Figure 16. XRD patterns of $Li[Ni_{1/3}Co_{1/3}Mn_{1/3}]O_2$ heated for 12 hours at (a) 200°C, (b) 300°C, (c) 400°C, (d) 500°C, (e) 600°C, (f) 700°C, (g) 800°C, and (h) 900°C. 36

Figure 17. TGA-DSC of the mixture of $[Ni_{1/3}Co_{1/3}Mn_{1/3}](OH)_2$ and $LiOH \cdot H_2O$..... 39

Figure 18. SEM micrographs of $Li[Ni_{1/3}Co_{1/3}Mn_{1/3}]O_2$ annealed at (A) 600°C, (B) 700°C, (C) 800°C, (D) 900°C, (E) 950°C, (F) 1000°C for 3 hours with an EDS spectrum (bottom) from Sample (C). 41

Figure 19. Crystal diameters of L333 annealed for 3 hours at temperatures from 600°C – 1000°C. 3 separate growth regions are observed. 43

Figure 20. Bright-field TEM micrographs of $Li[Ni_{1/3}Co_{1/3}Mn_{1/3}]O_2$ annealed at 800°C for (A) 0.5 hour, (B) 1 hour, (C) 3 hours, and (D) 6 hours. Fast fourier transforms are inserted in (A) and (C). 44

Figure 21. Relationship between crystal diameter and annealing time for samples annealed in air from 700°C to 1000°C..... 46

Figure 22. XRD pattern of $Li[Ni_{1/3}Co_{1/3}Mn_{1/3}]O_2$ annealed in air at (A) 750°C, (B) 850°C, (C) 950°C, (D) 1000°C for 3 hours..... 56

Figure 23. SEM micrographs of $Li[Ni_{1/3}Co_{1/3}Mn_{1/3}]O_2$ annealed in air at (A) 750 °C, (B) 850 °C, (C) 950 °C, (D) 1000 °C for 3 hours. 58

Figure 24. CV profiles of $Li[Ni_{1/3}Co_{1/3}Mn_{1/3}]O_2$ (annealed in air at various temperatures) in the voltage range of 2.8-4.5V at a scan rate of 0.1mV/s..... 59

Figure 25. Initial charge/discharge profiles of $Li[Ni_{1/3}Co_{1/3}Mn_{1/3}]O_2$ samples at $16mAg^{-1}$ (synthesized at different annealing temperatures) in the voltage range 2.8-4.5V. ... 60

Figure 26. Cycling performance of $Li[Ni_{1/3}Co_{1/3}Mn_{1/3}]O_2$ cathodes between 2.8 and 4.5V (vs. Li^+/Li) (A) at different current rates (0.1C, 0.2C, 0.5C, 1C and 2C), (B) at 0.1C for 50 cycles. 62

Figure 27. SEM micrographs of $Li[Ni_{1/3}Co_{1/3}Mn_{1/3}]O_2$ cathode particles, annealed in air at (A) 750°C, (B) 850°C, (C) 950°C, (D) 1000°C, and removed from cells after 50 cycles..... 63

Figure 28. XRD pattern comparison of $Li[Ni_{1/3}Co_{1/3}Mn_{1/3}]O_2$ samples annealed in air at: A 750°C, B 850°C, C 950°C, D 1000°C before (blue) and after (black) cycling. ... 64

Figure 29. EIS micrographs of $Li[Ni_{1/3}Co_{1/3}Mn_{1/3}]O_2$ cathodes after 50 cycles for samples annealed in air at: A 750°C, B 850°C, C 950°C, D 1000°C. 68

Figure 30. (A) SEM micrograph and (B) XRD pattern of precursor sample indicating the formation of Li_3PO_4 nanocrystals. 76

Figure 31. Characterization of the sample synthesized at 160°C for 5 minutes. (A) SEM of the platelet structure, (B) Powder XRD of sample with $Fe_3(PO_4)_2 \cdot 8H_2O$ as a reference, (C) Synchrotron x-ray diffraction of the sample, confirming the VTE phase with little LFP phase (D) Bright-field TEM of the platelet structure (E) Bright-field TEM of the platelet structure with small particles on top (upper left inset), highlighting LFP nanoparticles forming at edges of $Fe_3(PO_4)_2 \cdot 8H_2O$), (G) SAED from clean platelet (green square area) (H) SAED from combination of platelet and nanoparticles (circled blue area), and (I) SAED from completely formed primary particle tail (circled purple area). 79

Figure 32. *In-situ* synchrotron monitoring of the phase transformation from $Fe_3(PO_4)_2 \cdot 8H_2O$ (VTE) to $LiFePO_4$ (LFP). 80

Figure 33. Analyses of $LiFePO_4$ synthesized at 160°C for 10 minutes in a sealed glass reactor. (A) SEM micrograph highlighting the assembled secondary particles of LFP. (B) Powder XRD of sample, (C) Bright field TEM with corresponding (D) SAED from the yellow-circled area. 82

Figure 34. Characterization of $LiFePO_4$ synthesized at 160°C for 10 minutes in a sealed glass reactor. (A) Zeta potential analysis of LFP particles, (B) Bright field TEM

showing c and a directions of particles, (C) HRTEM from yellow circle highlighted in (C), and (D) the corresponding FFT. 84

Figure 35. (A) SEM image of LFP particles synthesized in a sealed glass reactor at 160°C for 10 minutes and (B) the corresponding XRD pattern, (C) SEM image of LFP particles synthesized in a Teflon-liner reactor at 160°C for 10 minutes and (D) the corresponding XRD pattern. 85

Figure 36. SEM micrographs of LFP products at 160°C with increasing duration. (A) After 10 minutes, LFP formation and assembly into secondary particles is completed. Increasing reaction duration to (B) 60 minutes, (C) 420 minutes, and (D) 900 minutes yields more crystalline LFP..... 86

Figure 37. Analysis of single crystalline $LiFePO_4$ synthesized at 160°C for 900 minutes. (A) SEM of powder sample highlighting size and morphological features, (B) XRD pattern confirming pure $LiFePO_4$, (C) Bright field TEM micrograph of a $LiFePO_4$ particle, and (D) the corresponding SAED from (C), confirming its single crystalline nature..... 88

Figure 38. (A) Reaction time vs. solution pH with LFP formation information and (B) schematic of LFP nucleation, primary particles formation and single crystal evolution. 89

Figure 39. Electrochemical characterization of polycrystalline and single crystalline LFP. (A) CV profiles in the voltage range of 2.7-4.2 V at a scan rate of 0.2 mV/s, (B) Galvanostatic charge/discharge profiles and (C) Cycling performance at various current rates between 2.7 V and 4.2 V (vs. Li^+/Li). 91

Figure 40. The XPS of Fe 2p for LFP (A) synthesized at 10 and 900 minutes at 160°C, both indicating small concentrations of Fe^{3+} impurities. (B) fitted curve for sample synthesized for 10 minutes and (C) fitted curve for sample synthesized for 900 minutes. 92

Figure 41. Schematic of carbon coating on $LiFePO_4$ (A) pure $LiFePO_4$ without any carbon coating, (B) carbon coated $LiFePO_4$ with conventionally used mechanical method, and (C) carbon coated $LiFePO_4$ with precisely controlled method. 97

Figure 42. TGA/DSC of pristine $LiFePO_4$ from 25°C to 700°C at 20 cc/min flow rate in 95% N_2 / 5% H_2 with a 3 hour hold at 700°C. 102

Figure 43. XRD diffraction patterns for pristine $LiFePO_4$ annealed for 3 hours in 95% N_2 / 5% H_2 at: (A) 200°C, (B) 300°C, (C) 400°C, (D) 500°C, (E) 600°C, and (F) 700°C. 103

Figure 44. SEM micrographs of pristine $LiFePO_4$ annealed in 95% N_2 / 5% H_2 for 3 hours at: (A) 200°C, (B) 300°C, (C) 400°C, (D) 500°C, (E) 600°C, and (F) 700°C. 104

Figure 45. TGA/DSC curves for PEG and sucrose heated in 95% N_2 / 5% H_2 flowing at 20 cc/min. (A) PEG from 25°C to 700°C and held for 3 hours duration and (B) sucrose from room temperature to 600°C and held for 3 hours duration. 105

Figure 46. Raman spectroscopy of PEG annealed in 95% N_2 / 5% H_2 at 20cc/min for 3 hours duration at: (A) 400°C, (B) 500°C, (C) 600°C, and (D) 700°C. 107

Figure 47. Raman spectroscopy of sucrose annealed under 95% N_2 / 5% H_2 at 20 cc/min for 3 hours duration at: (A) 500°C, (B) 600°C. 108

Figure 48. SEM micrographs for solution-coated PEG on $LiFePO_4$ after magnetically stirring for 1 hour. 109

Figure 49. SEM micrographs for carbon-coated $LiFePO_4$ (from PEG) after annealing at 600°C for 3 hours in 95% N_2 /5% H_2 at 20 cc/min. 110

Figure 50. XRD diffraction pattern for carbon-coated $LiFePO_4$ (from PEG) after annealing at 600°C for 3 hours in 95% N_2 / 5% H_2 at 20 cc/min. 110

Figure 51. Raman spectroscopy of carbon-coated $LiFePO_4$ (from PEG) annealed at 600°C for 3 hours in 95% N_2 / 5% H_2 at 20 cc/min. 111

Figure 52. SEM micrographs for sucrose added $LiFePO_4$ mixture after annealing at 600°C for 3 hours in 95% N_2 / 5% H_2 at 20 cc/min. 112

Figure 53. XRD diffraction pattern for sucrose added $LiFePO_4$ after annealing at 600°C for 3 hours in 95% N_2 /5% H_2 at 20 cc/min. 113

Figure 54. Raman spectroscopy of sucrose added LFP annealed at 600°C for 3 hours in 95% N_2 / 5% H_2 at 20cc/min. 114

Figure 55. CV profiles of $LiFePO_4$ in the voltage range of 2.7-4.2 V at a scan rate of 0.1 mV/s for sample, (A) carbon coated $LiFePO_4$ using PEG as carbon source, (B) carbon coated $LiFePO_4$ using sucrose as carbon source, and (C) pure $LiFePO_4$ as control sample. 116

Figure 56. Discharge capacity vs. cycles for carbon coated $LiFePO_4$ using PEG as the carbon source, (A) cycling performance at 0.1C between 2.7 V and 4.2 V (vs. Li^+/Li) for 70 cycles, (B) discharge capacity retention. 117

Figure 57. Carbon-coated and carbon-free $LiFePO_4$ cycling performance at various current rates between 2.7 V and 4.2 V (vs. Li^+/Li), (A) carbon coated $LiFePO_4$ using PEG as carbon source, (B) carbon coated $LiFePO_4$ using sucrose as carbon source, and (C) pure $LiFePO_4$ as a control sample..... 118

LIST OF TABLES

Table 1. Metallic lithium phase, capacity and volume change information.[12] 12

Table 2 Summary of cathode and anode materials used for different types of lithium-ion batteries.[29] 14

Table 3. Calculated structure parameters for synthesized $Li[Ni_{1/3}Co_{1/3}Mn_{1/3}]O_2$. 38

Table 4. Grain growth parameters at different temperatures. 47

Table 5. Calculated lattice parameters of $Li(NiCoMn)_{1/3}O_2$. 57

Table 6. Specific capacities for $Li[Ni_{1/3}Co_{1/3}Mn_{1/3}]O_2$ cathodes annealed at various temperatures. 61

Table 7. Lattice parameters for $Li[Ni_{1/3}Co_{1/3}Mn_{1/3}]O_2$ cathodes after 50 cycles. 66

Table 8. Parameters from the EIS curves..... 66

Table 9. Reaction pH at different reaction durations (minutes)..... 83

Table 10. Structural Carbon Data from Annealed PEG and Sucrose Sources..... 107

Table 11. Crystal size and carbon content for samples A, B and C after heat-treatment at 600°C for 3hours. 115

Chapter 1.

Introduction

1.1 History of Batteries

Energy is important to all of us, for a variety of reasons, but mostly because it is useful in our daily life. And it's been well known that gaseous emissions from the burning of fossil fuels and biomass are not only polluting the air but also creating the global warming. Solar energy and wind energy are among the most abundant and potentially readily available renewable energy sources that are variable in time and diffuse in space.[1, 2] However, as we know, while renewable energy is plentiful, it is also fickle. The sun does not shine all the time and the wind blows sometimes too hard and sometimes not at all. Therefore, we need to store the energy when it can be made, so that we can use it when we need it. Thus, methods to store and transport energy from place to place, from time to time can be of great importance. The energy carriers are the electricity grid, electromagnetic waves, and chemical energy, among which the most convenient form of energy storage is portable chemical energy.[3] Electrochemical devices can be used as transducers between electrical and chemical energy conversion. Such electrochemical transduction systems are often called galvanic cells or batteries.

In 1798, Italian physicist Alessandro Volta made the first battery. His "voltaic pile", as it comes to be known, consists of stacks of zinc, acid-moistened cardboard and copper (Figure 1). Here oxidation occurs on the metals ("electrodes"), which creates electrons that are transferred down the pile via the saltwater paper (the "electrolyte"). Therefore a charge is introduced at one pole, which builds as electrons move down the pile.

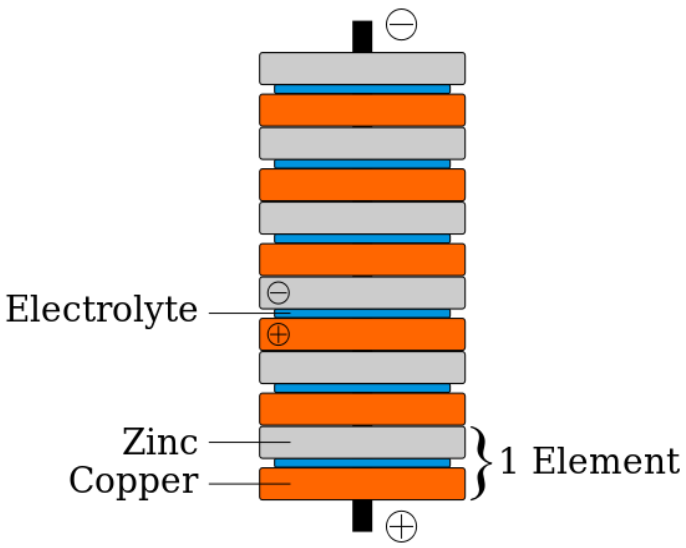

Figure 1. Schematic of a copper-zinc voltaic pile. The copper and zinc were separated by cardboard.

There were various batteries invented at this time, but they were all primary cells, so could not be recharged. In 1859, the French physicist Gaston Planté used conductor plates in dilute sulfuric acid, which led to the first rechargeable/secondary battery. So the initial secondary battery was lead-acid based, and it is still used to this day. Over the following decades, the lead battery underwent a number of significant further developments. Later, the first Ni–Cd battery, which is the first alkaline battery, was created by Waldemar Jungner of Sweden in 1899 and has been used for a long time. For many years, nickel-cadmium had been the only suitable battery for portable equipment from wireless communications to mobile computing until nickel-metal-hydride (NIMH) and lithium-ion emerged in the early 1990s. NIMH batteries tend to have longer lifespans than NiCd batteries (and their lifespans continue to increase as manufacturers experiment with new alloys) and since cadmium is toxic, NiMH batteries are less damaging to the environment.

Lithium batteries were used as early as 1912 under G.N. Lewis, but it was not until the early 1970s when the first primary lithium batteries became commercially available. As the lightest of all metals, lithium has the highest theoretical capacity (3,829 mAh/g) and has the greatest electrochemical potential and provides the largest gravimetric energy density. However, attempts to develop rechargeable lithium batteries failed because of safety issues, which were caused by the inherent instability of lithium metal (especially during charging process). Therefore, researchers shifted to use lithium ions instead of lithium metal. Though the lithium ion battery has a slightly lower energy density than lithium metal, it is safe, which makes it practical to be a secondary battery. In 1991, Sony commercialized the first lithium-ion battery.

Compared to the other batteries, lithium ion batteries provide high energy density, (160% greater than NiMH and 220% greater than NiCd, Figure 2). The voltage is higher (above 3V) compared to NiMH and NiCd batteries (with an operating voltage of 1.2 V). For example, the high cell voltage of 3.6 V (using $LiCoO_2$ and carbon as electrodes) allows battery pack designs with only one cell. Thus, using a Ni-based pack, it would require three 1.2-volt cells connected in series. Moreover, Li-ion batteries have a long shelf-life (only 5% discharge loss per month), versus 10% for NiMH and 20% for NiCd batteries.

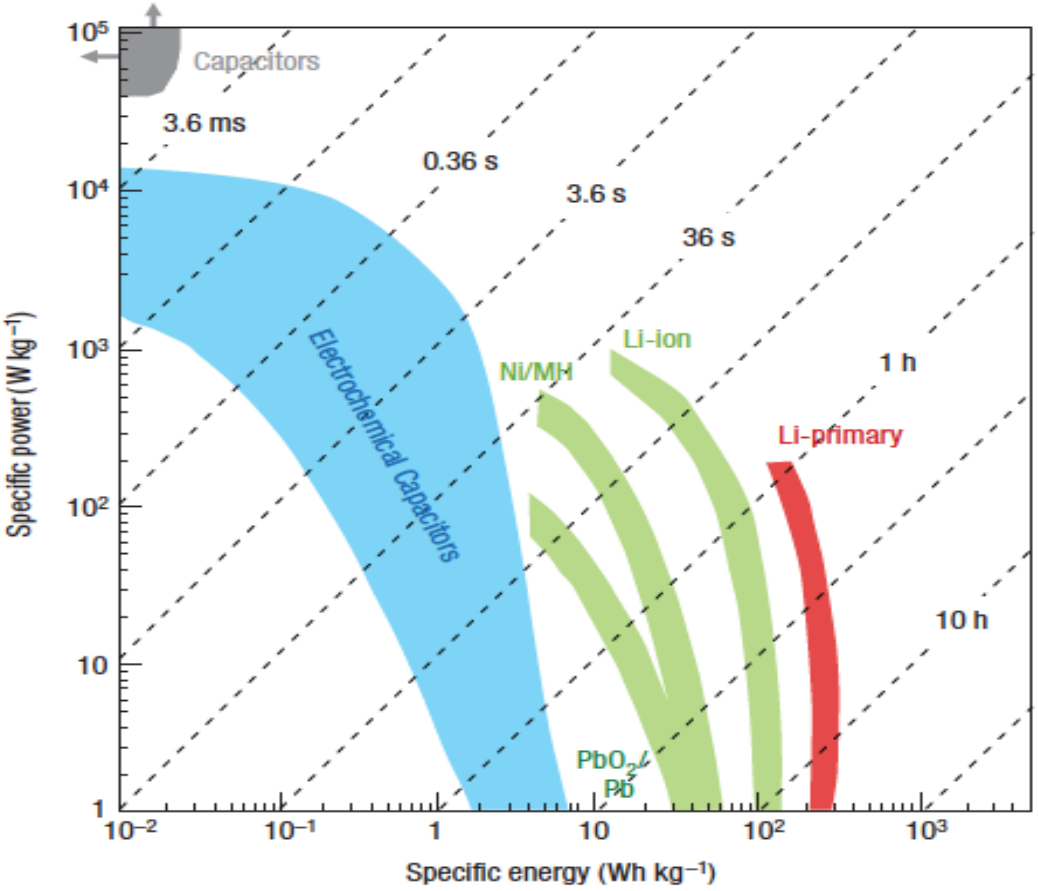

Figure 2. Ragone plot showing energy density and power density for various electrical energy storage devices.[4]

1.2 Lithium ion batteries

1.2.1 Basic concepts of lithium ion batteries

As we mentioned earlier, a battery is a transducer between electrical and chemical energy conversion. The structure of a battery includes an anode, a cathode, a separator and the electrolyte. As a secondary battery, the lithium ion battery involves a reversible insertion/extraction of lithium ions into/from the host matrix. The anode is the source of lithium ions and the cathode is the sink for the lithium ions. The separator, as the name

implies, separates the positive and negative electrodes while allowing ions to pass through during lithium ion insertion/extraction. Thus the electrode system must have both good ionic and electronic conductivity. Figure 3 illustrates the working principle of lithium ion batteries.

When the battery charges, ions of lithium move through the electrolyte from the positive electrode (e.g., $LiCoO_2$) to the negative electrode (e.g., carbon). At the same time, electrons generated in the reaction go through the external circuit to charge the battery. During discharge, the lithium ions move back to the $LiCoO_2$ from the carbon while the electricity generated in the external circuit is used for device operation.

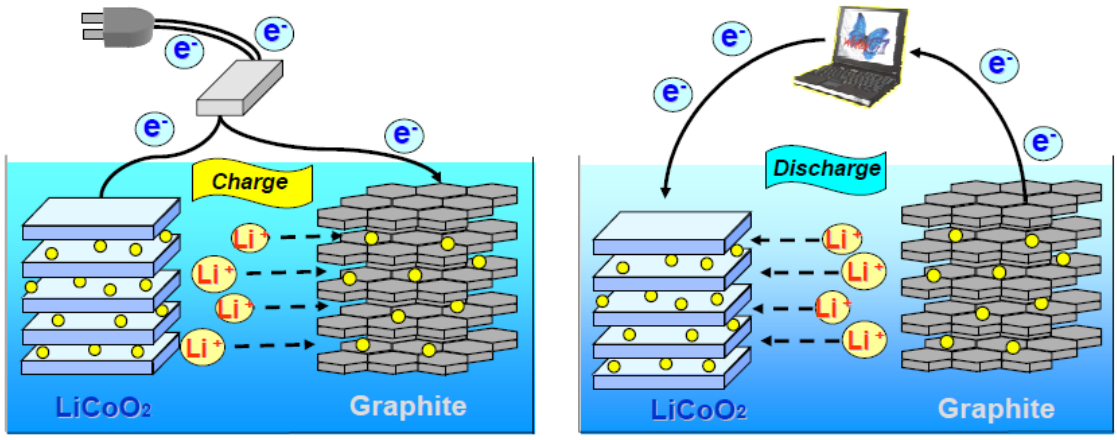

Figure 3. Illustration of the working principle of a lithium ion battery using $LiCoO_2$ as the cathode and graphite as the anode.

The electrochemical reaction occurring in the cathode material ($LiCoO_2$) is shown in reaction (1): lithium ions are transported from the positive to negative electrodes by oxidizing the transition metal, cobalt, in Li_xCoO_2 from Co^{3+} to Co^{4+} during charge. And the Co^{4+} is reduced to Co^{3+} during the discharge while the lithium ions move back from negative to positive electrodes. The complete reaction is shown in reaction (3)

Positive electrode half reaction $LiCoO_2 \leftrightarrow Li_{1-x}CoO_2 + xLi^+ + xe^-$ (1)

Negative electrode half reaction $C_y + xLi^+ + xe^- \leftrightarrow C_yLi_x$ (2)

Total reaction $LiCoO_2 + C_y \leftrightarrow Li_{1-x}CoO_2 + C_yLi_x$ (3)

1.2.2 Materials used in lithium ion batteries

Figure 4 is one type of commercially used prismatic lithium ion cells. Lithium ion battery packs can come in all shapes and sizes, but they all look about the same on the inside. For the outside material, as with most batteries, lithium ion batteries have an outer case made of metal. The use of metal is very important here because the battery is pressurized during assembly. In this case, it has a pressure-sensitive vent hole that will release the extra pressure (when the battery gets hot) to avoid exploding. This metal case holds a long spiral comprising three thin sheets (pink, green and orange in Figure 4) pressed together. These three thin sheets are composed of one positive electrode, one negative electrode and one separator in between. Inside the case these sheets are submerged in an organic solvent that acts as the electrolyte.

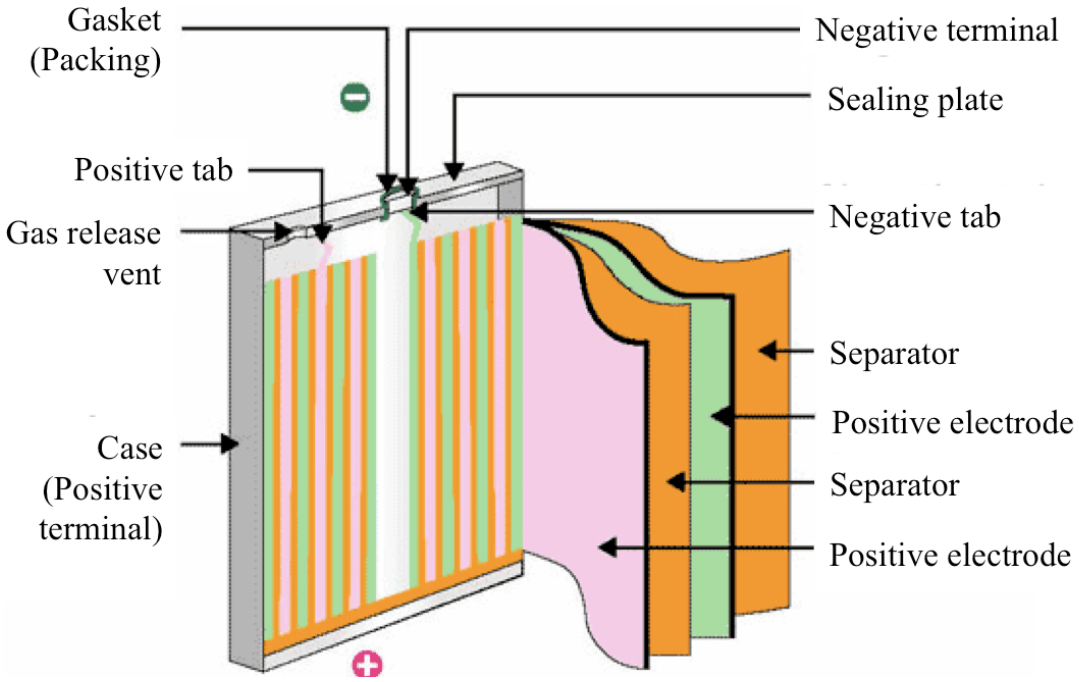

Figure 4. Structure of a prismatic lithium ion cell.

As discussed earlier, the four primary functional components of a lithium-ion battery are the positive electrode, negative electrode, separator and electrolyte. Normally, the positive electrode is a lithium metal oxide. It is generally one of the following three types of materials: a layered oxide (e.g. $LiCoO_2$), a spinel ($LiMn_2O_4$) or a polyanion (such as $LiFePO_4$) structure. The negative electrode of a conventional lithium-ion cell is made from carbon due to its abundance, low cost and good performance. The separator is a very thin sheet of microporous plastic, which is made of polyethylene (PE) or polypropylene (PP) or a mixture of both. The electrolyte is typically a mixture of organic carbonates such as ethylene carbonate or diethyl carbonate containing complexes of lithium ions. These non-aqueous electrolytes generally use non-coordinating anion salts such as lithium hexafluorophosphate ($LiPF_6$), lithium hexafluoroarsenate monohydrate

($LiAsF_6 \cdot H_2O$), lithium perchlorate ($LiClO_4$), lithium tetrafluoroborate ($LiBF_4$) and lithium triflate ($LiCF_3SO_3$).

1.3 Anode materials used in lithium ion batteries

The first commercialized lithium-ion battery by Sony in 1991 used carbon as the anode. It's been popular since that time due to its low cost and low operating voltage (0.2V vs. Li). The lithium interaction is well known, as shown in reaction (4).

$$Li+6C \leftrightarrow LiC_6 \quad (4)$$

The theoretical capacity is 372mAh/g for carbon. Despite the advantages of anodes made from carbon, it has been recognized for some years that new anode materials are needed. One of the reasons is the structure degradation because of the reaction between carbon and electrolyte during cycling, though this can be improved by adding electrolyte additives[5]. Most importantly, graphitic carbon is very limited by the capacity (Figure 5), especially volumetric capacity compared to the other candidates. Figure 5 shows the theoretical capacity of various anodes. It's clear to see that carbon has a very low capacity compared to the other candidates. A large amount of effort has been expended in the past two decades to improve the battery performance in terms of the energy density and rate capacity. There are three main aspects that researchers have been focusing on.

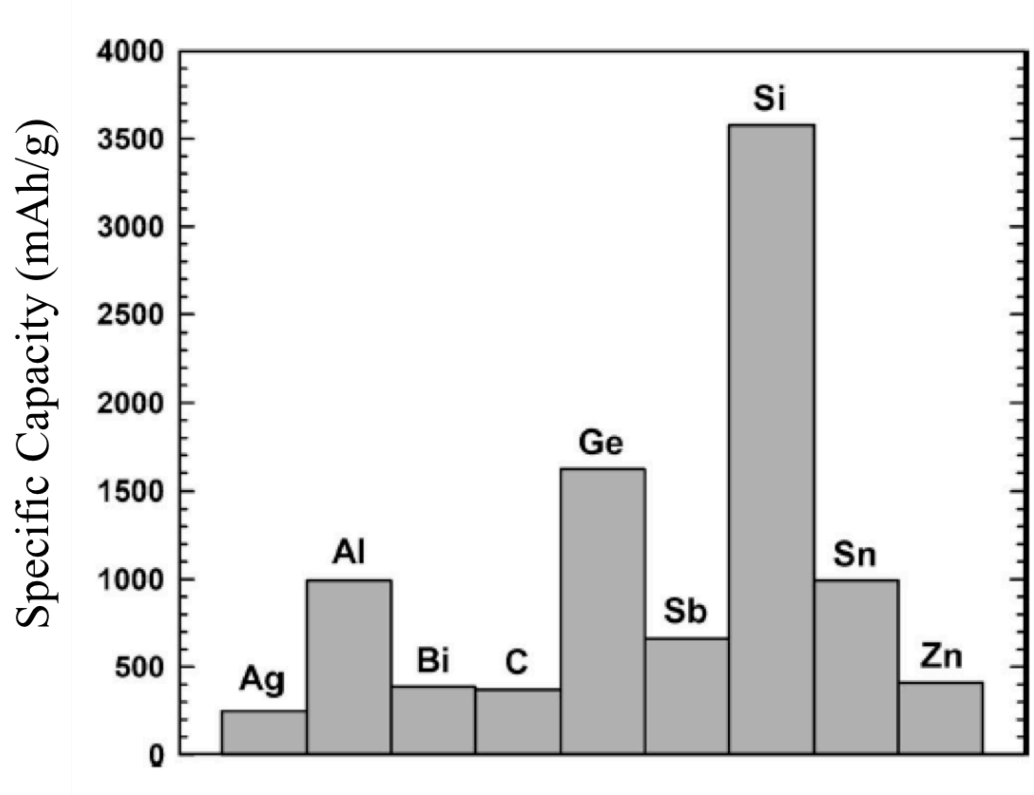

Figure 5. Specific capacity comparison among different anode materials for lithium ion battery[6]

First is the modification of the carbonaceous materials. Numerous carbon materials from natural and synthetic graphites, low-temperature and non-graphitized carbon as well as doped carbons have all been studied. Analysis of the published results showed that both highly crystalline and high disordered materials show the best electrochemical performance. Carbon with the intermediate crystallinity that was heat-treated in the temperature range 1600-2100^{o}C has lower reversible capacities. Low temperature carbons and hard carbons, doped or undoped, may display high reversible capacities.[7] However, graphites, especially those enriched in the rhombohedral phase, tend to demonstrate the best performance. They have low irreversible capacities and

reasonable capacities. Further improvement is still possible since carbon is the most versatile element from the periodic table, able to form varies chemical bonds with other elements, and has a variety of structures, textures and particles sizes.

Second is utilization of metallic lithium with stable electrolytes. The elements such as Si, Sn, Ge, Sb, Zn, Al, Bi can form alloys with lithium at relatively low voltages vs. Li. From Figure 5, we can see there are a variety of materials have high theoretical capacities compared with carbon. While we observe the dramatic capacity increase, there are also large volume changes (more than 100%) from Table 1. The volume change causes progressive cracking and eventually, pulverization of the metal particles, thereby inducing contact losses between them.[8] Therefore, although greatly appealing in terms of the storage capacity, lithium alloy electrodes are very hard to be used in practice. A lot of effort has been made to overcome or even control the pulverization effect. The main approach is to use metal oxides as the starting material instead of metal. This concept was first proposed by Fuji Photo Film Company in Japan and announced the use of amorphous SnOx as the anode.[9] The other solution is to use intermetallic compounds such as Sn_5Cu_6 [10]and $SnAg_2$.[11] The advantages are again to control the volume changes, thus improving the cycle life and capacities.

Table 1. Metallic lithium phase, capacity and volume change information.[12]

Starting materials	C	Bi	Al	Sn	Si
Lithiated phase	LiC_6	Li_3Bi	Li_9Al_4	$Li_{17}Sn_4$	$Li_{21}Si_5$
Theoretical specific capacity (mAh/g)	372	385	2235	959	4010
Theoretical volumetric capacity (mAh/ml)	833	3773	6035	7000	9340
Volume change (%)	12	115	238	257	297

The last method involved seeking new materials. Lithium titanate ($Li_4Ti_5O_{12}$) with a spinel structure turns out to be a promising anode candidate.[13-16] This material has a theoretical specific capacity of 175 mAh/g and exhibited a practical specific capacity as high as 160 mAh/g after 100 cycles. The mid-discharge potential for Li insertion is about 1.5 V vs. Li, which is above the potential range where most electrolytes or solvents are reduced. Thus, it can avoid the SEI formation and improve the safety of lithium ion cells. The lithium intercation/deintercation process in this compound is the following:

$$Li_4Ti_5O_{12}+3Li \leftrightarrow Li_7Ti_5O_{12} \quad (5)$$

Here, the reaction is only accompanied by a small lattice volume change, also called "zero strain" material. Unlike lithium alloy materials, lithium titanate is a very stable material with good cycle-ability and a very small capacity fade upon cycling.[16] However, $Li_4Ti_5O_{12}$ has a fairly low electronic conductivity (ca. 10^{-13} S cm^{-1}) and a moderate Li^+ diffusion coefficient (10^{-9}–10^{-13} cm^2 s^{-1}), thus the high rate performance is not satisfactory for some applications. Commonly used strategies to solve this problem are to reduce the particle size[17-19] and to coat conductive materials on the surface of

$Li_4Ti_5O_{12}$.[20-22] Reducing the particle size decreases the lithium ion diffusion path length, therefore the rate capability can be improved. Coating conductive materials on the surface enhances the electronic conductivity of electrode.

In conclusion, there are a variety of carbonaceous and non-carbonaceous compounds that have been intensively studied recently, but their performances are still to be fully ascertained before they can be commercialized into the battery market. Therefore the standard carbonaceous materials, i.e., graphite or coke, are likely to be the anode choice in the near future.[7] It's likely that the lower voltage request of the electronic circuits may open chances for the middle voltage, zero-strain insertion compounds like lithium titanate in the next few years.

1.4 Cathode materials used in lithium ion batteries

In current lithium ion battery technology, cell voltage and discharge capacity are mainly determined by the cathode material, which is also the limiting factor for lithium ion transportation rate. The developments of cathode materials therefore become extremely crucial and have received much attention in recent years. As we introduced in section 1.2.2, three types of conventional cathode materials were categorized by structure: layered compounds $LiMO_2$ (M = Co, Ni, Mn, etc.), spinel compounds LiM_2O_4 (M = Mn, etc.), and olivine compounds $LiMPO_4$ (M = Fe, Mn, Ni, Co, etc.). Most of the research were performed on these materials and their derivatives, and is also the areas that we are focusing on. Recently, new research has also started on the other types of intercalation

structure materials such as silicates, borates and tavorites.[23-28] We will discuss each of these.

Table 2 Summary of cathode and anode materials used for different types of lithium-ion batteries.[29]

Types	Cathodes	Anodes
High energy	$LiNi_xCo_yM_{1-x-y}O_2$ (layered) [a]	Si, Sn, Sb
	$LiMn_{2-x}MnO_4$ [b]	Mo_x [d]
	MF_x [c]	graphite
High power	$LiMn_{2-x}Al_xO_{4+\delta}$	Hard carbon
	$LiNi_xCo_{1-2x}Mn_xO_2$	graphite
	LiFePO4 (olivine)	$Li_4Ti_5O_{12}$
Long cycle life	LiFePO4 (olivine)	$Li_4Ti_5O_{12}$
	$LiMn_{2-x}Al_xO_{4+\delta}$	graphite

[a]M= Mn, Al, and Cr. [b] 5 V systems, M=Ni, Cu, and Cr. [c]M=Fe, Co, Ni, Cr, Mn, Cu, and Sn. [d]M=Fe, Co, Ni, Cr, Mn, Cu, and Sn.

1.4.1 Layered structures

Several oxides with the general formula $LiMO_2$ (M = Co, Ni, Mn, etc.) crystallize in a layered structure. The oxygen anions form a close-packed fcc lattice with cations located in the 6-coordinated octahedral crystal site. $LiCoO_2$ is used as an example to demonstrate the crystal structure (Figure 6a). As shown in Figure 6(b), the structure consists of CoO_2 slabs with layers of lithium in-between the slabs. Columns of lithium ions in this structure can be viewed clearly in the [110] projection, as shown in a two-dimensional cell of 2.44 Å by 14.05 Å (Figure 6c).

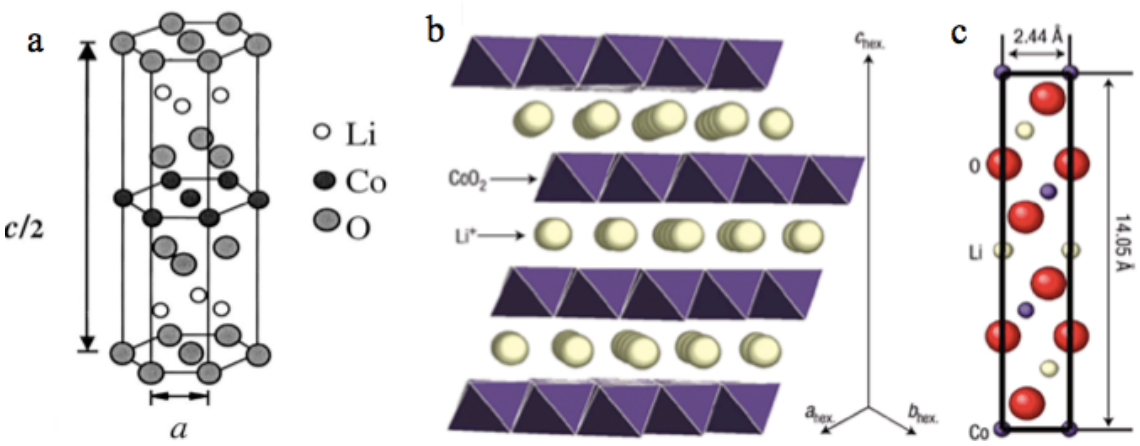

Figure 6. (a) Crystal structure of $LiCoO_2$ having the O3 layered structure;[12] (b) Drawn with lithium ions horizontally between CoO_2 octahedra, lattice parameters a= b= 2.8138 Å and c= 14.0516 Å. (c) Projection along the [110] zone axis shows lithium, cobalt and oxygen atoms in columns.[30]

$LiCoO_2$ is the most widely used positive electrode. A high lithium chemical potential associated with the highly oxide Co^{3+}/Co^{4+} couple could provides a high cell voltage of around 4V.[31] The direct Co-Co interaction with a partially filled t_{2g}^{6-x} band associated with the $Co^{3+/4+}$ couple leads to high electronic conductivity for $Li_{1-x}CoO_2$. Additionally, the strong preference of the low spin Co^{3+} ($t_{2g}^6 e_g^0$) and Co^{4+} ($t_{2g}^5 e_g^0$) ions for the octahedral sites provides good structural stability of $Li_{1-x}CoO_2$ without migrating of the $Co^{3+/4+}$ ions from the octahedral sites of the cobalt plane to the octahedral sites of the lithium plane via the neighboring tetrahedral sites.[12] These features make $LiCoO_2$ an excellent cathode for the lithium ion cells. The theoretical capacity of $LiCoO_2$ is approximately $274 mAhg^{-1}$. However the practical capacity is limited to almost half the theoretical value due to a hexagonal to monoclinic phase transformation upon charging between 4.15 and 4.2V.[32, 33] In order to prevent phase instability, the substitution of metal elements for Co in $LiCoO_2$ or a surface coating has been suggested. Various metal oxides

(e.g. MgO, ZrO_2, TiO_2, Al_2O_3, ZnO) have been coated on the surface of $LiCoO_2$ and reported to improve the cycle-ability of $LiCoO_2$,[34-36] but full delithiation is still not possible without cycling losses.

Another layered compound with the composition of $LiNiO_2$ has also been investigated for battery applications.[37-40] The low cost and non-toxicity make it a good candidate for the lithium ion battery applications. However, it has drawbacks that hindered its development. Its primary drawback is due to its structural instability during the synthesis. There is some lithium loss and the reduction of some Ni^{3+} to Ni^{2+} oxidation states while during synthesis.[41] The reduced Ni^{2+} could migrate to Li^+ sites because of their similar ion sizes, so the actual composition can be written as $Li_{1-z}Ni_zO_2$[40]. The degree of disorder could be changed by the synthetic conditions, thus to improve the electrochemical properties.[37, 42] The difficulty of making this material was one impediment to its wide use and commercialization ability in industry. Partial substitution of Ni by Cu, Al or Ti was reported to be effective towards reducing this disorder.[43] Despite of this progress, $LiNiO_2$ has not yet reached a large impact in battery manufacturing.

In 2001, Ohzuku and Makimura introduced an alternative layered cathode material $Li[Ni_{1/3}Co_{1/3}Mn_{1/3}]O_2$ (NCM)[44] by mixing three metal precursors by a solid state method. Since then, $Li[Ni_{1/3}Co_{1/3}Mn_{1/3}]O_2$ has drawn much attention as it exhibits much higher capacity of close to 200 mAh/g with enhanced safety,[45-47] thus it proves to be a promising cathode candidate in battery applications. Electronic structural studies have shown that it consists of Ni^{2+}, Co^{3+}, Mn^{4+} and the reversible capacity involves the

oxidation of Ni^{2+} to Ni^{4+} with a two-electron transfer during the initial stage and that of Co^{3+} to Co^{4+} in the later stage.[48, 49] Thus the higher capacity of the layered $Li[Ni_{1/3}Co_{1/3}Mn_{1/3}]O_2$ could be due to the improved chemical stability associated with the $Ni^{2+/3+}$ and the $Ni^{3+/4+}$ redox couples compared to the $Co^{3+/4+}$ redox couple. Despite the positive effect of $Li[Ni_{1/3}Co_{1/3}Mn_{1/3}]O_2$ on its electrochemical properties, the discharge capacities have shown a fading effect when a high rate current density was applied[50]. The addition of dopants,[51, 52] the optimization of $Li[Ni_{1/3}Co_{1/3}Mn_{1/3}]O_2$ morphology[53, 54] and coatings have been studied to improve its performance during cycling at high rates.[55-57]

1.4.2 Spinel structures

Mn-based compounds have been studied extensively, specifically the three dimensional $LiMn_2O_4$ spinel.[58-64] It was first proposed as the cathode material in lithium ion batteries by Thackeray et al. in 1983.[65] Thereafter, it became one of the most popular cathode candidates due to its abundance sources, low cost, high voltage and friendly impact on our environment (compared to Co and Ni).

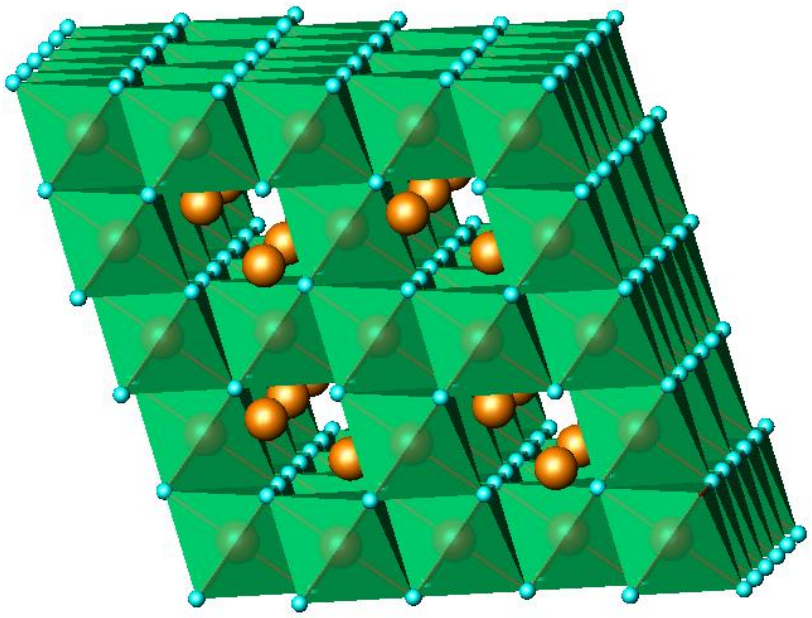

Figure 7. Crystal structure of spinel $LiMn_2O_4$ (blue: oxygen ions; brown: lithium ions; green: manganese ions).

The structure of $LiMn_2O_4$ spinel is shown in Figure 7. The oxygen framework of $LiMn_2O_4$ is the same as that of the $LiMO_2$ layered structure. Mn cations still occupy the octahedral sites, but 1/4 of them are located in the Li layer, leaving 1/4 of the sites in transition metal layer vacant. Li ions occupy the tetrahedral sites in the Li layer that share faces with the empty octahedral sites in the transition metal layer. The structure is based on a three-dimensional MnO_2 host, and the vacancies in the transition metal layer ensure the three dimensional Li diffusion pathways.[59] The advantage of three-dimensional frameworks over two-dimensional layered structures are: (i) the possibility of avoiding, for steric reasons, the co-insertion of bulky species such as solvent molecules and (ii) the smaller degree of expansion/contraction of the framework structure upon

lithiation/delithiation.[66] In spite of its advantages, this material was found to encounter sever capacity fading problems. The degradation mechanisms have been proposed as (i) structural damage due to Jahn-Teller distortion,[67] (ii) dissolution of the Mn^{2+} into the electrolyte: $2Mn^{3+} \rightarrow Mn^{4+} + Mn^{2+}$,[68] (iii) oxidation of the electrolyte on the surface of the cathode at the highly charged state.[69] Substituting Mn with other metal ions has been used as an important approach to improve cycling performance of spinel materials. Multiple dopants including inactive ions such as Mg and Al,[70, 71] transition metal ions such as V, Cr, Co and Ni,[72-75] and rare earth metal ions such as Nd and Sm[76, 77] have been investigated. $LiNi_{0.5}Mn_{1.5}O_4$ shows the best overall electrochemical performance among the above.[78-81]

1.4.3 Olivine structures

Polyanion materials are receiving growing attention because of the inherent stability of the polyanion group, which can delay or minimize the oxygen loss occuring in traditional layered or spinel oxides. Among all of the polyanion-based materials, $LiFePO_4$ has attracted the most interest due to its excellent electrochemical properties. The crystal structure of $LiFePO_4$ is shown in Figure 8. It contains slightly distorted hcp anion oxygen arrays with half of the octahedral sites occupied by Fe and one eighth by Li. The FeO_6 octahedra are corner-shared while LiO_6 octahedra are edge-shared. Covalent P-O bonds stabilize the oxide when fully charged and avoid O_2 release, making $LiFePO_4$ the most stable commercial cathode material.[82] Due to its chemical stability, it has stability during cycling and tolerance to overcharge (i.e., it's safer compared to $LiCoO_2$). Most importantly, it is composed of abundant resources, which are environmentally friendly.

Olivine $LiFePO_4$ has been considered as the most promising cathode candidate for the next-generation large-scale lithium ion batteries used for hybrid electric vehicles (HEVs) or electric vehicles (EVs)

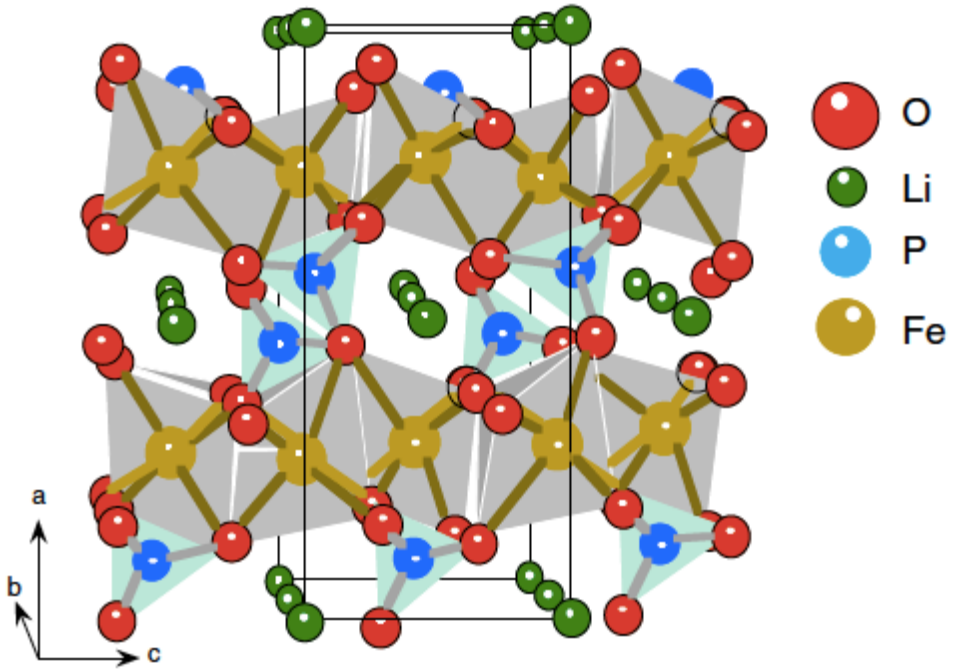

Figure 8. Crystal structure of spinel $LiFePO_4$. It contains FeO_6, LiO_6 octahedra and PO_4 tetrahedra.

Although $LiFePO_4$ shows excellent cycling performance, the main drawbacks of this material are its low energy density due to its low voltage (OCV is 3.4 vs. 3.7 for $LiCoO_2$ and 4.2 for $LiMn_2O_4$), low lithium ion diffusion rate (10^{-14} cm^2 s^{-1})[83] and extremely poor intrinsic electronic conductivity (10^{-10} S cm^{-1}).[84] Different experimental approaches have been proposed to solve these issues, including: (i) partial substitution of Fe with Mn, Co or Ni due to the different redox potentials; (ii) coating the particles with a conductive film to increase the electronic conductivity; (iii) decreasing the particle size and shorten the lithium ion diffusion path to improve the lithium ion diffusion rate.

Olivine structures can also be formed from other metals such as Mn, Co and Ni. Based on different active redox couples, the open circuit voltage is 4.1 V for $LiMnPO_4$,[85] 4.8 V for $LiCoPO_4$[86] and 5.1 V for $LiNiPO_4$.[87] Figure 9 illustrates the phosphate voltage vs. gravimetric capacity for various redox couples, where the red dashed line indicates the upper voltage considered as safe area against electrolyte decomposition. Due to the limited voltage window of the current electrolyte, intensive research work have been done on $LiMnPO_4$ and doping $LiFePO_4$ with Mn, Co or Ni on the Fe site (so-called divalent doping) to get an optimal voltage as well as an increased performance.[88-92]

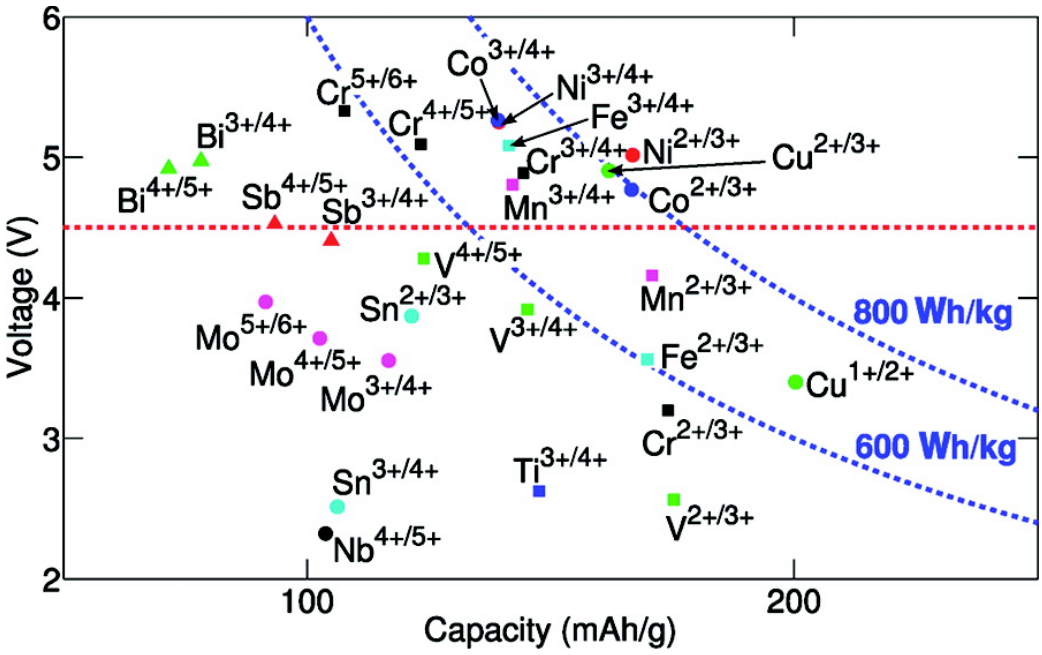

Figure 9. Voltage in various phosphates versus gravimetric capacity. The blue dashed lines are the energy density curves at 600 and 800 Wh/kg. The red dashed line indicates the upper voltage considered as safe area against electrolyte decomposition.[93]

For the low electronic conductivity of this material, coating the surface with a conductive film is believed to be an effective method to increase the electronic conductivity of the material, thus increasing the rate capability. Conductive carbon is one

of the popular coating materials and has been widely investigated. It was firstly reported by Armand et al. in 2001 that more than 90% of capacity could be reached after adding carbon on $LiFePO_4$ with good stability.[94] Later, Dahn et al. showed the $LiFePO_4$/C composite demonstrated a discharge capacity of 125mAh/g at even at 5C current density.[95] Besides the carbon coating, other conductive materials such as metals and metal oxides were used to improve the electronic conductivity of $LiFePO_4$.[96, 97]

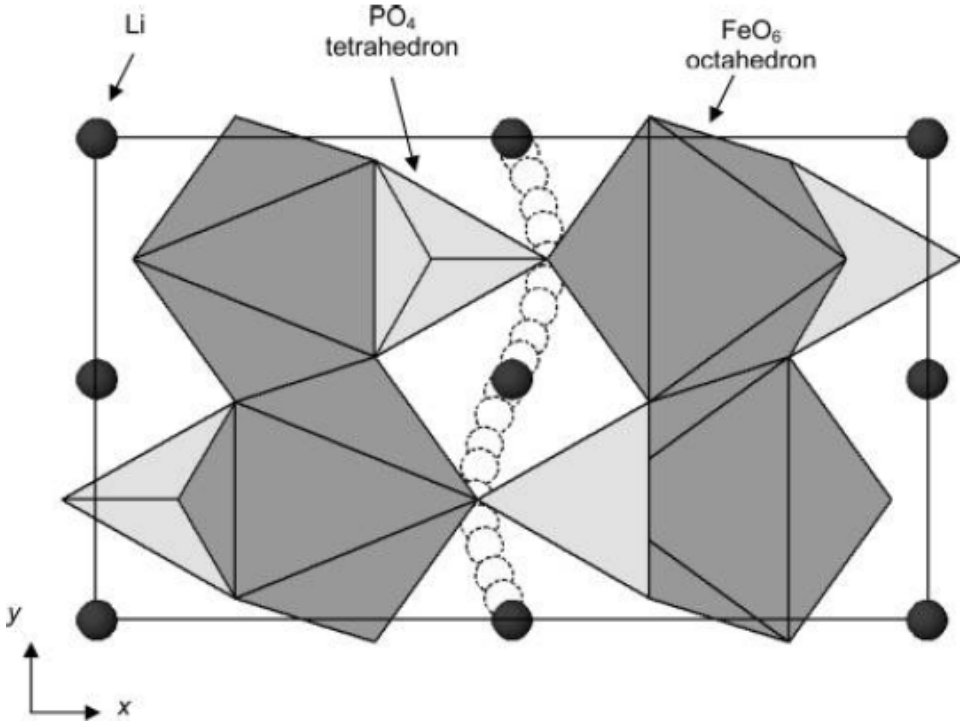

Figure 10. Curved trajectories for Li ion migration between sites in the [010] direction The diffusion path lies out of the x-y plane.[98]

The approach to increase the lithium ion diffusion rate is to minimize the particle size to shorten the Li ion diffusion length in the solid state as well as decrease anti-site defects to increase the Li-ion conductivity. Because of the [010] one dimensional Li diffusion pathway in $LiFePO_4$,[98, 99] a single immobile defect would block the diffusion path along the b axis (Figure 10). In the ideal ordered olivine structure in Figure 11, all

lithium ions reside on the M1 site, while all iron ions are on the M2 site. The presence of M2 site ions or dopant ions on the M1 site has been theorized to hinder ion transport along the b-axis, and require 3D diffusion of Li^+. Calculations show that Li–Fe mixing leads to ‘‘anti-site (Li^+: Fe^{2+}) pairs’’, which are the most favorable defects that can occur in olivine, and have the lowest formation energy.[100] According to Yang et al., the nano-sized $LiFePO_4$ shows increased capacity compared to the micro-sized materials.[101] Later work by Ceder et al. reported that reducing particle size can help diminish the blocked capacity and nano-sized LFP is more tolerant to anti-site defects.[102]

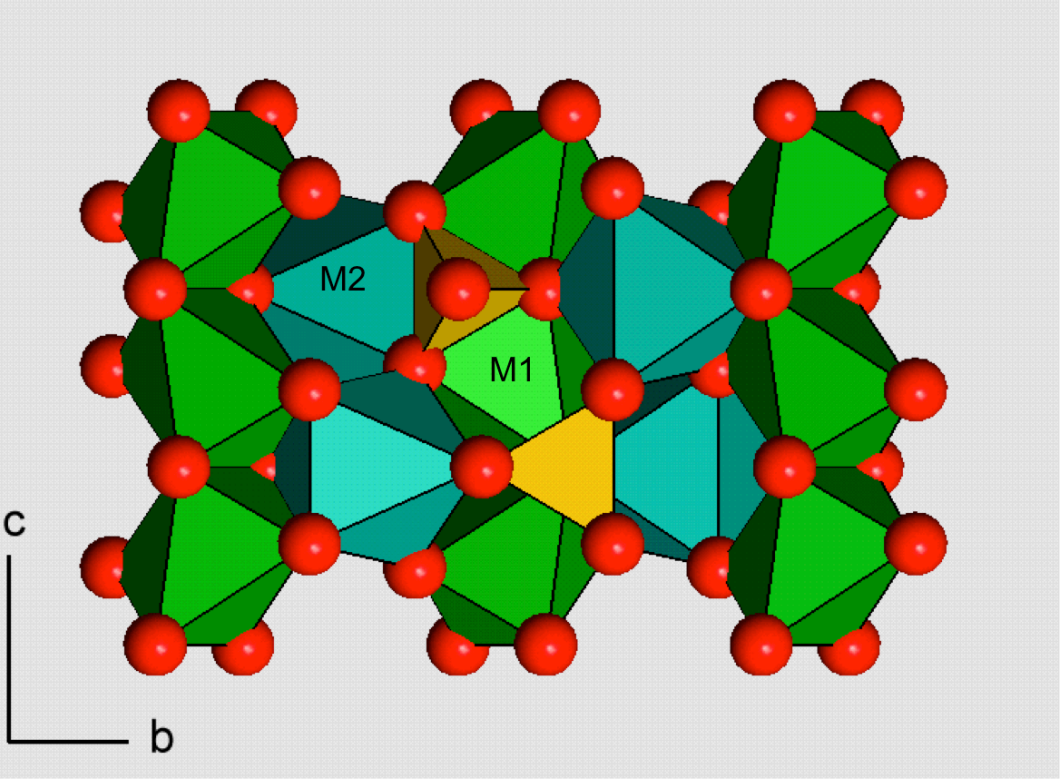

Figure 11. Ideal olivine structure shows M1 and M2 sites. M1 is the smaller site and M2 is the bigger site.

In summary, olivine $LiFePO_4$ has a lower voltage and similar gravimetric energy density compared to $LiCoO_2$. However, its low cost, long cycle life, chemical and

thermal stability, and environmental friendliness provide this material with high potential to be the next generation of commercialized cathode material used for HEVs or EVs. By partially substituting Fe with other transition metal ions such as Mn, Co or Ni in $LiFePO_4$, the open voltage can be significantly increased. However, the intrinsic low conductivity of this series of materials is still the key problem, which is also a focus of our research.

1.4.4 Other types

One of the recently investigated compounds is the olivine derivative structure-tavorite ($LiMPO_4F$).[103] The crystal structure of tavorite is shown in Figure 12, where the lithium ions are surrounded by FeO_6 octahedra and PO_4 tetrahedra. Tavorite has excellent both thermal and chemical stability due to the strength of the phosphorous and oxygen bonds, which makes it a good cathode candidate for many applications. Besides stability, the addition of fluorine into the structure opens up the 1D lithium diffusion path to a multidimensional pathway for lithium ions, therefore increasing ionic conductivity.[82]

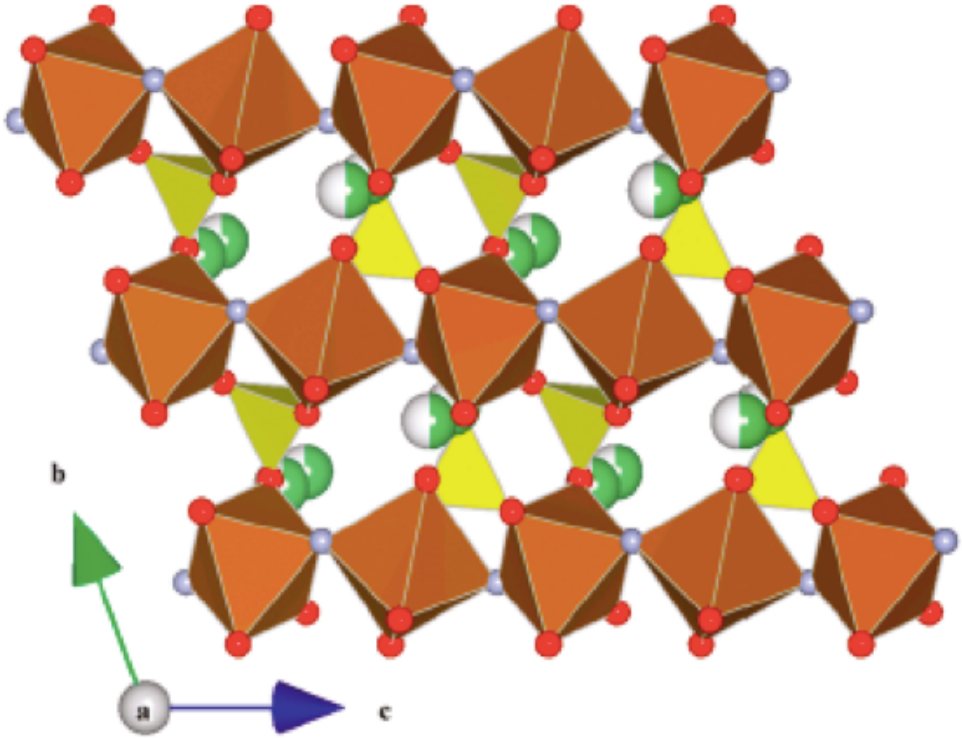

Figure 12. Crystal structure of a typical tavorite-structured material, $LiFe(PO_4)F$. Brown FeO_6 octahedra, yellow PO_4 tetrahedra, red spheres: O, and blue spheres: F. The green-and-white spheres represent partially occupied lithium sites, with the occupancy given by the fraction of the sphere shaded green.[28]

At the same time, growing interest in the silicate, Li_2MSiO_4 (M=Mn, Fe, Co, and Ni) has also been reported.[104, 105] Because of the possibility of having two lithium ions to be reversibly extracted from the host structure, the Li_2MSiO_4 cathode could offer a high theoretical capacity of ~330 mAh/g. However, its rate capability and cycling performance are still far from satisfying requirements for commercialization due to the instable structure upon use, though some positive results for Li_2MSiO_4 (M= Mn, Fe, Co, and Ni) have been recently reported.[106]

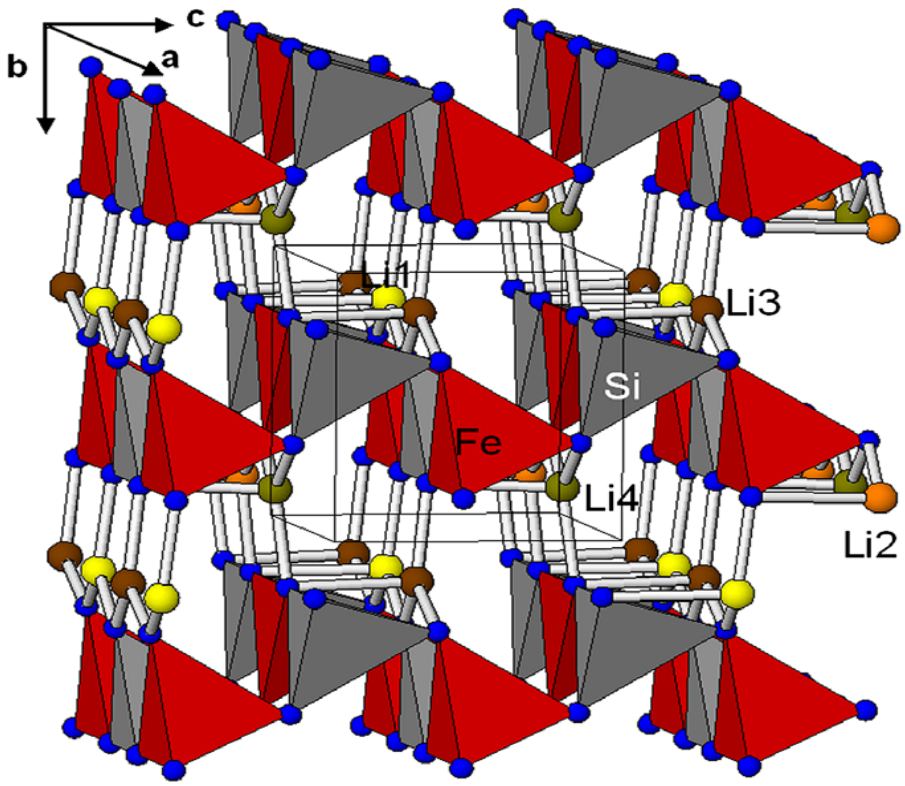

Figure 13. Crystal structure of the silicate Li_2FeSiO_4, Li ions at sites 1, 2, 3 and 4 are labeled and colored differently.[107]

1.5 Objectives

As we discussed previously, cathodes in lithium ion batteries are a very important aspect which affects the whole cells parameters such as cell voltage, discharge capacity, cycle life, etc. Therefore, their study is extremely crucial and thus have received much attention in recent years. From Table 2, we can see both the layered NCM structure and olivine structure materials are promising cathodes, as they can provide high power and high energy, and are thus the focus of our research.

1.5.1 Specific objectives for NCM

$Li[Ni_{1/3}Co_{1/3}Mn_{1/3}]O_2$ (NCM) has drawn much attention as it exhibits much higher capacity of close to 200 mAh/g with enhanced safety compared to traditionally used $LiCoO_2$. However, there are still some factors that limit the performance of this material such as relatively large particle sizes, inhomogeneous particle size distributions, and low packing densities. The electrochemical performance of these materials has been reported to be dependent upon structure, composition and voltage range during charge/discharge. Therefore, the microstructure of the cathode material is a key factor in its performance, as it controls the packing density, diffusion rates and pathways. The particle size and distributions are strongly dependent on the synthesis methods and annealing processes. Consequently, a thorough understanding of the nucleation and growth of these materials is of fundamental importance. At the same time, we performed a thorough investigation of the structure-performance relationship in order to uncover the details of factors that cause capacity fade.

Objective 1: Investigate the crystal growth behavior of the NCM cathode, synthesized by using a two-step synthesis method, during the annealing process.

We have successfully utilized a two-step synthesis method involving co-precipitation and annealing to investigate the crystal growth behavior of NCM displaying the α-$NaFeO_2$ structure. Annealing at different temperatures and subsequent materials characterization were used to determine specific crystal growth modes in these materials in order to determine synthesis-structure relationships.

The information revealed by this study will help develop guidelines to control the size and morphological features more precisely, and will help create design strategies for cathodes that will enable efficient lithium ion transport and extended lifetime batteries.

Objective 2: Study NCM capacity degradation mechanisms. Discuss the annealing temperature, crystal structure and crystal size effects on its capacity fade.

Here, we have systematically investigated the effects of crystal structure and size effects on the performance degradation of NCM cathodes. The data from this study will help shed light on structure-performance parameters for NCM, and also uncover relationships between nanoscale cathode structures and their use in batteries.

1.5.2 Specific objectives for $LiFePO_4$

With the increasing electric vehicle demand market in our modern life, the olivine $LiFePO_4$ (LFP) has been considered one of the most promising cathode candidates for the next-generation large-scale lithium ion battery used for hybrid electric vehicles (HEVs) or electric vehicles (EVs) due to its low cost, low toxicity, thermal and chemical stability, and its good cycle stability. However, it is hindered by a low rate capacity due to the poor electronic conductivity and low lithium ion diffusivity, which inhibits expanding its commercial potential. Various solutions have been applied to overcome this inherent deficiency of LFP including size tailoring, addition of conductive agents (carbon, silver, etc.) and cationic or anionic doping. It is important to use non-toxic and low cost synthesis systems. Thus, understanding the formation mechanism (i.e., synthesis-structure) and the resulting crystallinity on the performance (i.e., structure-performance) is helpful for improved performance. In addition, utilizing conformal coatings on LFP

with minimum volumetric capacity decrease and increased rate performance for the big applications in HEVs and EVs is also important.

Objective 1: Uncover the formation mechanisms of LFP nanostructures, using an environmental-friendly synthesis method, and determine structure-performance relationships.

Here, we investigate the crystal nucleation and morphological evolution of $LiFePO_4$ in a water-triethylene glycol system under moderate pressures and low temperatures. Detailed materials characterization techniques were used to interrogate size, morphological and orientational changes to reveal growth mechanisms which will yield synthesis-structure relationships.

Objective 2: Study the effective conformal coating of LFP via polymer solution coating methods based on compatibility of LFP and polymer functionality.

Here, we have successfully applied thin layer carbon coatings via a polymer solution method. The goal here was to make conductive LFP with carbon that did not inhibit Li-ion transport.

Chapter 2.

Crystal Growth of $Li[Ni_{1/3}Co_{1/3}Mn_{1/3}]O_2$ as a Cathode Material for High-Performance Lithium Ion Batteries

Jianxin Zhu, Thinh Vo, Dongsheng Li, Richard Lu, Nichola M. Kinsinger, Laj Xiong, Yushan Yan, and David Kisailus. Crystal Growth of $Li[Ni_{1/3}Co_{1/3}Mn_{1/3}]O_2$ as a Cathode Material for High-Performance Lithium Ion Batteries, Crystal Growth & Design, 2012, 12 (3), pp 1118–1123.

ABSTRACT:

$Li[Ni_{1/3}Co_{1/3}Mn_{1/3}]O_2$ (L333) has been successfully synthesized through a two-step co-precipitation and annealing method. Crystal phase and growth behavior were monitored by X-ray diffraction (XRD) while particle morphologies were observed by scanning electron microscope (SEM) and transmission electron microscopy (TEM). We observed three primary growth regions in the temperature range of 600-1000^{o}C. In the low temperature region (i.e., 600 – 750°C), there is almost no grain growth as well as a small rate-controlling mechanism exponent 1/n data (1/n = 0.2), which is likely due to surface diffusion. In the medium temperature range (800 – 900^{o}C), growth is controlled by the volume diffusion of ions within the matrix, while in the high temperature region from 900^{o}C to 1000^{o}C, crystal growth is controlled by the diffusion of ions along the matrix-particle boundary.

2.1. Introduction

$LiCoO_2$ has been used as a cathode material for commercially available lithium-ion batteries due to its facile preparation and excellent cycling stability.[108] However, the toxicity, high cost of cobalt, and charging limitations prohibits its long term viability. In 2001, Ohzuku and Makimura[44] introduced an alternative cathode material, $Li[Ni_{1/3}Co_{1/3}Mn_{1/3}]O_2$ (L333), as it combines the advantages of high specific capacity, low cost, long cyclic life, and both structural and thermal stability.[109-112] Thus, it proves to be a promising candidate cathode in battery applications. Some of the factors that limit the performance of this material are related to relatively large particle sizes, inhomogeneous particle size distributions, and low packing densities. The

electrochemical performance of these materials has been reported to be dependent upon structure, composition and voltage range during charge/discharge. Zhang et al.[113] reported that smaller particle size and good homogeneity of materials may mainly account for the improved electrochemical properties of the L333. Therefore, the microstructure of the cathode material is a key factor in its performance, as it controls the packing density, diffusion rates and pathways. As we know, the particle size and distributions are strongly dependent on the synthesis methods and annealing processes. Although lower temperature synthetic routes may yield smaller particles, which shorten diffusion path lengths, there is also a reduction in the tap density at the same time. Lee et al.[5] synthesized larger L333 particles (i.e., 10μm) using co-precipitation and annealing to yield nearly uniform particles that had a tap density of 2.39g/cm^3. Additional synthesis processes[114-117] and structural characterization methods[45, 118, 119] of L333 materials have been utilized. Cho et al.[8] reported the carbonate co-precipitation method, which could synthesize the homogeneous material even at temperatures as low as 750°C. Guo et al.[9, 10] used a solid-state pyrolysis reaction method for effectively doping other elements or coating carbon to increase the conductivity. Although these mixed metal oxides have been synthesized by a number of routes, there is limited information about details of the growth of the particles during synthesis. Consequently, a thorough understanding of the nucleation and growth of these materials is of fundamental importance, not only for its intrinsic scientific interest, but also for its technological significance.[120, 121]

Here, we have successfully utilized a two-step synthesis method involving co-precipitation and annealing to investigate the crystal growth behavior of

$Li[Ni_{1/3}Co_{1/3}Mn_{1/3}]O_2$ displaying the α-$NaFeO_2$ structure. The information revealed by this study will help develop guidelines to control the size and morphological features more precisely, and will help create design strategies for cathodes that will enable efficient lithium ion transport and extended lifetime batteries.

2.2. Experimental Section

L333 powders were prepared using a two-step method. The precursor, $(Ni_{1/3}Co_{1/3}Mn_{1/3})(OH)_2$, was synthesized at room temperature through a co-precipitation method similar to those previously reported.[111] Figure 14 is the schematic illustration of the synthesis process. Briefly, stoichiometric amounts of nickel, cobalt and manganese nitrates (99.5% purity, Sigma-Aldrich Co.) were thoroughly dissolved in deionized water to achieve a homogeneously mixed 100mM solution. 2M NaOH was added (under stirring) to this solution to modify the pH to be 10, thus, inducing precipitation. The resultant suspension was subsequently stirred at 600 rpm under a nitrogen atmosphere at room temperature for 2 hours. The $(Ni_{1/3}Co_{1/3}Mn_{1/3})(OH)_2$ precipitates were washed three time with DI water and dried under vacuum at 70°C overnight. The $(Ni_{1/3}Co_{1/3}Mn_{1/3})(OH)_2$ precursor was then mixed with a 5% excess (to compensate the lithium evaporation) of $LiOH{\cdot}H_2O$ and subsequently ground with a mortar and pestle. The mixture was placed in an alumina boat and annealed in a preheated tube furnace at different temperatures (i.e., 600°C – 1000°C) for specific durations (3 – 24 hours) in air, which also helped in the oxidation of Co and Mn.

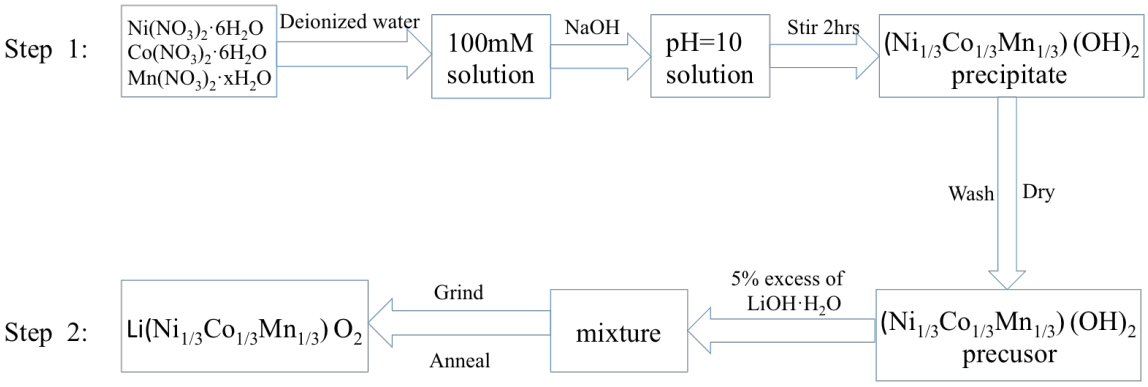

Figure 14. Schematic of $LiNi_{1/3}Co_{1/3}Mn_{1/3}O_2$ two steps (co-precipitation and annealing method) synthesis.

Phase identification was determined by X-ray diffraction analysis (XRD, Philips X'Pert) using Cu Kα radiation. Using the resulting XRD diffraction patterns, crystallite diameters were calculated based on the Scherer formula.[122]

$$D = \frac{K\lambda}{\beta \cos\theta}$$

Where D is the mean size of the ordered (crystalline) domains, which may be smaller or equal to the grain size; K is a dimensionless shape factor, with a value close to unity. The shape factor has a typical value of about 0.9, but varies with the actual shape of the crystallite; λ is the X-ray wavelength; β is the line broadening (full width) at half the maximum intensity (FWHM), after subtracting the instrumental line broadening, in radians and θ is the Bragg angle.

Particle sizes and morphologies were observed using a scanning electron microscope (SEM, FEI XL30) at 10 kV accelerating voltage. The SEM was equipped with an energy dispersive X-ray spectrometer (EDS) that was used to confirm sample stoichiometry (based on examination of five different regions per sample). A

transmission electron microscope (TEM, FEI T20), operated at 200 kV, was used to identify crystallite size, morphology and phase. Thermal and mass analyses were performed using a thermal gravimetric analyzer/differential scanning calorimetry (TGA/DSC Mettler Toledo) from room temperature to 1000^{o}C in air at a heating rate of 10^{o}C/min to investigate material reactions during annealing.

2.3. Results and Discussion

2.3.1 XRD

Figure 15 depicts an XRD pattern of the $(Ni_{1/3}Co_{1/3}Mn_{1/3})(OH)_2$ precursor after co-precipitation under N_2 at room temperature. Indexing of this diffraction pattern confirms the formation of the metal hydroxide structure.[123] All peaks were indexed on the basis of the hexagonal $Mn(OH)_2$ structure (JCPDS 12-0696).

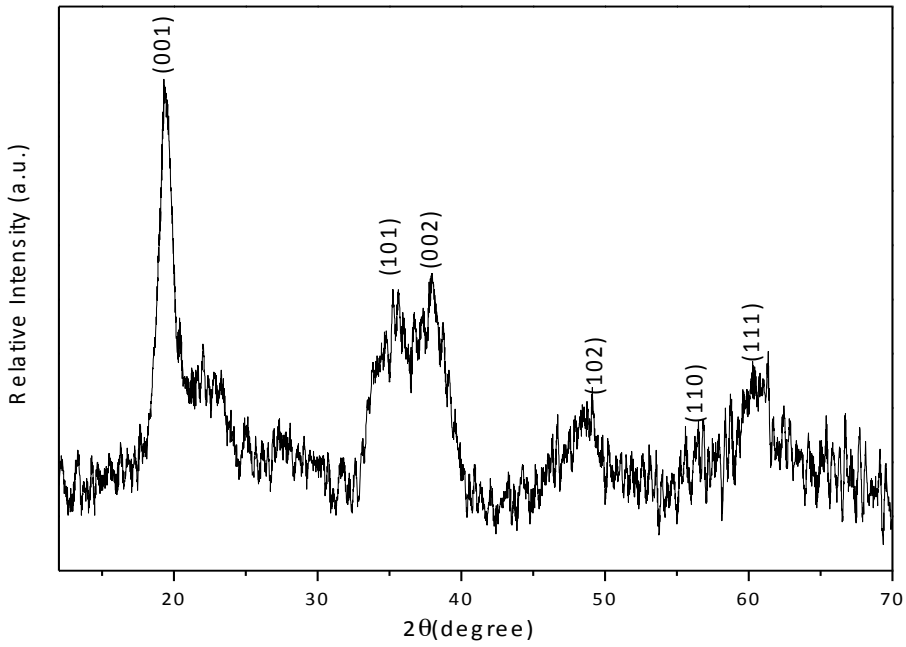

Figure 15. XRD pattern of $[Ni_{1/3}Co_{1/3}Mn_{1/3}](OH)_2$ precursor.

The metal hydroxide precursor was mixed with $LiOH \cdot H_2O$ and annealed at different temperatures. Figure 16 shows diffraction patterns of $Li[Ni_{1/3}Co_{1/3}Mn_{1/3}]O_2$ annealed in air at increasing temperatures for 12 hours duration time. Indexing of these diffraction patterns confirmed the formation of the layered L333 structure. All peaks from L333 were indexed on the basis of the hexagonal α-NaFeO2 structure with the $R\bar{3}m$ space group (JCPDS 82-1495).

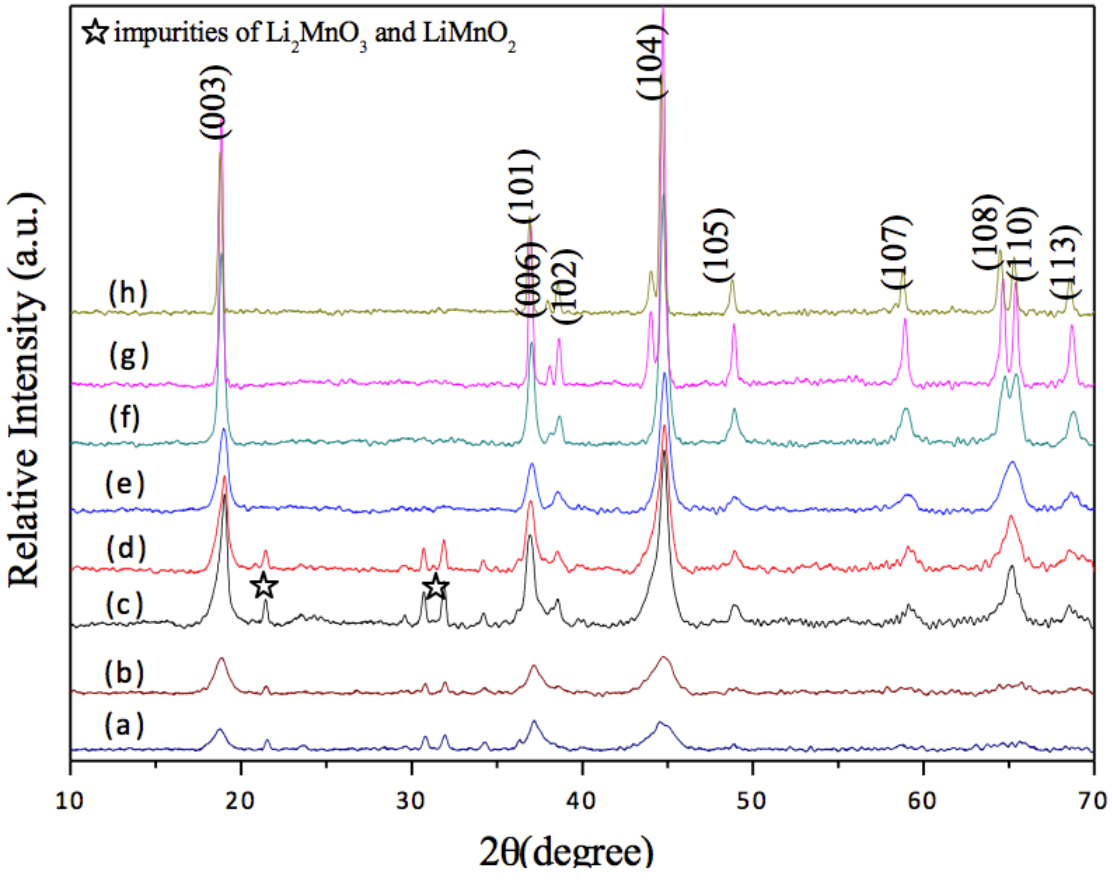

Figure 16. XRD patterns of $Li[Ni_{1/3}Co_{1/3}Mn_{1/3}]O_2$ heated for 12 hours at (a) 200°C, (b) 300°C, (c) 400°C, (d) 500°C, (e) 600°C, (f) 700°C, (g) 800°C, and (h) 900°C.

XRD analysis of samples annealed as low as 200°C for 12 hours has already indicated the presence of crystalline $Li[Ni_{1/3}Co_{1/3}Mn_{1/3}]O_2$. However, small quantities of

both Li_2MnO_3 and $LiMnO_2$ were also detected. After annealing at 600°C, the impurity phases were no longer detected. Above 700°C, significant crystal growth occurs, as indicated by the reduced full width at half maximum (FWHM) of the XRD peaks. The reported known indication of an ordered hexagonal layered structure,[108, 123, 124] which is confirmed by the presence of doublet peaks for the (006)/(102) at 37°(2θ) and the (108)/(110) reflections at 65°(2θ), is present for the samples heated at or above 700°C. This is an indicator of the ordering of the L333 layered structure, that enables the reduction of cationic mixing during intercalation and deintercalation of lithium ions inside the host matrix, leading to an increase in the electrochemical performance of this cathode material.[124]

Lattice parameters were calculated from the refinement of the XRD data, which are shown in Table 3. The ratios of c/a for all the samples are larger than 4.899, which confirm the layered structure based on work by Ngala et al..[125, 126] They reported that the c/a ratio of the lattice parameter is a direct measurement of the deviation of the lattice from a perfect cubic close packed lattice. Since the ideal cubic close packed lattice has a c/a value of 4.899, a larger c/a ratio means a more ordered layered structure. For all of our samples (table 3) except the 600°C annealed one, the ratios are larger than 4.960 and thus, they have the well ordered layered structure. In addition, according to the Wang et al.[127], the *R* factor ($R=I_{102}+I_{006}/I_{101}$) is related to the hexagonal ordering (i.e., the lower *R* value, the better hexagonal ordering). All of our samples have an *R* value less than 0.45, which is indicative of a good hexagonal ordering of the lattice.

Table 3. Calculated structure parameters for synthesized $Li[Ni_{1/3}Co_{1/3}Mn_{1/3}]O_2$.

Parameters	600°C	700°C	800°C	900°C	1000°C
a(Å)	14.001	14.133	14.158	14.176	14.261
c(Å)	2.858	2.852	2.851	2.853	2.870
c/a	4.899	4.966	4.969	4.969	4.970

2.3.2 TGA-DSC

The thermochemical properties (Figure 17) of synthesized L333 materials were investigated by thermogravimetric analysis and differential scanning calorimetry (TGA/DSC). As the specimen is heated, there is an endothermic peak at 90°C accompanied by a ~13% weight loss, which can be attributed to water desorption (consistent with the observed mass loss). The exothermic peak observed at 259°C is due to the decomposition of hydroxyl [128] and correspondingly the crystallization process is initiated with concurrent dehydration reactions. This has already been shown on the XRD of sample heated at 200°C for 12 hours. At the same time, there is another endothermic peak at 445°C, which is related with LiOH melting[129]. Furthermore, the third endothermic peak at 750°C is probably due to the completion of the ordering of the hexagonal lattice. There are some similar data reported by Delmas et al., who suggested that synthesis of $LiNiO_2$ systems at temperatures higher than 700°C produced 2D-type cationic ordering structure[130] and also by Jouybari et al., who reported the temperature at 700°C during their $LiNi_{0.8}Co_{0.2}O_2$ synthesis.[131] This is concurrent with observations from XRD analyses, which depicts an ordered layered structure at, and above 700°C. No

additional reactions are observed at higher temperatures, however, there is a small weight loss (~2.5%) from 800°C-1000°C likely attributed to evaporation of Li_2O.[128]

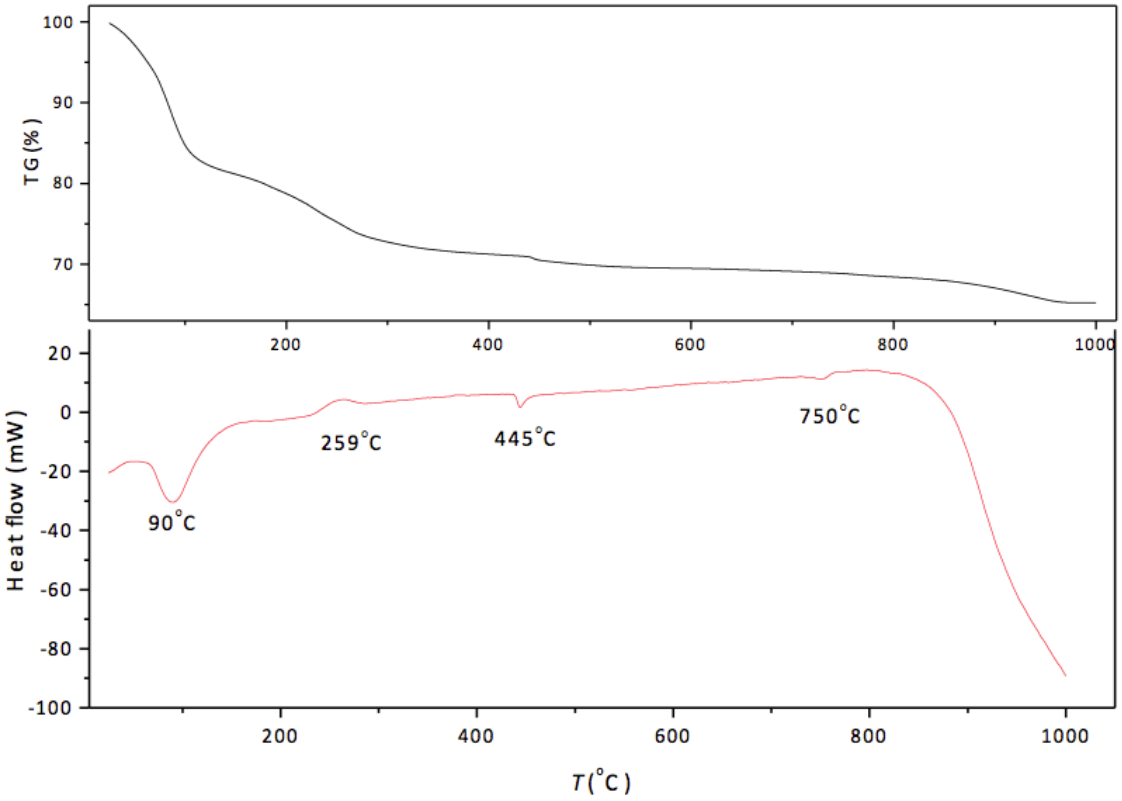

Figure 17. TGA-DSC of the mixture of $[Ni_{1/3}Co_{1/3}Mn_{1/3}](OH)_2$ and $LiOH \cdot H_2O$.

2.3.3 Microstructural Analysis

Figure 18 depicts SEM micrographs of $Li[Ni_{1/3}Co_{1/3}Mn_{1/3}]O_2$ specimens annealed in air at different temperatures for 3 hours. As mentioned previously, we observe significant crystal growth between 800°C and 1000°C. Specimens heated to 600°C demonstrate a nanocrystalline nature (i.e., crystal diameters less than 20 nm, as determined by transmission electron microscopy and x-ray diffraction). These crystals grow in size with increased temperature up to 250 nm by 900°C and eventually to 850 nm by 1000°C. The EDS spectra of the annealed powder (800°C / 3 hours, placed on a

Silicon wafer) in Figure 18 shows the presence of Ni, Co, Mn in a 1:1:1 ratio, with O, C and Si (wafer) present. No additional impurities were detected. The combination of XRD and EDS results confirmed that the final product was $Li[Ni_{1/3}Co_{1/3}Mn_{1/3}]O_2$.

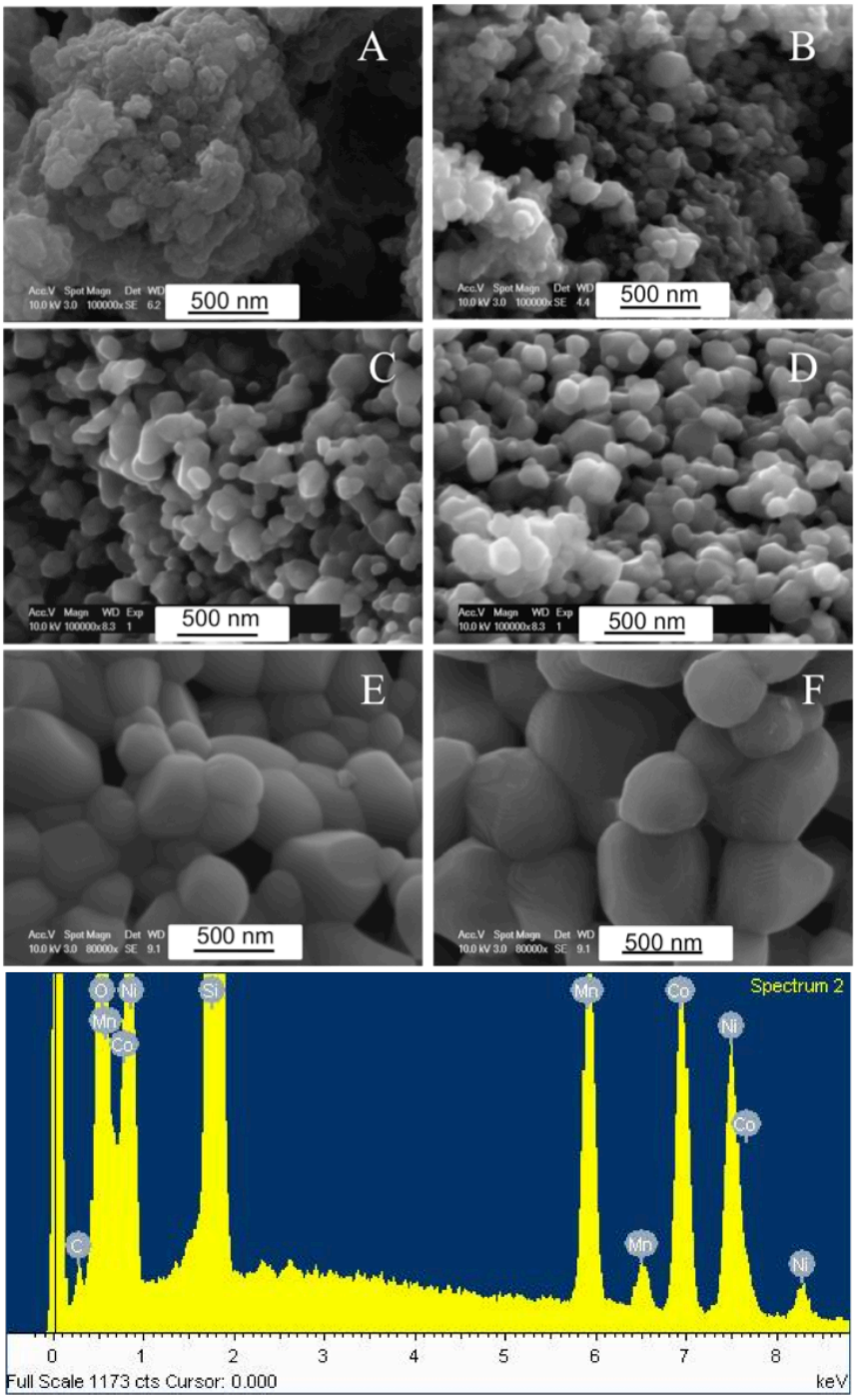

Figure 18. SEM micrographs of $Li(Ni_{1/3}Co_{1/3}Mn_{1/3})O_2$ annealed at (A) 600°C, (B) 700°C, (C) 800°C, (D) 900°C, (E) 950°C, (F) 1000°C for 3 hours with an EDS spectrum (bottom) from Sample (C).

Figure 19 shows the increase in particle diameter (as measured by both SEM and TEM) as a function of temperature for samples annealed for 3 hours. It is clear that there are three growth regions between 600°C – 1000°C. Region I, from 600°C – 750°C, exhibits minimal crystal growth, while the growth rate in region II (750°C – 900°C) is larger. Finally, above 900°C (region III) significant grain growth is observed. These three regions were divided based on the different slopes of the curve, increasing from 0.05±0.01 in region I to 1.54±0.02 in region II, and finally up to 6.09±1.11 in region III. This increased grain growth behavior in region II and III is partially attributed to the chemical potential gradient of the lithium ion between the surface and the interior of the particles because of lithium oxide evaporation as we observed in our thermal analyses. This may also act as a driving force for mass transport, which results in the increased particle size. Similar effects were observed by Antolini et al. on the grain growth of $LiNiO_2$ at high temperatures.[132]

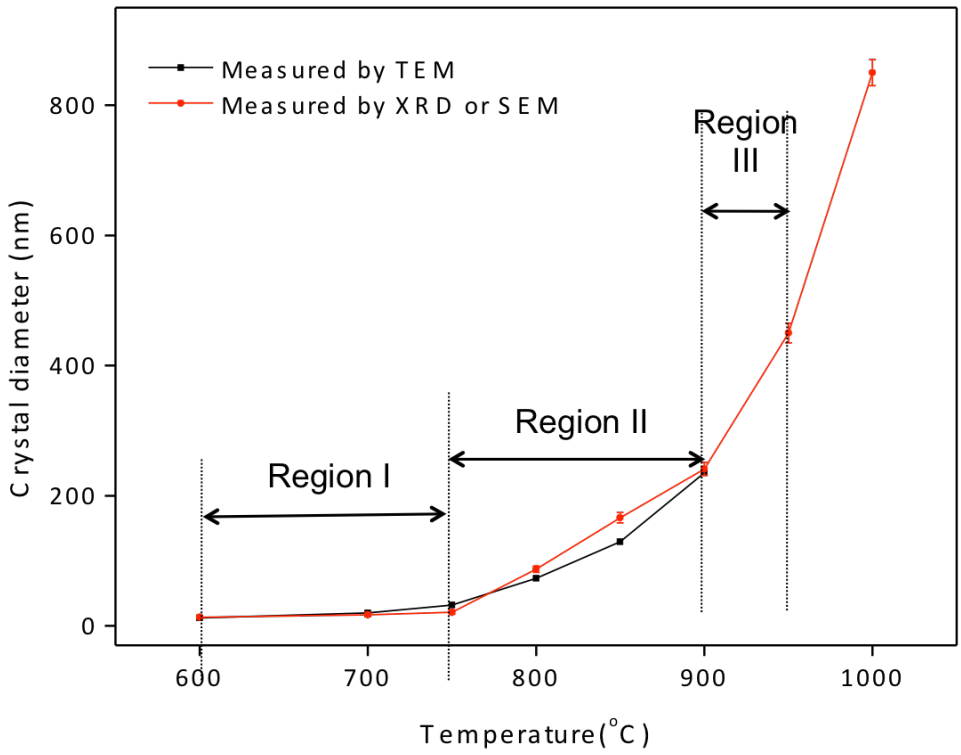

Figure 19. Crystal diameters of L333 annealed for 3 hours at temperatures from 600°C – 1000°C. 3 separate growth regions are observed.

Figure 20 depicts bright-field TEM micrographs of $Li[Ni_{1/3}Co_{1/3}Mn_{1/3}]O_2$ annealed at 800°C for different durations. The crystal diameters increase from 57 nm ± 3 nm (0.5 hours) to 169 nm ± 11 nm (24 hours) and demonstrate good uniformity. The micrographs also confirm the single crystalline nature of the particles observed by SEM.

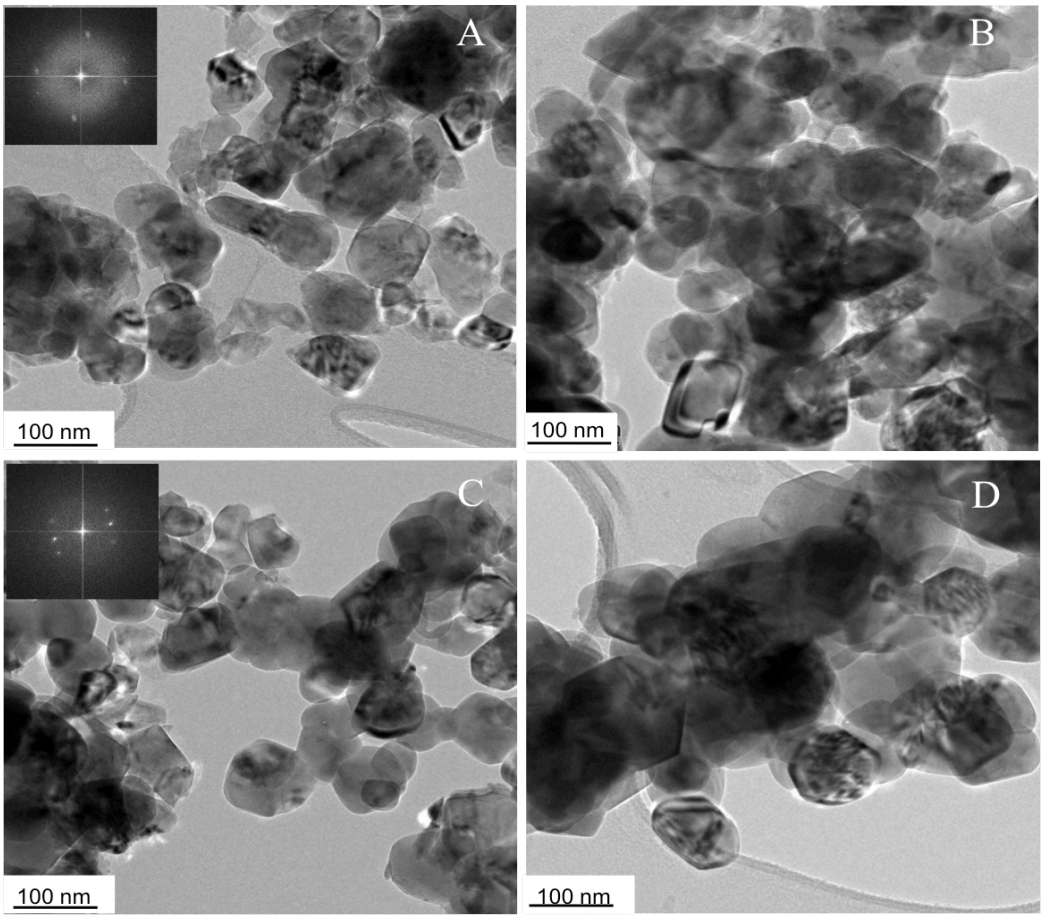

Figure 20. Bright-field TEM micrographs of $Li[Ni_{1/3}Co_{1/3}Mn_{1/3}]O_2$ annealed at 800°C for (A) 0.5 hour, (B) 1 hour, (C) 3 hours, and (D) 6 hours. Fast fourier transforms are inserted in (A) and (C).

2.4. Growth Mechanisms

Based on SEM and TEM observations, it appears that there are 3 separate growth regimes (highlighted in Figure 19) during the L333 annealing process. In order to investigate the crystal growth mechanisms within these regions, we calculated the crystal diameters of the specimens either through X-ray diffraction measurements (i.e., via the Scherer equation[122] utilizing the full width at half maximum, FWHM) or through direct crystal measurement of SEM images (at crystal diameters greater than 100nm).

We plot the ln (crystal diameter) vs. ln (time) for the samples annealed at different temperatures, which are shown in Figure 21. By fitting these curves, we obtain a linear relationship between ln (time) and ln (crystal diameter) which, through theory developed by Lifshitz, Slyozov, Wagner (LSW)[133, 134], describes the growth of the average crystallite size, *G*, with time, *t*, by Eq. (6)

$$D^n - D_0^n = kt \tag{6}$$

Here, D_0 is the initial crystallite size, *k* is a temperature-dependent parameter of the crystal growth rate, and n is an exponent, which describes the rate-controlling mechanism.

As a generalization, Eq. (6) can be rearranged and written as Eq. (7)[135-137]

$$D - D_0 = kt^{1/n} \tag{7}$$

Taking the natural log of Eq. (2), we obtain Eq. (8):

$$\ln (D - D_0) = \ln k + 1/n \ln t \tag{8}$$

Since D_0 is the initial grain diameter, it is found that when ln D is plotted versus ln time, a straight line is obtained (Figure 21) as stated above.

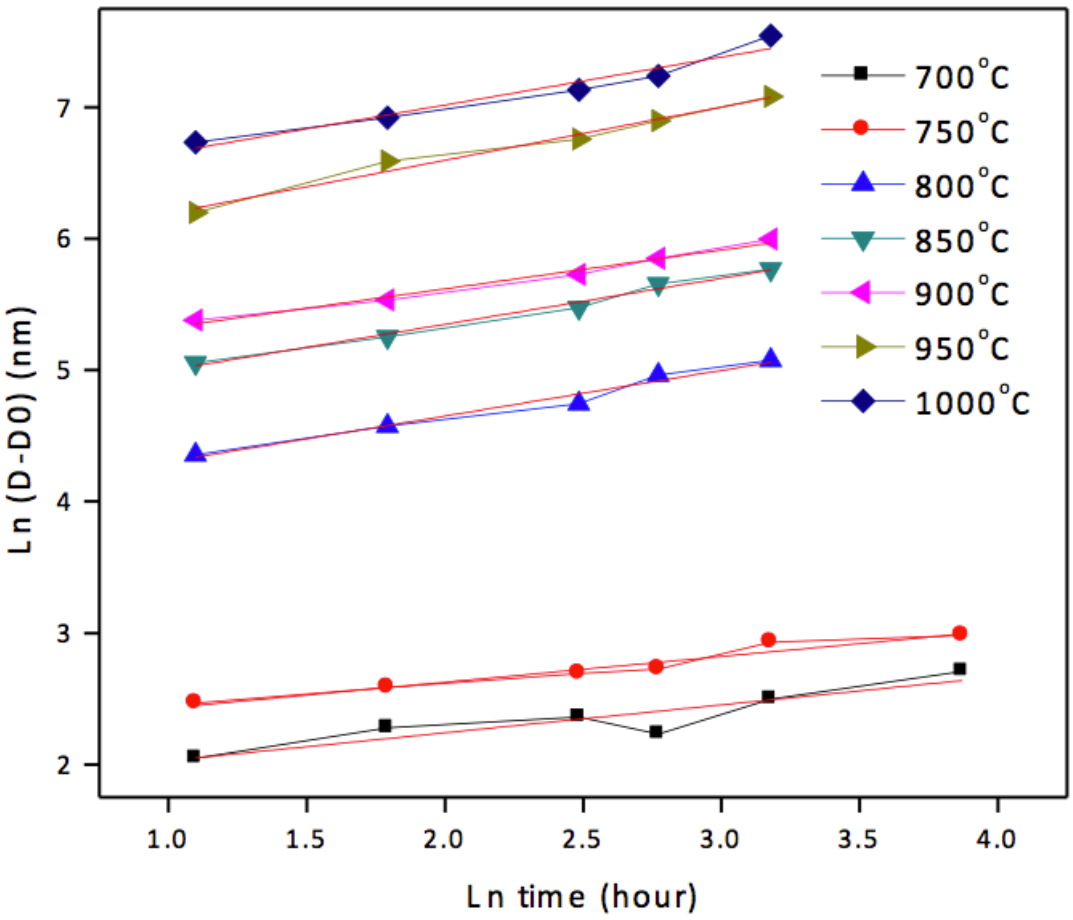

Figure 21. Relationship between crystal diameter and annealing time for samples annealed in air from 700°C to 1000°C.

We obtain both 1/n and ln *k* values from the slope and intercepts of the observed straight line, respectively. Frequently, the slope of the curve plotted in this way is less than 0.5, usually falling between 0.1 and 0.5. This may be due to a small initial crystallite size, D_0 (in our case was calculated to be 9 nm from L333 formed at 400°C) or due to the presence of inclusions or solute segregation, which inhibits grain growth, especially at low temperatures.[136] Table 4 depicts the values of the rate-controlling mechanism exponent, 1/n and the crystal growth rate, ln *k*. As expected, we can see with the increase of temperature, the values of both 1/n and ln k increase.

Table 4. Grain growth parameters at different temperatures.

Temperature (°C)	1/n	ln k
700	0.21 ± 0.05	1.81 ± 0.13
750	0.20 ± 0.02	2.23 ± 0.06
800	0.35 ± 0.03	3.96 ± 0.07
850	0.35 ± 0.02	4.65 ± 0.05
900	0.39 ± 0.02	4.78 ± 0.06
950	0.44 ± 0.02	5.68 ± 0.05
1000	0.48 ± 0.05	5.97 ± 0.11

As mentioned previously, we observe three primary growth regions in our annealing schedule. In region 1 (i.e., 600°C – 750°C), there is almost no grain growth as well as a small rate-controlling mechanism exponent 1/n data (1/n = 0.2). Here, we suspect that the crystal growth mechanism at this temperature range would likely be due to surface diffusion. In Regions II and III, we observe different grain growth behavior. In the temperature range from 800°C to 900°C, we determined that n = 3, indicating the growth is controlled by the volume diffusion of ions within the matrix. At temperatures from 900°C to 1000°C, n = 2, indicating that crystal growth is controlled by the diffusion of ions along the matrix-particle boundary.[138-145] We also observe triple grain junctions at 950°C (Figure 17e) that are indicative of a metastable equilibrium for the L333 system.[133]

Based on our observations, we find that the atomic diffusion across the grain boundary is a simple activated process. Thus, k can be written as:

$$k=k_0\exp(-E_a/RT) \quad (9)$$

$$\ln k=\ln k_0-E_a/RT \quad (10)$$

where, E_a is the activation energy for the process, T is the absolute temperature and R is the gas constant. Thus, the activation energy for crystal growth can be derived from the ln k vs. $1/T$ plot (Eq. 10). We calculated the activation energy in the temperature range of 800°C – 900°C to be 109 ± 17 kJ/mol and 162 ± 25 kJ/mol in the temperature range of 900°C – 1000°C. The calculated activation energies at these temperatures match the observed diffusion mechanisms within these temperature ranges.

2.5. Conclusions

We have successfully synthesized $Li[Ni_{1/3}Co_{1/3}Mn_{1/3}]O_2$ through a two step co-precipitation and annealing method, investigating the crystal growth processes at different temperatures. At temperatures below 750°C, surface diffusion is expected to be the dominant growth mechanism based on minimal crystal growth and a small rate-controlling exponent 1/n. As the annealing temperature is increased (i.e., 800°C – 900°C), crystal growth is controlled by the volume diffusion, while grain boundary diffusion is the predominant mechanism for the temperature range of 900°C – 1000°C. Based on these results, we can establish synthesis and annealing parameters to optimize crystal size and perhaps, control over morphological features, both of which are crucial towards

enhancing rate capabilities, energy densities and cycling stability of future Li-ion batteries.

Chapter 3.

Crystal Structure and Size Effect on the Performance Degradation of $Li[Ni_{1/3}Co_{1/3}Mn_{1/3}]O_2$ as a Cathode Material for Lithium Ion Batteries

To be submitted to *Journal of Power Sources*. Unpublished work copyright (2014) ScienceDirect.

Jianxin Zhu, Kevin Yoo, Akhila Denduluri, Wenting Hou, Juchen Guo and David Kisailus. Crystal Structure and Size Effect on the Performance Degradation of $Li[Ni_{1/3}Co_{1/3}Mn_{1/3}]O_2$ as a Cathode Material for Lithium Ion Batteries. Journal of Power Sources 2014

ABSTRACT:

We have investigated the effects of crystal structure and size of $Li[Ni_{1/3}Co_{1/3}Mn_{1/3}]O_2$ (L333) cathodes on the performance of lithium ion batteries. The cation ordering, crystal structure, size and morphology were monitored as a function of annealing temperature and analyzed by X-ray diffraction (XRD) and scanning electron microscopy (SEM). Electrochemical performance were studied by cyclic voltammograms (CVs), charge-discharge tests and electrochemical impedance spectroscopy (EIS). We investigated the effect of cation ordering and crystal size, which increased with increasing annealing temperatures, on their electrochemical performance. With increasing annealing temperatures, L333 exhibits higher cation ordering which subsequently benefits the cell performance. Concurrently, the higher annealing temperatures yielded larger crystal sizes, which resulted in the decrease of high rate discharge capacity. The L333 cathode underwent an increase in lattice parameter and volume expansion after cycling for all samples with various crystal sizes. Samples with the largest crystal sizes showed the most significant structural changes due to the lower strain accommodation. The lattice parameter in the "c" direction demonstrated a larger change compared to "a", indicating an anisotropic expansion. The resistance increase during cycling furthermore confirmed the performance degradation in the L333 materials.

3.1. Introduction

$Li[Ni_{1/3}Co_{1/3}Mn_{1/3}]O_2$ (L333) is one of the promising cathodes used in lithium ion batteries, as it combines the advantages of high specific capacity, low cost, long cyclic

life, and good structural and thermal stability.[109-112] The performance of $Li[Ni_{1/3}Co_{1/3}Mn_{1/3}]O_2$ greatly depend on the synthesis method. This is because the phase, crystal size, particle morphology, surface area and cation mixing all play a role on the performance and are related to the synthesis route.[112, 146] There are a variety of synthesis methods including coprecipitation,[147] sol-gel,[148] solid-state,[149] hydrothermal,[150] microemulsion,[151] and pyrolysis methods.[152] While there has been a focus on improving performance by introducing novel synthesis methods, coatings and doping, it's also important and necessary to study the performance degradation mechanisms. Manthiram et al.[153] discussed the irreversible capacity loss after the first cycle in layered $LiNi_{1/3}Co_{1/3}Mn_{1/3}O_2$ cathodes at various annealing temperatures. Recently, Ghosh et al.[154] reported the relationship of crystal structure with calcination conditions using oxalate precursors to synthesize $LiNi_{1/3}Co_{1/3}Mn_{1/3}O_2$ cathodes. However, there is very limited information about details of the performance degradation on $Li[Ni_{1/3}Co_{1/3}Mn_{1/3}]O_2$ cathodes. Coprecipitation synthesis method is the most popular method due to its low cost, experimental flexibility and scalability. Based on our previous crystal growth mechanism studies of L333 synthesized by the coprecipitation system,[155] we have continued a thorough investigation of the structure-performance relationship, which is of fundamental importance, not only for its intrinsic scientific interest, but also for its technological significance.[120, 121]

Here, we have synthesized $Li[Ni_{1/3}Co_{1/3}Mn_{1/3}]O_2$ by a two-step coprecipitation method and investigated the cathodes performance degradation with various crystal sizes ranging from 20nm - 1μm. The crystallinity is one of the most important factors that can

effect the electrochemical performance. Larger crystal sizes could result in larger strains, leading to degradation of the microstructure. The information revealed by this study will help develop guidelines to control the size and structure more precisely, create design strategies for cathodes that will enable high efficiency lithium ion transport and extended lifetime batteries.

3.2. Experimental Section

3.2.1 Material synthesis

L333 powders were prepared using a two-step method (see the details in Figure 14). Stoichiometric amounts of nickel, cobalt and manganese nitrates (99.5% purity, Aldrich Chemical Co.) were thoroughly dissolved in deionized water to achieve a homogeneously mixed 100mM solution, followed by adding 2M NaOH to adjust the solution pH to 10, thus, inducing precipitation. The resultant suspension was subsequently stirred at 600 rpm under a nitrogen atmosphere at room temperature for 1 hour. The $(Ni_{1/3}Co_{1/3}Mn_{1/3})(OH)_2$ precipitates (i.e., precursor) were washed with DI water and pure ethanol, then dried under vacuum at 70°C for 12 hours. The precursor was then mixed with a 5% excess of $LiOH{\cdot}H_2O$ and subsequently ground with a mortar and pestle. The mixture was placed in an alumina boat and annealed in a tube furnace at different temperatures (i.e., 750°C – 1000°C) for 3 hours in air.

3.2.2 Material characterization

Phase identification was determined by X-ray diffraction analysis (XRD, PANalytical Empyrean) using Ni-filtered Cu Kα radiation at 45KV and 40mA within the

10-70^{o} 2θ range. Using the resulting XRD diffraction patterns, crystallite diameters were calculated based on the Scherer formula. Particle sizes and morphologies were observed using a scanning electron microscope (SEM, FEI XL30) at 10 kV accelerating voltage. The surface areas of each sample were determined via BET nitrogen adsorption at 77K using a Micromeritics Tristar 3000.

3.2.3 Electrochemical performance

For the electrochemical characterization, as-synthesized $Li[Ni_{1/3}Co_{1/3}Mn_{1/3}]O_2$ powder, conductive carbon black (Super P), and polyvinylidene fluoride (PVDF) (70:20:10 in wt.%) were mixed in N-methylpyrrolidone (NMP) to produce a slurry. This viscous slurry was subsequently coated on an aluminum foil current collector. The coated film was dried in the vacuum oven at 100°C for 12 hours. A R2032 type of coin cell was assembled in an argon-filled glove box, consisting of the prepared positive electrode, lithium metal foil as the counter electrode, Celgard polymer as a separator and 1.0 M $LiPF_6$ in ethylene carbonate (EC)–diethyl carbonate (DEC) (50:50 in vol.%) as the electrolyte solution. The loading of the active material was 2 mg/cm^2. The cyclic performance and rate capability of batteries were tested using an Arbin battery test system (Arbin Instruments, Model BT2043) in the voltage range of 2.8-4.5 V at 25°C. Cyclic voltammograms (CVs) of $Li[Ni_{1/3}Co_{1/3}Mn_{1/3}]O_2$ were recorded on a VMP3 multichannel electrochemical station in the voltage range of 2.8-4.5V at a scan rate of 0.1 mV/s. The electrochemical impedance spectroscopy (EIS) was conducted on the Gamry electrochemical workstation. The amplitude of the input ac signal was 10 mV, and the frequency range was set between 10 mHz and 1 MHz. The positive electrodes that were

fully discharged at the 1st and 10th cycle, were stored to self-equilibrium for 6 hours before EIS testing.

3.3. Results and Discussion

3.3.1 Characterization of synthesized $Li[Ni_{1/3}Co_{1/3}Mn_{1/3}]O_2$

X-ray diffraction patterns of $Li[Ni_{1/3}Co_{1/3}Mn_{1/3}]O_2$ annealed in air for 3 hours with increasing temperature are shown in Figure 22. All peaks from L333 were indexed on the basis of the hexagonal α-$NaFeO_2$ structure with the $R\bar{3}m$ space group. Indexing of these diffraction patterns confirmed the formation of the layered L333 structure without any detectable impurities. Here we can see that all of the samples showed the doublet peaks for the (006)/(102) at 37°(2θ) and the (108)/(110) reflections at 65°(2θ), an indication of ordering of the hexagonal layered structures.[49] This reduction of cationic mixing enabled the intercalation and deintercalation of lithium ions inside the host matrix, leading to an increase in the electrochemical performance of this cathode material.[124]

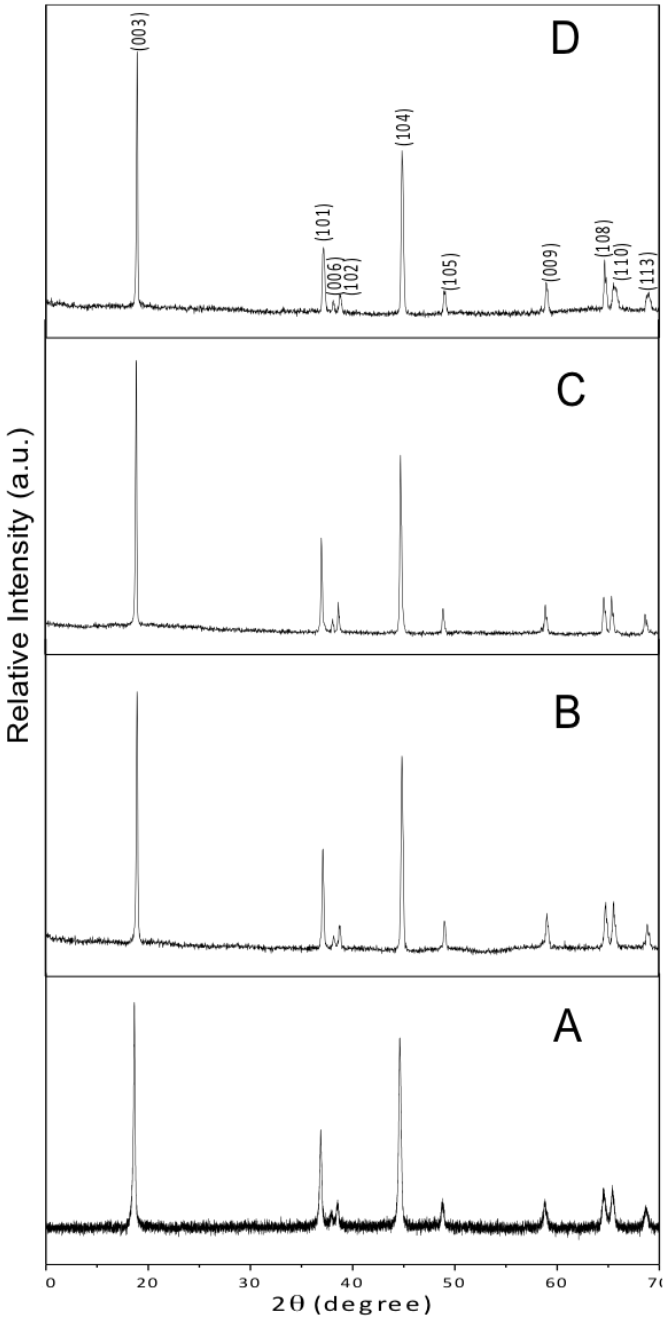

Figure 22. XRD pattern of $Li[Ni_{1/3}Co_{1/3}Mn_{1/3}]O_2$ annealed in air at (A) 750°C, (B) 850°C, (C) 950°C, (D) 1000°C for 3 hours.

It was also noticed from Figure 22 that with increasing annealing temperature, the peak-splitting became clearer indicating an increased cationic ordering. In addition to

peak splitting, the ratio of the intensities of the (003) to (104) indices (i.e., $I_{(003)}/I_{(104)}$) is an indicator of cation mixing in materials with a layered structure. For example, a ratio of $I_{(003)}/I_{(104)}$ >1.2 indicates lower cation mixing with highly ordered structures.[148] From Table 5, we can clearly see that the ratios of $I_{(003)}/I_{(104)}$ at 750°C, 850°C, 950°C and 1000°C are 1.19, 1.28, 1.49 and 1.47 respectively, showing an increase in cationic ordering with temperature and confirming results from the peak splitting analyses.

Table 5. Calculated lattice parameters of $Li(NiCoMn)_{1/3}O_2$.

Annealing temperature (°C)	*a*(Å)	*c*(Å)	*c*/*a*	*unit cell volume* (Å^3)	$I_{(003)}/I_{(104)}$	Average crystal size (nm)	Surface area (m^2/g)
750	2.848(1)	14.014(0)	4.920(3)	98.444(0)	1.19	28.3±6	6.13
850	2.852(0)	14.0571)	4.929(0)	99.009(0)	1.28	166±18	1.58
950	2.856(2)	14.073(3)	4.927(2)	99.425(0)	1.49	458±34	0.41
1000	2.856(1)	14.026(2)	4.911(0)	99.082(3)	1.47	850±50	0.09

SEM micrographs of $Li[Ni_{1/3}Co_{1/3}Mn_{1/3}]O_2$ specimens annealed in air at different temperatures are illustrated in Figure 23. As expected, the micrographs show that the particle sizes increase with increasing annealing temperature. Confirmation of the particle crystallinity was demonstrated by TEM from our previous report,[155] which revealed significant crystal growth of L333 between 750°C and 1000°C. Specifically, specimens heated to 750°C demonstrated a nanocrystalline nature (i.e., crystal diameters less than 50 nm) as determined by analyses of FWHM from x-ray diffraction patterns. These crystals grow in size with increased temperature up to 166 nm by 850°C, 458 nm by 950°C, and eventually to 850 nm by 1000°C (Table 5). It is evident that lower temperature annealing

(i.e., Figures 23A-23C) demonstrate a more uniformed size distribution than at 1000°C (Figure 23D). Thus, the annealing temperature not only affects the crystal size but also changes the particle size dispersity. Based on the above analysis, samples annealed at 850°C and 950°C, which have clear peak splitting, higher cation ordering and uniform crystal sizes, should demonstrate better electrochemical performance.

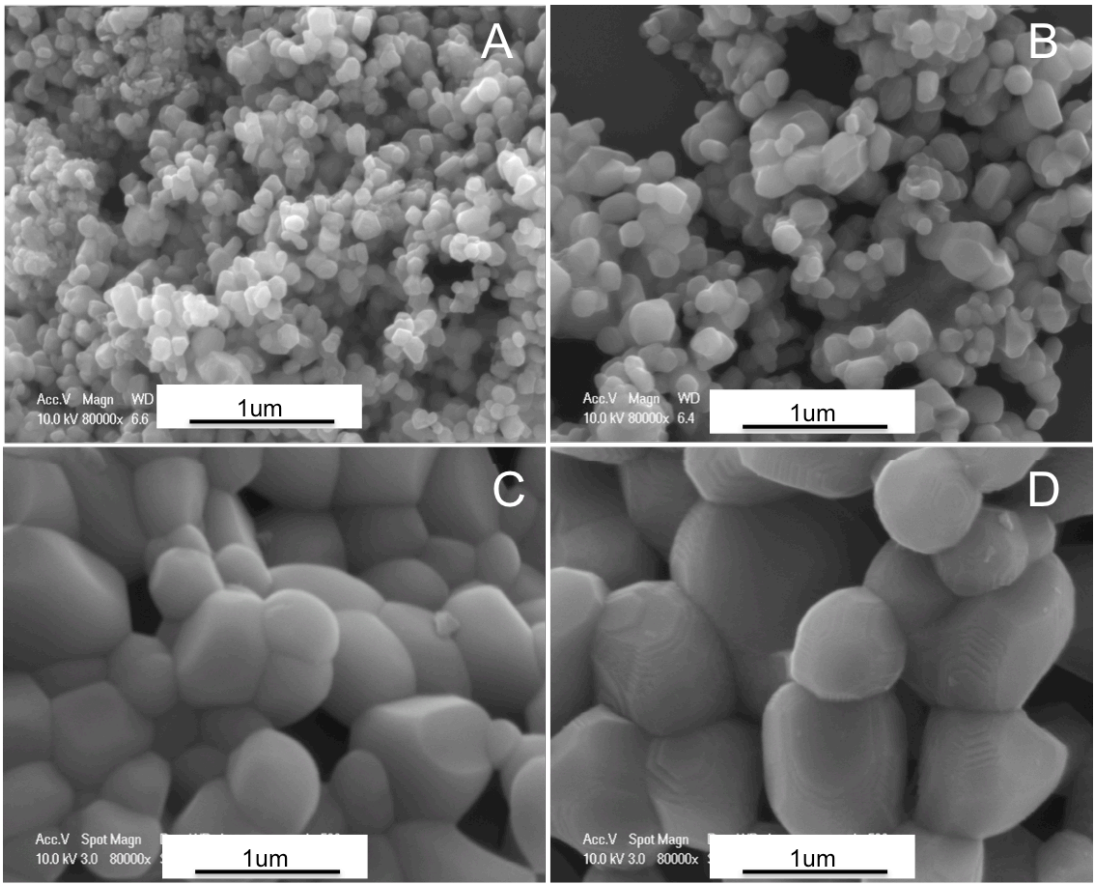

Figure 23. SEM micrographs of $Li[Ni_{1/3}Co_{1/3}Mn_{1/3}]O_2$ annealed in air at (A) 750 °C, (B) 850 °C, (C) 950 °C, (D) 1000 °C for 3 hours.

3.3.2 Electrochemical performance

Figure 24 shows representative CV curves of samples annealed under different temperatures. Each of these curves display only one oxidation peak and reduction peak,

corresponding to the charge/discharge reactions of the Ni^{2+}/Ni^{4+} redox couple.[156, 157] The lack of a peak at 3V indicates the absence of Mn^{3+} in the as-synthesized materials.[158, 159] The potential separations between the anode and cathode peaks are 0.12, 0.21, 0.24 and 0.28 V for samples annealed at 750°C, 850°C, 950°C and 1000°C, respectively. In addition, samples treated at 850°C and 950°C display the highest peak currents (0.19 A/g, and 0.16 A/g) compared to samples annealed at 750°C and 1000°C. It is known that smaller voltage differences between the charge and discharge as well as higher peak currents indicate better electrode reaction kinetics and rate performance.[160, 161]

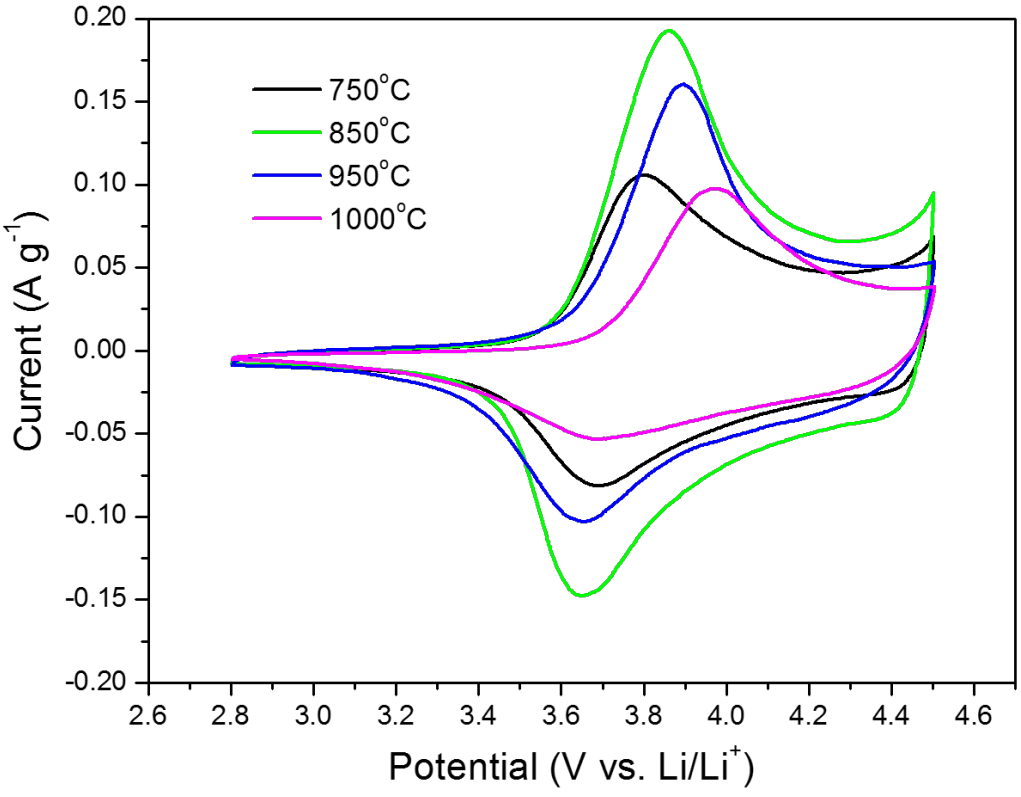

Figure 24. CV profiles of $Li[Ni_{1/3}Co_{1/3}Mn_{1/3}]O_2$ (annealed in air at various temperatures) in the voltage range of 2.8-4.5V at a scan rate of 0.1mV/s.

The initial charge/discharge profiles of the cells with different L333 cathode crystal sizes are illustrated in Figure 25. The first discharge capacities are 155.1, 204.7, 191.6 and 139.3 mAh/g at 750°C, 850°C, 950°C and 1000 °C, respectively. Here the discharge capacities are comparable or even better than that reported in the literature.[162] The discharge plateaus for 850°C and 950°C samples are longer compared to the other two samples, indicating the increased kinetics of these cathodes with increased annealing temperatures.

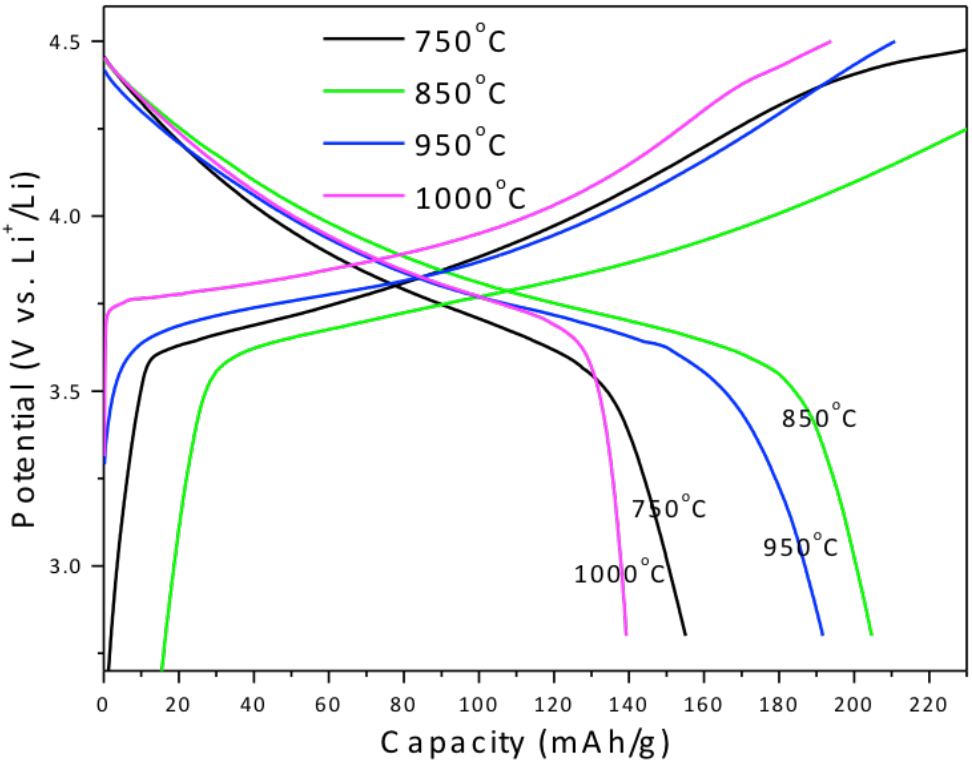

Figure 25. Initial charge/discharge profiles of $Li[Ni_{1/3}Co_{1/3}Mn_{1/3}]O_2$ samples at $16mAg^{-1}$ (synthesized at different annealing temperatures) in the voltage range 2.8-4.5V.

Further cycling charge-discharge capacities were measured at 0.1C for 10 cycles followed by 10 cycles at 0.2C, 0.5C, 1C and 2C. Figure 26A clearly demonstrates that the sample annealed at 850°C delivers the highest discharge capacity. Although the discharge

capacity inevitably decreases with increasing current density, cathodes annealed at 850°C in air for 3 hours delivered a discharge capacity of 119.9 mAh/g at 2C (Table 6), comparable with the report from the literature for a carbon coated L333 system.[163] By comparing the samples annealed at 950°C and 1000°C, which have similar cation ordering ($I_{(003)}/I_{(104)}$ =1.49 and 1.47, respectively), the smaller crystal sizes (458 nm at 950°C) delivers a higher capacity than larger ones (850 nm at 1000°C).

Table 6. Specific capacities for $Li[Ni_{1/3}Co_{1/3}Mn_{1/3}]O_2$ cathodes annealed at various temperatures.

Annealing temperature (°C)	Specific capacity (mAh/g)				
	0.1C	0.2C	0.5C	1C	2C
750	155.05	127.03	107.54	89.02	72.46
850	204.77	188.26	162.99	144.84	119.92
950	191.61	172.17	145.62	116.60	79.30
1000	139.28	108.47	82.30	63.44	36.68

Further calculations (Table 6) show the capacity difference (around 15mAh/g) is smaller at low current densities (from 0.1 to 0.5 C) for 850°C and 950°C, while it increases to 30mAh/g at 1C and 40mAh/g at 2C. Therefore, the smaller crystal size is beneficial under high rates. Figure 26B displays the cycling stability at 0.1C for these samples. Clearly, the 850°C and 950°C samples carry larger discharge capacities with higher capacity retention (84% for 850°C and 88% for 950°C) compared with the other two samples (81% for 750°C and 79% for 1000°C).

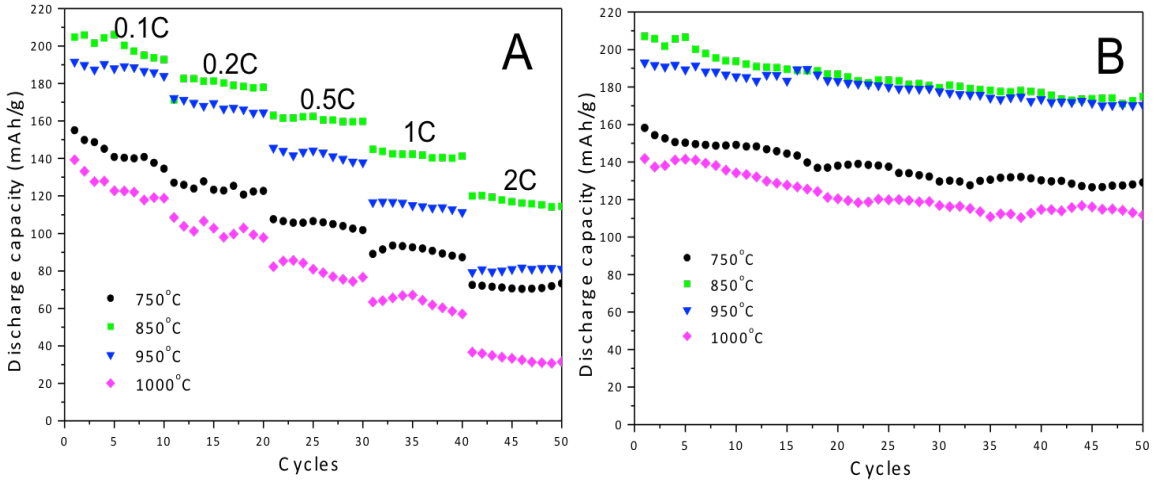

Figure 26. Cycling performance of $Li[Ni_{1/3}Co_{1/3}Mn_{1/3}]O_2$ cathodes between 2.8 and 4.5V (vs. Li^+/Li) (A) at different current rates (0.1C, 0.2C, 0.5C, 1C and 2C), (B) at 0.1C for 50 cycles.

3.3.3 Discussion of performance degradation

In order to investigate the performance degradation mechanisms for $Li[Ni_{1/3}Co_{1/3}Mn_{1/3}]O_2$ cathodes annealed at different temperatures, we disassembled the cells after 50 cycles and collected the cathode materials from the Al foil. The mixture was rinsed with NMP several times to remove the PVDF binder and the remaining organic solvents from the electrolyte. Then the material was dried in the vacuum oven for the XRD and SEM characterization. Figure 27 demonstrates the SEM micrographs for samples after disassembling the cell. Based on analyses by EDS, smaller particles in each micrograph are mostly carbon that was mixed during the cell preparation. The particles that were annealed at 750°C and 850°C did not show obvious changes (Figure 27A and 27B, respectively). Small cracks appeared in particles at 950°C (Figure 27C) and the significantly larger cracks were observed at 1000°C (Figure 27D). In order to study the

crystal microstructure change, we conducted the further XRD analyses to calculate the lattice diameters, volume changes, etc.

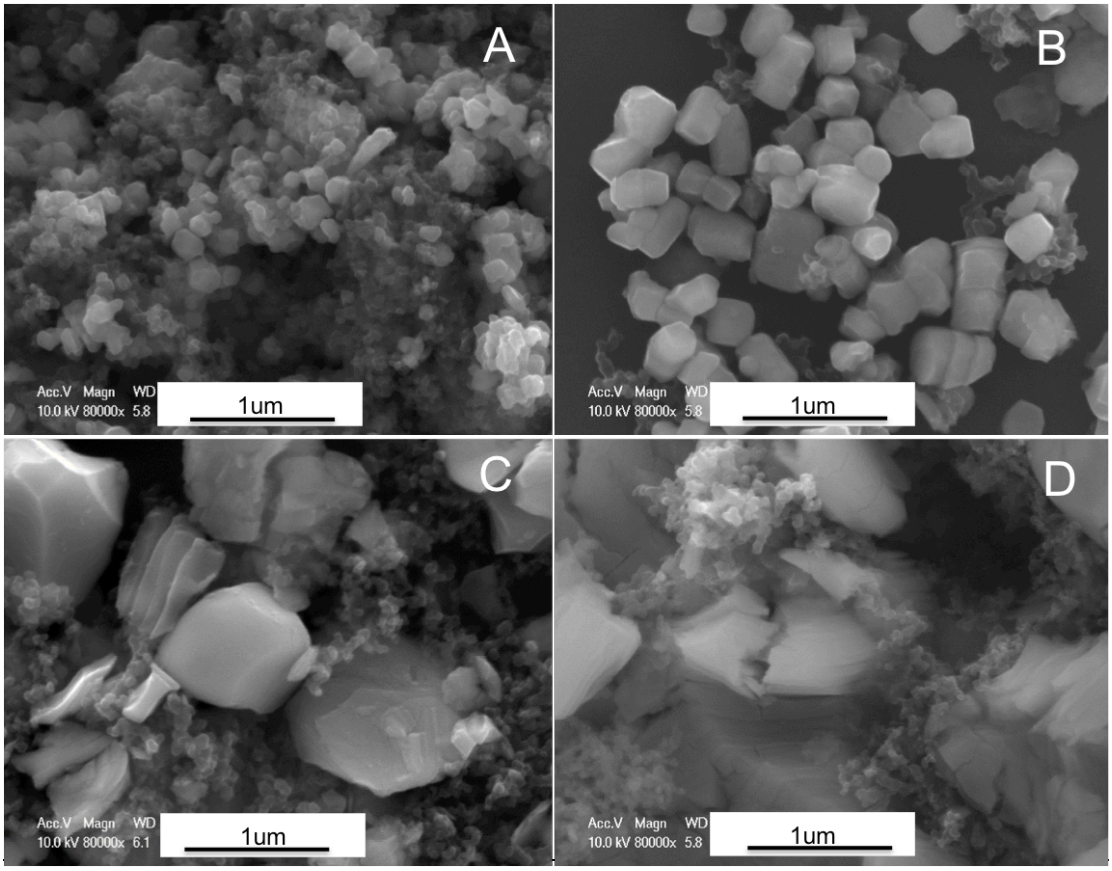

Figure 27. SEM micrographs of $Li[Ni_{1/3}Co_{1/3}Mn_{1/3}]O_2$ cathode particles, annealed in air at (A) 750°C, (B) 850°C, (C) 950°C, (D) 1000°C, and removed from cells after 50 cycles.

Figure 28 show the X-ray diffraction patterns for non-cycled $Li[Ni_{1/3}Co_{1/3}Mn_{1/3}]O_2$ samples (blue line) and after 50 cycles (black line). It can be seen that all of the peaks shifted to lower 2-theta values after cycling, indicating the increased lattice parameter and expanded volume. As we discussed earlier, the peak splitting for (006)/(102) at 37°(2θ) and (108)/(110) at 65°(2θ) reflected a well-ordered layered structure. After 50 cycles, these extent of splitting of peaks did not appear to change for specimens annealed at 750°C and 850°C. However, the intensity of the splitting

decreased for the sample annealed at 950°C (Figure 28C), and was especially significant in the first peak splitting (around 37°). The sample annealed at 1000°C (Figure 28D) showed a further decrease in peak intensity, with almost no splitting observed. These analyses are consistent with our SEM observations.

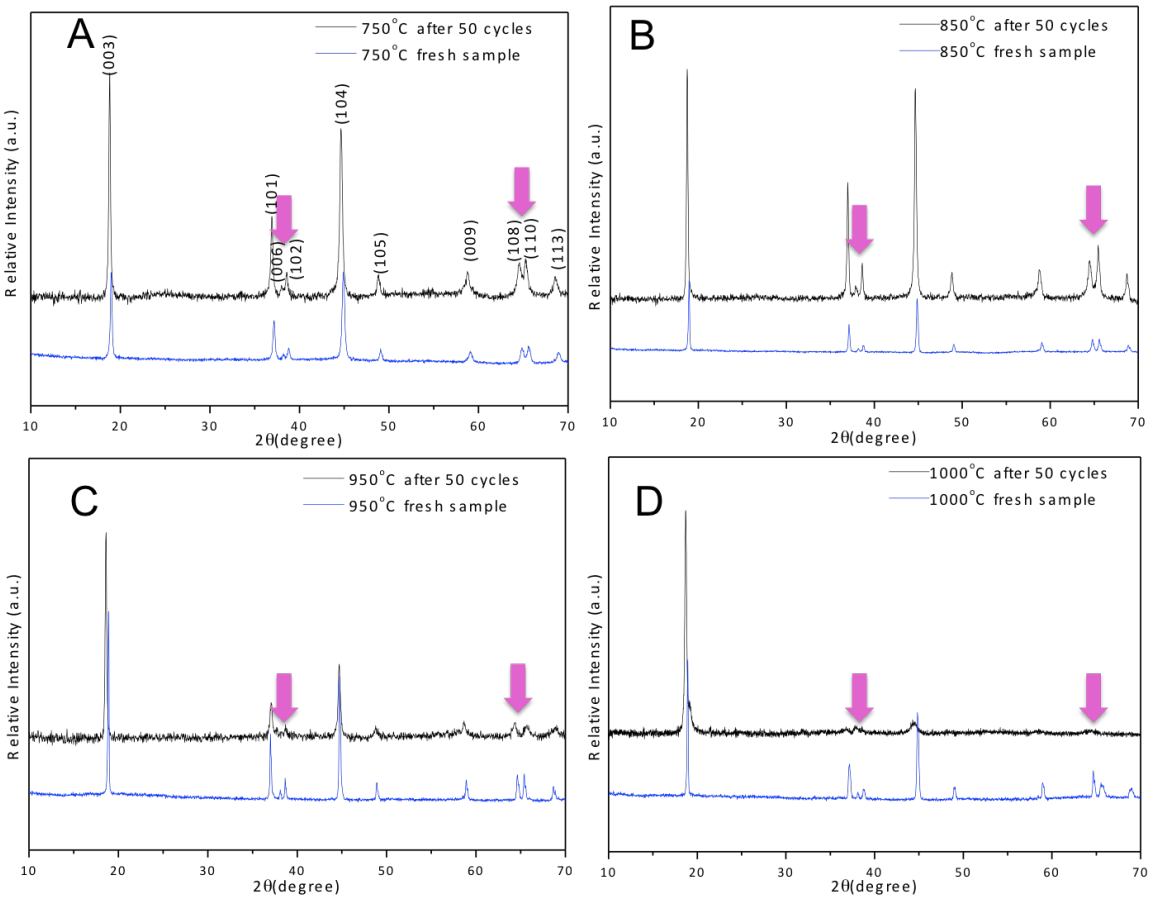

Figure 28. XRD pattern comparison of $Li[Ni_{1/3}Co_{1/3}Mn_{1/3}]O_2$ samples annealed in air at: A 750°C, B 850°C, C 950°C, D 1000°C before (blue) and after (black) cycling.

Detailed lattice parameters are listed in Table 7, from which we can see the 1000°C cathode shows the largest lattice parameter increase and volume expansion (2.15%), while samples annealed at 850°C and 950°C display minimal changes. Here, we also observed that the percent change in the "a" lattice parameter (i.e., <0.5%) is

significantly less compared to those occurring in the "c" r(~1 or >1%), indicating anisotropic degradation in the L333 system. It is known that lithium ions move along the ab plane in L333 during lithiation and delithiation. Thus, we suspect parameter c change in this crystal structure degradation is comparably a mild effect to the performance compared to changes along a and b. By combining the above SEM and XRD analyses, smaller particle sizes will yield smaller structural changes and thus, better strain accommodation, which is also observed in Si-based anodes.[164-166] According to Liu et al. reporting,[164] there exists a critical particle size of ~150 nm below which cracking did not occur, and above which surface cracking and particle fracture took place upon lithiation. They discussed that the unexpected surface cracking is attributed to the development of hoop tension in the surface layer, resulting from a unique lithiation mechanism in crystalline Si nanoparticles by means of motion of a two-phase interface. This might also be true for our NCM system based on the similar results, which is currently under investigation. One exception was the sample annealed at 750°C. It is believed that reduced ordering in the non-cycled layered structure ($I_{(003)}/I_{(104)} = 1.19$) yielded poorer performance compared to samples annealed at 850 and 950°C.

Table 7. Lattice parameters for $Li[Ni_{1/3}Co_{1/3}Mn_{1/3}]O_2$ cathodes after 50 cycles.

Sample	a(Å)	Δa/a(%)	c(Å)	Δc/c(%)	a/c	V(Å^3)	ΔV/V(%)
750°C	2.858(0)	0.35	14.144(0)	0.93	4.949(0)	100.039(1)	1.62
850°C	2.852(1)	0.004	14.189(4)	0.93	4.976(1)	99.915(0)	0.92
950°C	2.859(0)	0.11	14.205(2)	0.94	4.969(0)	100.538(3)	1.12
1000°C	2.868(0)	0.42	14.213(4)	1.33	4.956(7)	101.211(4)	2.15

In order to further investigate the various crystal size effects on the performance, electrochemical impedance spectroscopy were recorded for the 0% state of charge (SOC) samples. Figure 29A shows the impedance after the 1st cycle while Figure 29B represents samples after the 10th cycle. Each curve consists of a semicircle and a straight line, which are interpreted as the resistance of electrolyte "R_e" at high frequency, the resistance of charge-transfer "R_{ct}" for the semicircle at middle frequency and the lithium ion diffusion into the bulk of the electrode material at low frequency for the straight line (also called Warburg diffusion).[167] The numerical value of the diagram on the real axis, Z_{re}, is approximately the R_e and the R_{ct} for the semicircle, which are listed in Table 8.

Table 8. Parameters from the EIS curves.

Annealing temperature (°C)	Resistance (Ω)			
	R_e after 1st	R_e after 10th	R_{ct} after 1st	R_{ct} after 10th
750	1.39	2.88	118.16	175.28
850	1.39	1.33	308.54	616.69
950	1.72	1.55	371.18	761.38
1000	1.40	1.48	843.04	955.57

As we can see from Table 8, R_e did not vary much among different samples. This is because the R_e is only related to the electrolyte and the contact resistance. After 10 cycles, the R_e value only changed for the sample annealed at 750°C (with smallest crystal size). The high radius of curvature in these small crystals is the likely reason for the high reactivity between electrolyte and active material. This high reactivity likely induced the formation of a solid electrolyte interfaces (SEI), but did not occur with samples with larger crystal sizes. The R_{ct} increased with annealing temperature because of the increased crystal size (28 nm at 750°C, 166 nm at 850°C, 458 nm at 950°C, and 850 nm at 1000°C). We also observe that R_{ct} increases after cycling, which helps shed light on the decreased performance. Among these Rct changes, samples annealed at 750°C and 1000°C did not change as much as samples annealed at 850°C and 950°C. According to Wohlfahrt-Mehrens,[168] impedance increases are caused by the loss of contact between the electrolyte and electrode. Here the sample annealed at 750°C has a smaller crystal size (and higher surface/volume ratio), and likely to have good contact with the electrolyte. The sample annealed at 1000°C displayed obvious cracks in the particle, breaking into smaller pieces. We think this might help the contact between electrode and electrolyte.

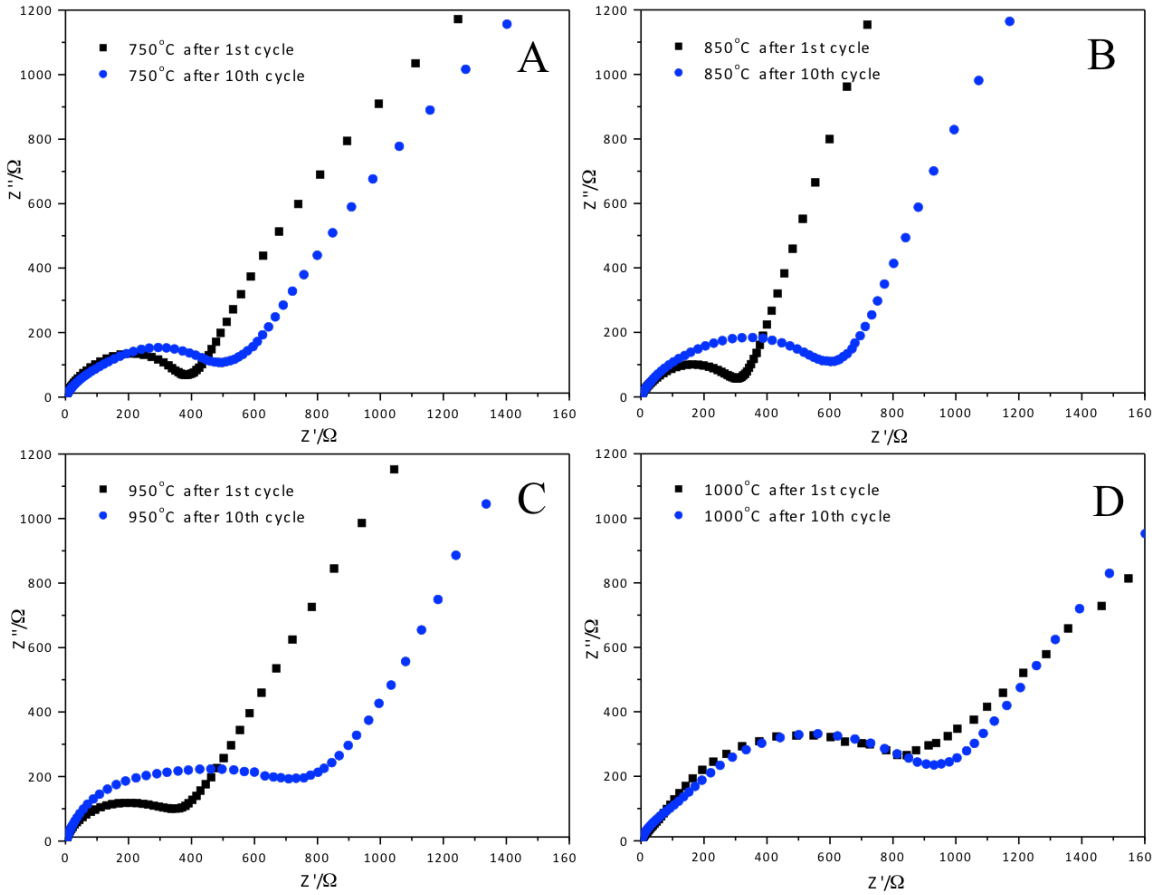

Figure 29. EIS micrographs of $Li[Ni_{1/3}Co_{1/3}Mn_{1/3}]O_2$ cathodes after 50 cycles for samples annealed in air at: A 750°C, B 850°C, C 950°C, D 1000°C.

3.4. Conclusions

We have systematically investigated the effects of crystal structure and size on the performance of $Li[Ni_{1/3}Co_{1/3}Mn_{1/3}]O_2$ cathodes. With increasing annealing temperature, $Li[Ni_{1/3}Co_{1/3}Mn_{1/3}]O_2$ has the increased ordering of the hexagonal α-$NaFeO_2$ layered structure and increased crystallite sizes. The higher cationic ordering provides better performance for the crystal sizes below 500 nm. Beyond that, crystal size has a key effect on the performance, especially for the high current density discharge capacity. Due to the lower strain accommodation within the larger particles, cracks form in the

microstructures during lithiation/delithiation, which results in a fast capacity fade. EIS studies show that a charge-transfer resistance R_{ct} increases with cycles for all sizes of $Li[Ni_{1/3}Co_{1/3}Mn_{1/3}]O_2$ cathodes and explains the capacity retention decrease.

Chapter 4.

Solvothermal Synthesis, Development and Performance of $LiFePO_4$ Nanostructures

Jianxin Zhu, Joseph Fiore, Dongsheng Li, Nichola M. Kinsinger, Qianqian Wang, Elaine DiMasi, Juchen Guo and David Kisailus. Solvothermal Synthesis, Development and Performance of $LiFePO_4$ Nanostructures, Crystal Growth & Design, 2013, 13 (11), pp 4659–4666.

ABSTRACT:

We report the synthesis and nanostructural development of single and polycrystalline $LiFePO_4$ (LFP) nanostructures using solvothermal media (i.e., water-triethylene glycol mixture). Crystal phase and growth behavior were monitored by powder and synchrotron X-ray diffraction as well as transmission electron microscopy (TEM), while particles morphologies were examined using scanning electron microscopy (SEM). Initially, thin (100 nm) platelets of $Fe_3(PO_4)_2 \cdot 8H_2O$ (vivianite, VTE) formed at short reaction times followed by the nucleation of LFP (20 nm particles) on the metastable VTE surfaces. With decreasing pH, primary LFP nanocrystals subsequently aggregated into polycrystalline diamond-like particles via an oriented attachment (OA) process. With increasing reaction time, the solution pH further decreased, leading to a dissolution-recrystallization process (i.e., Ostwald ripening, OR) of the oriented polycrystalline LFP particles to yield uniformly sized, single crystalline $LiFePO_4$. Samples prepared at short reaction durations demonstrated a larger discharge capacity at higher rates compared to the single crystalline particles. This is due to the small size of the primary crystallites within larger secondary $LiFePO_4$ particles, which reduced the lithium ion diffusion path while subsequently maintained a high tap density. Understanding the relationship between solution conditions and nanostructural development as well as performance revealed by this study will help to develop synthetic guidelines to enable efficient lithium ion battery performance.

4.1 Introduction

As fossil fuel supplies are depleted, efforts to create new and renewable energy sources are being implemented. In addition to the need for renewable energy conversion technologies, there is an urgency for enhanced energy storage for municipal energy storage, electric vehicles and portable devices. Rechargeable lithium ion batteries offer an effective media to store energy. There has been a marked improvement in Li-ion technologies compared to other alternatives such as the NiCd (Nickel-Cadmium) or NiMH (Nickel-Metal Hydride) cells. Li-ion cells offer double the specific energy and over three times the energy density versus Ni-H_2 (which use pressurized hydrogen) systems, while providing higher energy efficiency.[169]

Improvement in the material components of Li-ion batteries, specifically the cathode and anode, offers potential to enhance their performance. One such cathode, the olivine-structured lithium iron phosphate ($LiFePO_4$, LFP) was invented and reported by Goodenough et al. more than 15 years ago.[170] Due to its low cost, low toxicity, thermal and chemical stability, and its good cycle stability, it is an excellent candidate as a cathode in rechargeable lithium batteries used in electric vehicles.[170] However, it is hindered by a low rate capacity due to the poor electronic conductivity and low lithium ion diffusivity, which inhibits expanding its commercial potential.[171, 172] In order to overcome this inherent deficiency of LFP, research strategies have focused on utilizing conductive agents (carbon, silver, etc.)[95, 96, 173] to increase the electronic conductivity, and to improve the mobility of lithium ions via cationic doping.[174, 175]

A number of different synthesis methods have been developed to produce controlled LFP including solid phase synthesis,[176, 177] sol-gel process,[178] solution co-precipitation,[179] and solvothermal treatments.[180] Solvothermal syntheses, which often operate under higher pressures, offer the potential to precisely control the size, shape distribution, and crystallinity of particles at low to moderate temperatures.[101, 180-185] Solvents used in the syntheses of LFP have included benzyl alcohol[180], tetraethylene glycol (TEG),[181] polyethylene glycol (PEG),[101, 182-184] and triethylene glycol[185]. Triethylene glycol is a transparent, colorless, low-volatility, moderate-viscosity liquid. Under normal conditions, there is no detectable odor. It is completely miscible with water and many organic liquids. Triethylene glycol has properties similar to other glycols and may be used preferentially in applications requiring a higher boiling point, higher molecular weight, or lower volatility than diethylene glycol. Furthermore, triethylene glycol can be used as the reducing agent as it will prevent the oxidation of Fe^{3+} from Fe^{2+}. Lim et al.[185] used pure triethylene glycol to synthesize $LiFePO_4$ and noticed impurities accompanied with the formation of $LiFePO_4$, which they ascribed to as the high boiling point of triethylene glycol.

Here, we modify the solution environment by utilizing a mixture of water and triethylene glycol as the solvent for the first time to synthesize lithium iron phosphate. Recently, Lu et al.[186] reported the mechanism of LFP formation under hydrothermal conditions. However, limited information has been presented to understand the formation mechanism and the resulting crystallinity on the performance in the water-triethylene glycol system. Previous research has revealed the primary lithium-ion insertion pathways

in LFP.[98] Thus, by uncovering the formation mechanism of LFP nanostructures and determining the relationship between the resulting structures and function, there is a great potential to yield highly efficient, long cycle life Li-ion batteries.

4.2 Experimental Section

4.2.1 Synthesis of lithium iron phosphate

LFP nanopowders were prepared using a hydro-solvothermal method. Stoichiometric amounts of $FeSO_4 \cdot 7H_2O$, H_3PO_4 (85 wt.% solution), and $LiOH \cdot H_2O$ with a molar ratio of 1:1:3 were used. Briefly, separate aqueous-based ferrous sulfate and lithium hydroxide solutions were made by dissolving $FeSO_4 \cdot 7H_2O$ and $LiOH \cdot H_2O$ in degassed Milli-Q water, respectively. After adding the lithium hydroxide solution into triethylene glycol, aqueous solutions of H_3PO_4 and ferrous sulfate were subsequently added to achieve a homogeneous 0.1M Fe solution. After vigorous magnetic stirring at room temperature for 10 minutes, a green suspension formed and was transferred into either glass vials (for short duration reactions) or Teflon-lined, stainless steel autoclaves (for extended reaction durations). Reactors were sealed (glass were sealed by melting the tops of reactors with a butane torch) and heated in a convection oven at 160°C for 5 to 900 minutes. After ambient cooling to room temperature, products were centrifuged, washed several times with deionized water and absolute alcohol, and finally dried in vacuum for 5 hours.

4.2.2 Material characterization

Phase identification was determined by X-ray diffraction analysis (XRD, Philips X'Pert) using Cu Kα radiation. Using the resulting XRD diffraction patterns, crystallite diameters were calculated based on the Scherer formula.[122] Particle sizes and morphologies were observed using a scanning electron microscope (SEM, FEI XL30) at 10-20 kV accelerating voltage. A transmission electron microscope (TEM, FEI CM300), operated at 300 kV, was used to identify crystallite size, morphology and phase. Powder synchrotron X-ray diffraction was performed at beam line X6B of the National Synchrotron Light Source (NSLS) in Brookhaven National Laboratory using 19 KeV X-rays and a beam spot focused to 100 μm x 100 μm. In-situ synchrotron X-ray diffraction was performed at beam line X7B using 40KeV with a beam spot of 0.5 x 1.0mm and Perkin Elmer amorphous silicon detector is used to acquire the 2-D x-ray diffraction pattern.

4.2.3 Electrochemical performance

As-synthesized $LiFePO_4$ powder, conductive carbon black (Super P), and polyvinylidene fluoride (PVDF, 70:20:10 wt.%) were mixed in N-methylpyrrolidone (NMP) to produce a slurry. This viscous slurry was subsequently coated on an aluminum foil current collector. The coated film was dried in the vacuum oven at 100°C for 12 hours. Coin cells (R2032 type) were assembled in an argon-filled glove box, consisting of the prepared positive electrode, lithium metal foil as the negative electrode, Celgard polymer as a separator and 1.0 M $LiPF_6$ in ethylene carbonate (EC)–diethyl carbonate (DEC) (50:50 vol.%) as the electrolyte solution. The loading of the active material was

1.5 mg/cm^2. The cyclic performance and rate capability of $LiFePO_4$ batteries were tested using an Arbin battery test system (Arbin Instruments, Model BT2043). Cyclic voltammograms were run on a VMP3 multichannel electrochemical station.

4.3 Results and Discussion

4.3.1 Formation and nanostructural evolution of $LiFePO_4$

4.3.1.1 Precursor

Precursor particles, which formed after 10 minutes of stirring, were collected via centrifugation, washed (as described in 4.2.1) and dried in a vacuum oven at 70°C for 5 hours. SEM (Figure 30A) demonstrates the aggregated nature of the nanoparticles and XRD (Figure 30B) revealed that these nanoparticulate precursor powders consist of ~ 10 nm (as calculated by the Scherer equation) crystallites of Li_3PO_4 (JCPDS #15-0760).

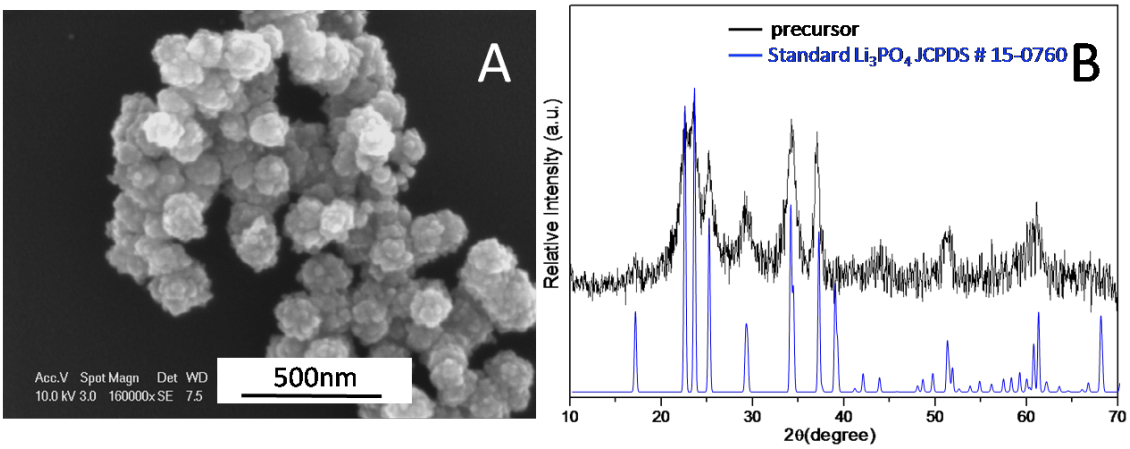

Figure 30. (A) SEM micrograph and (B) XRD pattern of precursor sample indicating the formation of Li_3PO_4 nanocrystals.

4.3.1.2 Formation of $Fe_3(PO_4)_2 \cdot 8H_2O$ (vivianite, VTE) and nucleation of $LiFePO_4$

The precursor-based slurries were subsequently placed in sealed reactors at 160°C. After a 5 minute reaction duration, large plate-like (5 μm x 5 μm x 100 nm thick) nanostructures (Figure 31A) formed with small particles on their surfaces (inset in Figure 31A). Examination of these products by powder XRD (Figure 31B) and synchrotron X-ray analysis (Figure 31C) revealed the formation of crystalline sheets of VTE ($Fe_3(PO_4)_2 \cdot 8H_2O$, JCPDS # 30-0662) as well as small quantities of $LiFePO_4$. The precursor particles, which consisted of Li_3PO_4, dissolve ($K_{sp}=3.2\times10^{-9}$), and in the presence of iron ions yield a less soluble $Fe_3(PO_4)_2 \cdot 8H_2O$ ($K_{sp}=1\times10^{-36}$). In addition, it is noteworthy that the triethylene glycol solvent serves as a reducing agent, providing a favorable environment for vivianite formation.[187, 188]

Interestingly, from the inset of Figure 31A (yellow square), we observed that small particles appear to form at the edges or kinks on the VTE plates. This phenomenon was also observed from bright field TEM in the inset of Figure 31E. Bright field TEM in Figures 31D-31E and the corresponding SAED in Figures 31G - I were used to confirm the phases of both plate-like structures and the small particles on the plate surfaces. The SAED pattern shown in Figure 31G represents the pure platelet region highlighted with a green square. Analysis of this diffraction pattern confirmed the single crystalline nature of pure $Fe_3(PO_4)_2 \cdot 8H_2O$. The SAED pattern shown in Figure 31H represents the region containing the small particles on the platelet surface (highlighted in blue). This diffraction pattern contains both dots and rings, revealing a combination of the nearly single crystalline $Fe_3(PO_4)_2 \cdot 8H_2O$ as well as nanocrystalline $LiFePO_4$ (i.e., the

nanoparticles on the surface of the platelets are $LiFePO_4$). Bright field TEM (Figure 31F) shows only primary and secondary particles without $Fe_3(PO_4)_2 \cdot 8H_2O$ platelets. The corresponding SAED pattern from the circled purple area in Figure 31I confirms pure LFP crystals with a preferred orientation with texture. Here, it is likely that under the reaction conditions, $Fe_3(PO_4)_2 \cdot 8H_2O$ is dissolving (as observed by striations on platelets, Figure 31A), providing high concentrations of nutrient for the nucleation of $LiFePO_4$ near the edge and kink sites.[189]

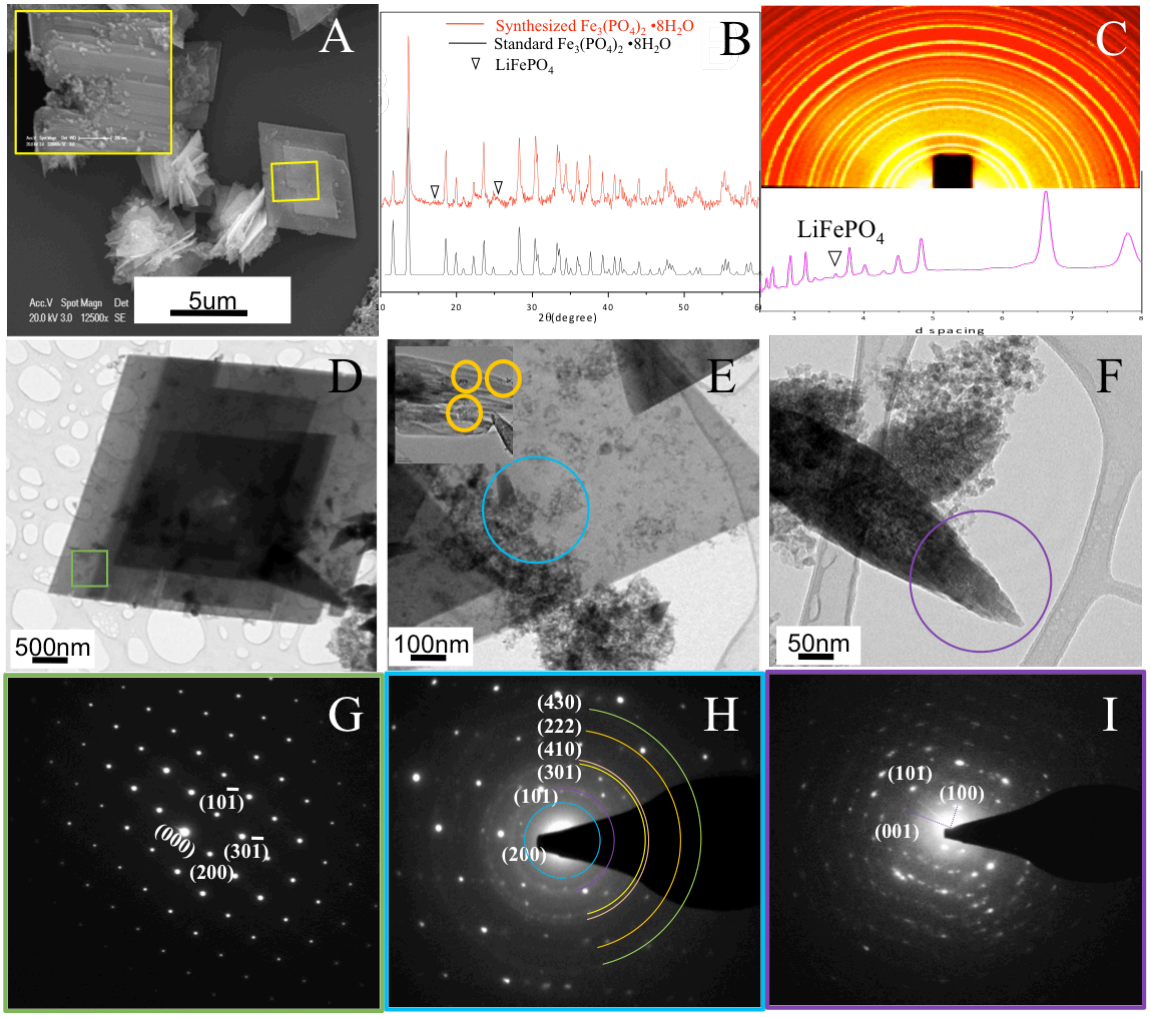

Figure 31. Characterization of the sample synthesized at 160°C for 5 minutes. (A) SEM of the platelet structure, (B) Powder XRD of sample with $Fe_3(PO_4)_2 \cdot 8H_2O$ as a reference, (C) Synchrotron x-ray diffraction of the sample, confirming the VTE phase with little LFP phase (D) Bright-field TEM of the platelet structure (E) Bright-field TEM of the platelet structure with small particles on top (upper left inset), highlighting LFP nanoparticles forming at edges of $Fe_3(PO_4)_2 \cdot 8H_2O$), (G) SAED from clean platelet (green square area) (H) SAED from combination of platelet and nanoparticles (circled blue area), and (I) SAED from completely formed primary particle tail (circled purple area).

In order to further confirm the phase transformation from $Fe_3(PO_4)_2 \cdot 8H_2O$ to $LiFePO_4$, we conducted *in-situ* synchrotron for the mixed precursor solution in a quartz capillary (1mm OD, 0.9 mm ID, 100mm length) with a round bottom. During the heating

process, the other end was sealed under He gas (~ 41-43 psi). The sample was heated according to the profile: 10°C/min from 25°C to 100°C, 2°C/min from 100°C to 160°C, held for 30 minutes duration time at 160°C, then 10°C/min from 160°C to 250°C, then cooled down to room temperature. As we can see from Figure 32, the phase transformation from $Fe_3(PO_4)_2 \cdot 8H_2O$ to LFP occurred between 129°C and 138°C (in 88 seconds). The peak intensities increased quickly in the next two measured synchrotron frames after the phase transformation (i.e., peaks at 149°C and 164°C). After heating for 30 minutes at 160°C, the peak intensity remained stable until 250°C.

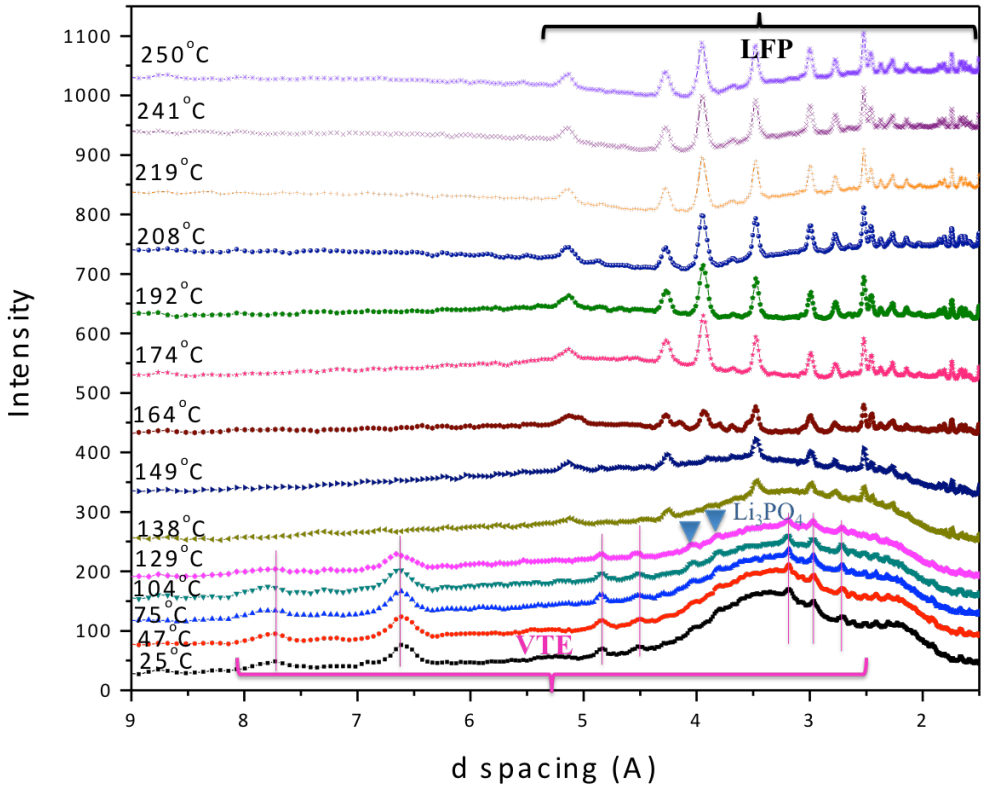

Figure 32. *In-situ* synchrotron monitoring of the phase transformation from $Fe_3(PO_4)_2 \cdot 8H_2O$ (VTE) to $LiFePO_4$ (LFP).

4.3.1.3 Oriented assembly of polycrystalline $LiFePO_4$ (LFP) particles.

After 10 minutes reaction duration at 160°C, particles (Figure 33A) displayed a diamond-like morphology and appeared to be formed by an oriented assembly of primary particles. Pure phase $LiFePO_4$ was detected via XRD (Figure 33B). All the reflections were indexed as an orthorhombic olivine-type structure (JCPDS 81-1173) and no additional impurity phases were observed, confirming the removal of vivianite. Rietveld refinement of the XRD data with the *Pnma* space group gave the following lattice parameters: a = 10.334(1) Å, b = 6.010(1) Å, and c = 4.694(1) Å, which are in good agreement with the reported values (a = 10.332(2) Å, b = 6.005(1) Å, c = 4.693(6) Å) that used a high temperature synthesis method).[190] The crystallite size of the LFP was calculated to be 39 nm using the Scherer equation.[122] Bright field TEM (Figure 33C) was conducted to further investigate the nanostructure of these particles. Electron diffraction (Figure 33D) analysis of one of the particles in Figure 33C revealed a pseudo-single crystal pattern, which consisted of arched (ca. ~ 5°) diffraction spots. This indicates that the larger, secondary diamond-like particles are likely to consist of an oriented assembly of smaller primary particles.

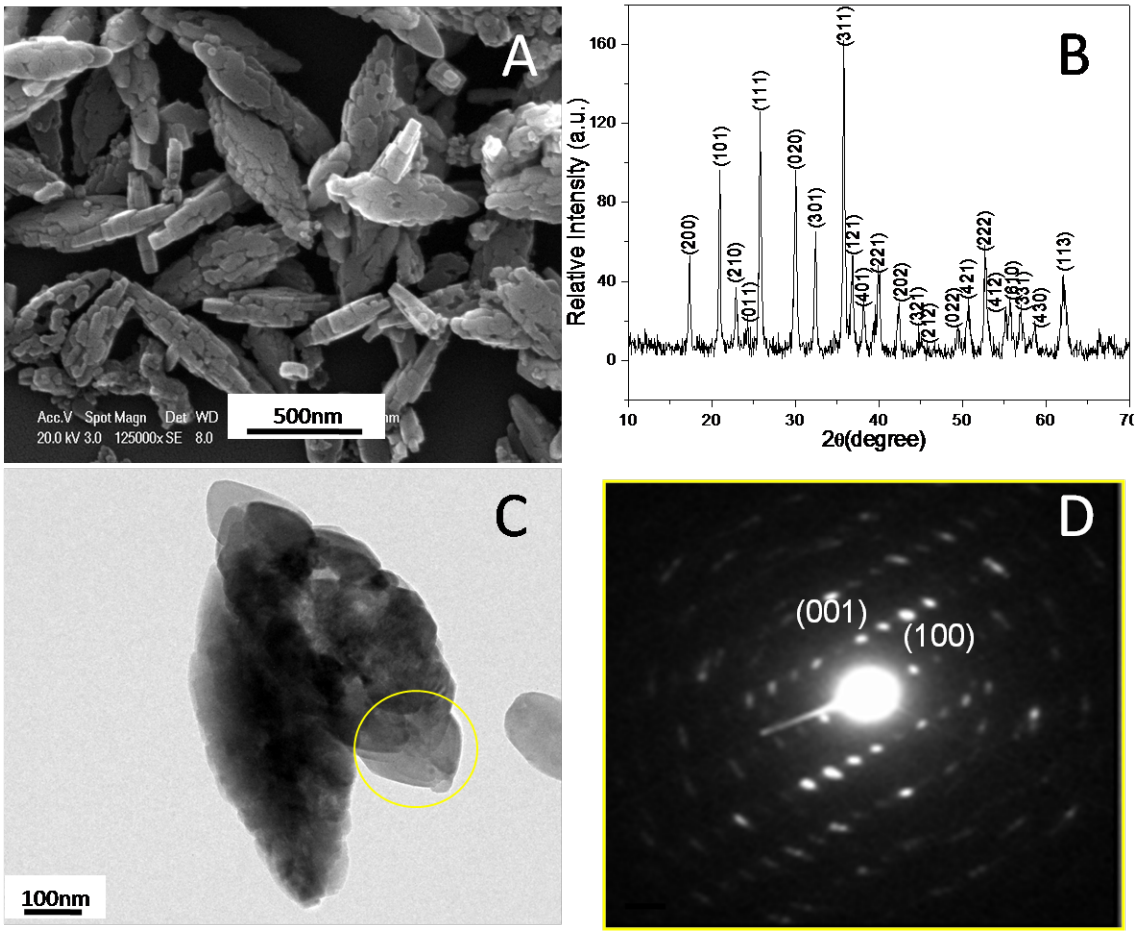

Figure 33. Analyses of $LiFePO_4$ synthesized at 160°C for 10 minutes in a sealed glass reactor. (A) SEM micrograph highlighting the assembled secondary particles of LFP. (B) Powder XRD of sample, (C) Bright field TEM with corresponding (D) SAED from the yellow-circled area.

In order to investigate the potential assembly of primary particles, we interrogated the surface charge of LFP using zeta potential measurements (Figure 34A) to determine their interactions in the reaction suspension. The primary nanoparticles of $LiFePO_4$ initially form at pH ~ 6 (Table 9). Here, these particles are highly negatively charged (i.e., ζ = -52 mV) and electrostatically repel each other. However, as the reaction duration increases, the pH continually decreases (below 5.5). Subsequently, the charge on the particles becomes less negative (i.e., ζ < -20 mV), which enables particles to approach

each other more closely, enabling their assembly.[191, 192] At this stage, the primary LFP particles appear to aggregate in an oriented manner, forming larger diamond-like secondary particles.

Table 9. Reaction pH at different reaction durations (minutes).

Reaction time (minutes)	0	5	10	15	20	60	180	900
pH	5.51	6.05	5.54	5.18	4.83	4.60	4.39	4.30

Additional bright field TEM analysis of one of the secondary particles is shown in Figure 34B. High-resolution TEM imaging (Figure 34C) with the corresponding Fast Fourier Transform (FFT, Figure 34D) of this particle reveals that primary nanoparticles are indeed attached to each other in an oriented manner and are aligned in [001] and [100] directions, with the (010) plane as the primary exposed surface. Ceder et al.[193] calculated surface energies of the olivine structured $LiFePO_4$ using density functional theory (DFT) within the generalized gradient approximation (GGA) + U framework. Their results show that the low-energy surfaces are in the [100], [010], [011], [101] and [201] directions. Islam et al.[194] reported that the (010) and (100) planes have the lowest attachment energies in their simulation, which corroborates our observations of diamond-like structures elongated in [001] direction with short [010] lithium diffusion pathways. This result enables a foundation for modifying experimental conditions to design particles with controlled thickness along the [010] direction (the primary lithium ion diffusion path) and therefore enhance the Li-ion battery performance.

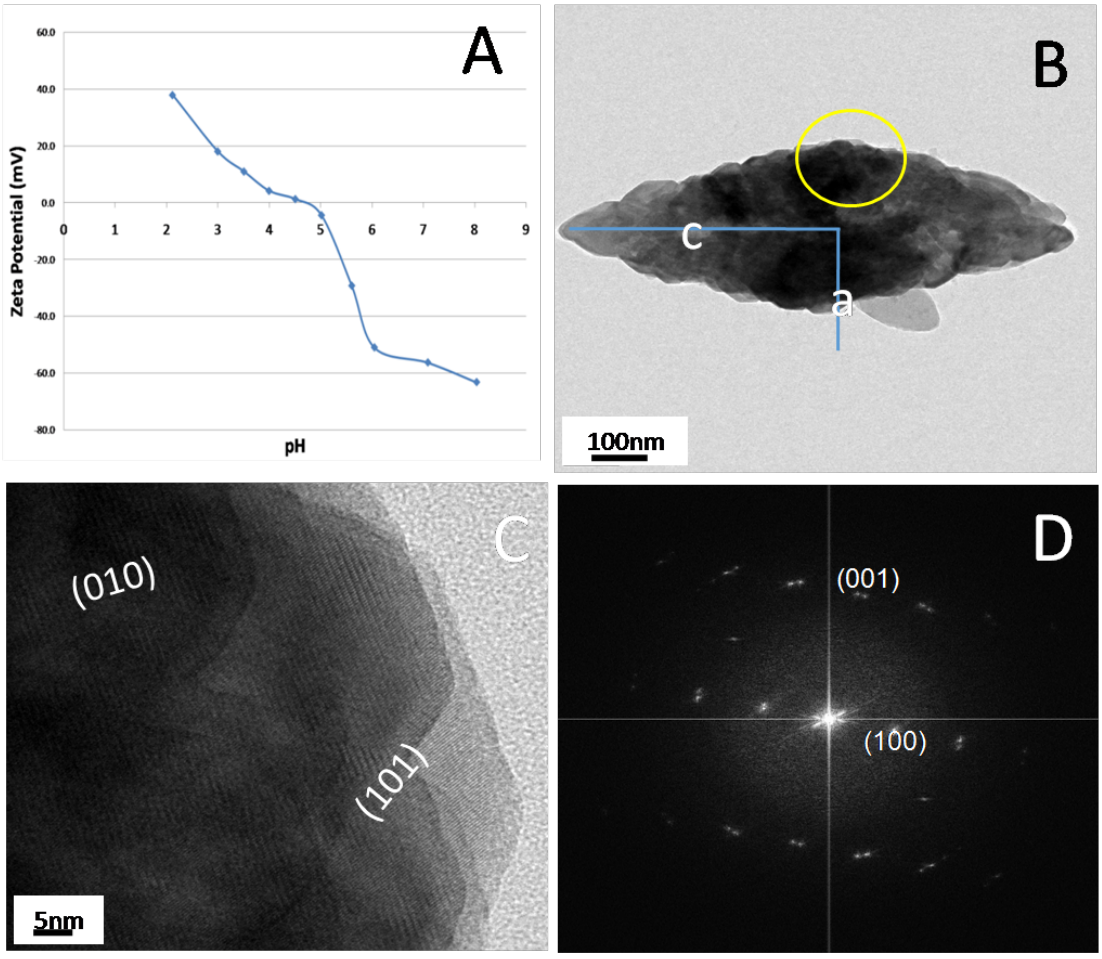

Figure 34. Characterization of $LiFePO_4$ synthesized at 160°C for 10 minutes in a sealed glass reactor. (A) Zeta potential analysis of LFP particles, (B) Bright field TEM showing c and a directions of particles, (C) HRTEM from yellow circle highlighted in (C), and (D) the corresponding FFT.

4.3.1.4. Ostwald ripening of polycrystalline LFP

For longer duration reactions, Teflon-lined autoclaves were used with the same synthesis conditions used in the glass tubes. Here, liners were filled with the same volume (43.5 vol. %) of precursor suspension in order to provide a similar head space and ensure the overall pressure in the reactors were the same in both sealed glass and teflon-lined reactors. After filling and sealing the liners, reactors were heated to 160°C

for different durations (60 minutes to 900 minutes). Subsequent analyses of products from both reactors under the same reaction conditions confirmed the similarity (particle size, crystallinity and shape) of products between these two reactions (Figure 35).

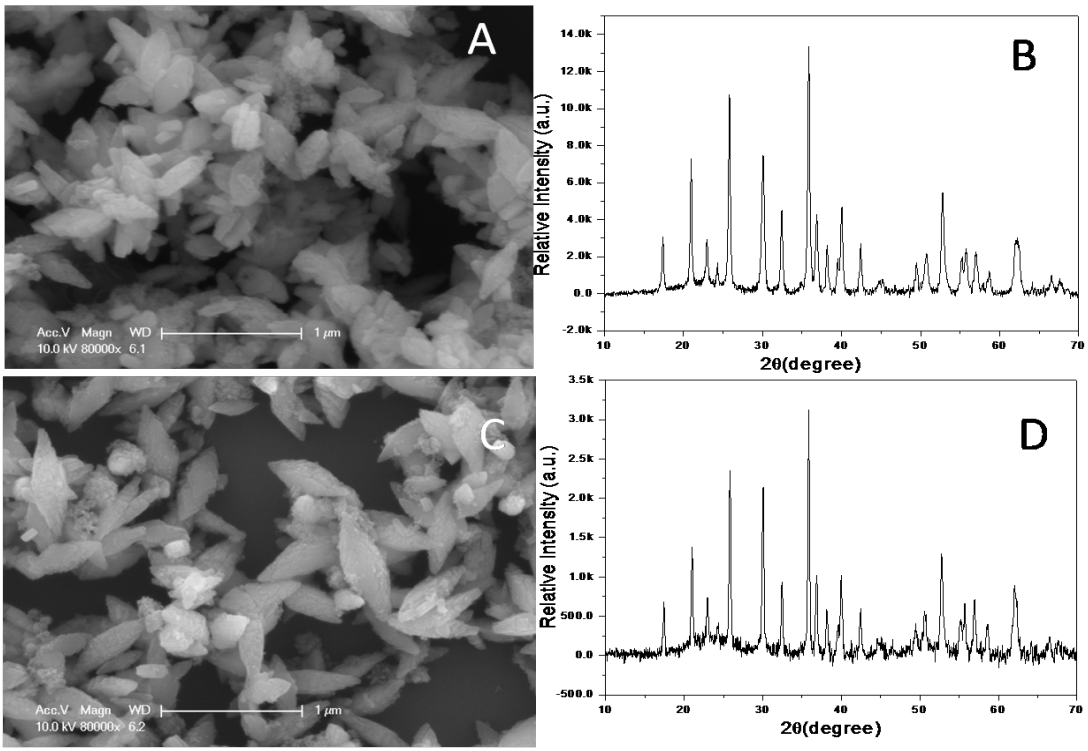

Figure 35. (A) SEM image of LFP particles synthesized in a sealed glass reactor at 160°C for 10 minutes and (B) the corresponding XRD pattern, (C) SEM image of LFP particles synthesized in a Teflon-liner reactor at 160°C for 10 minutes and (D) the corresponding XRD pattern.

SEM micrographs (Figure 36) highlight size and morphology changes of LFP particles at different reaction durations. As the reaction duration increases, the large secondary particles decrease in size with a concurrent increase in crystal size and decrease in number of grain boundaries per particle (Figures 36A–D). For example, the secondary particles are as long as 900 nm (Figure 33) and consist of 39 nm primary crystals (as calculated by the Scherer equation). With increasing reaction duration (i.e.,

60 minutes and 420 minutes in Figures 36B and C, respectively), the crystal size increases to 95 nm and 280 nm, respectively (as measured from SEM and TEM). At the longest reaction duration (900 minutes), significantly smaller particles have formed (ca. 450 nm long) but seem to have no internal grains (i.e., single crystalline).

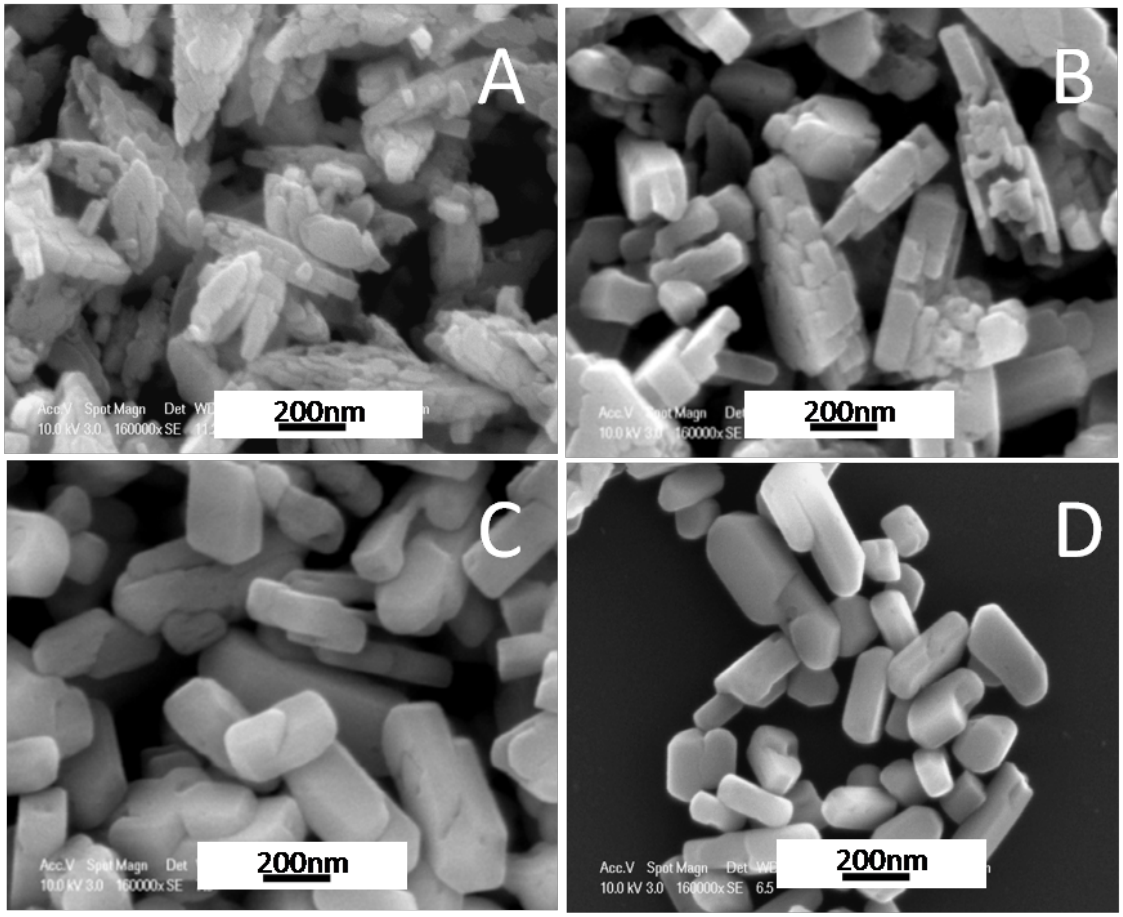

Figure 36. SEM micrographs of LFP products at 160°C with increasing duration. (A) After 10 minutes, LFP formation and assembly into secondary particles is completed. Increasing reaction duration to (B) 60 minutes, (C) 420 minutes, and (D) 900 minutes yields more crystalline LFP.

Measurement of reaction pH versus time (Table 9) indicates a decrease in pH after 5 minutes. This decrease in pH is due to net consumption of OH^- groups (see Equations 11 and 12) as more phosphate anions (PO_4^{3-}) and ferrous cations (Fe^{2+}) are

consumed during the formation of $LiFePO_4$ (Equation 13). The reaction schemes are shown below:

$$PO_4^{3-}{}_{(aq)} + 2H_2O_{(l)} \rightleftharpoons H_2PO4^- + 2OH^- \quad (11)$$

$$Fe^{2+} + 6H_2O_{(l)} \rightleftharpoons Fe(H_2O)_5(OH)^+{}_{(aq)} + H^+ \quad (12)$$

$$Li^+ + PO_4^{3-} + Fe^{2+} \rightleftharpoons LiFePO_4 \quad (13)$$

This decrease in pH increases the solubility of $LiFePO_4$ due to acidity and high temperature conditions.[195] This increased solubility enables a dominating dissolution-crystallization (Ostwald ripening, OR) of these particles, with their subsequent densification and formation of more crystalline particles. The morphology also changes from a diamond-like structure at 10 minutes to polygonal prisms at 900 minutes, providing evidence for the dominating crystal growth mechanism.[196] The drum-like polygonal $LiFePO_4$ crystals are the equilibrium morphology, which has been shown by both experiment and simulation.[186, 194]

4.3.1.5 Development of single crystalline LFP

SEM imaging of the powder products after 900 minutes at 160°C (Figure 37A) reveals a nanorod structure. These nanorods were measured (more than 40 particles) to be 450 ± 60 nm long × 128 ± 24 nm wide × 91 ± 13 nm thick. XRD (Figure 37B) confirms the formation of highly crystalline $LiFePO_4$ (indexed as the orthorhombic olivine-type structure, JCPDS 81-1173) without any detectable impurity phases. Bright field TEM analysis with SAED (Figures 37C and 37D) of one particle revealed its single crystalline nature with elongation along the c direction and a (010) surface plane.

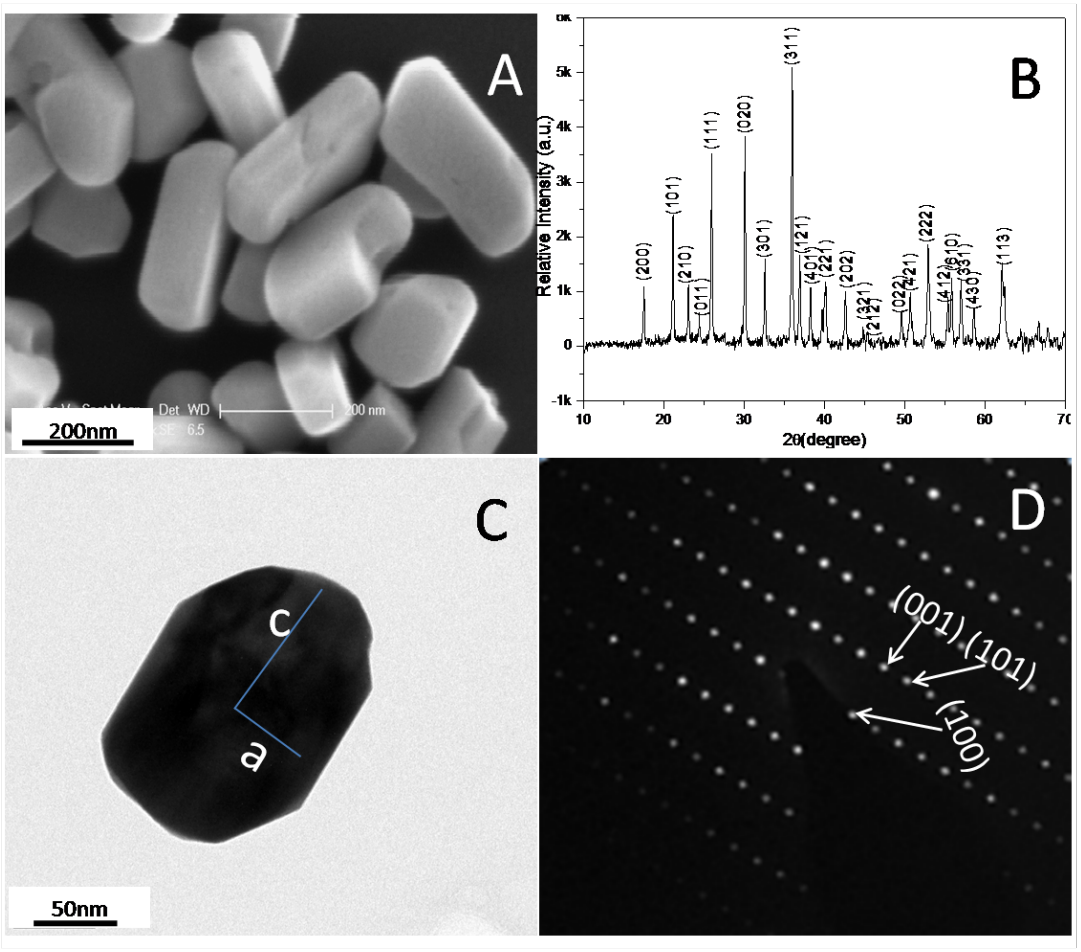

Figure 37. Analysis of single crystalline $LiFePO_4$ synthesized at 160°C for 900 minutes. (A) SEM of powder sample highlighting size and morphological features, (B) XRD pattern confirming pure $LiFePO_4$, (C) Bright field TEM micrograph of a $LiFePO_4$ particle, and (D) the corresponding SAED from (C), confirming its single crystalline nature.

Figure 38 summarizes the entire process of LFP nucleation, primary particle formation and single crystal evolution. Initially, thin (100 nm) platelets of $Fe_3(PO_4)_2 \cdot 8H_2O$ (vivianite, VTE) formed at short reaction times followed by the nucleation of LFP (20 nm particles) on the metastable VTE surfaces. Upon decrease in pH, primary LFP nanocrystals subsequently aggregated into polycrystalline diamond-like particles via an oriented attachment (OA). With increasing reaction time, the solution pH

further decreased, leading to a dissolution-recrystallization process (i.e., Ostwald ripening, OR) of the oriented polycrystalline LFP particles to yield evenly sized, single crystalline $LiFePO_4$.

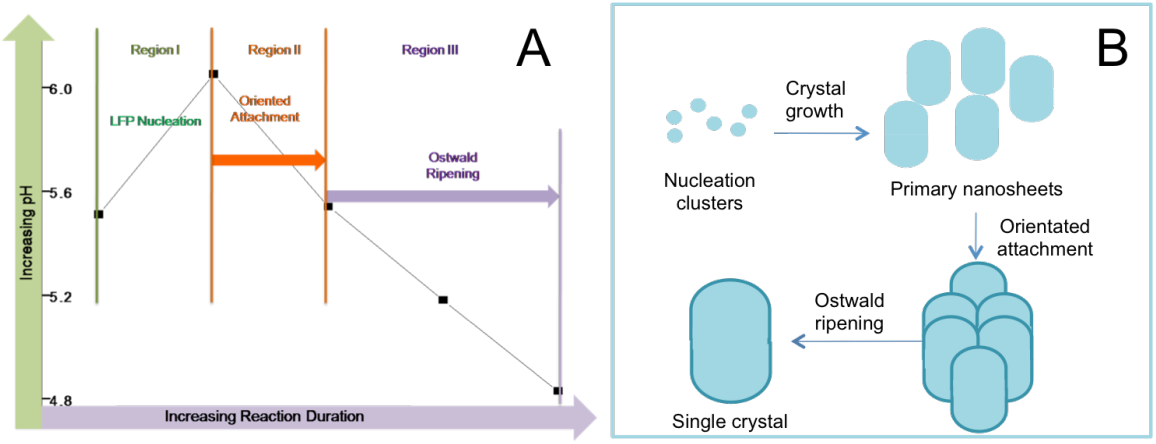

Figure 38. (A) Reaction time vs. solution pH with LFP formation information and (B) schematic of LFP nucleation, primary particles formation and single crystal evolution.

4.3.2 Electrochemical performance

In order to relate LFP structure to performance, electrochemical measurements were conducted for both poly- and single crystalline $LiFePO_4$ materials. Cyclic voltammetry (CV) (Figure 39A), which was performed at a scan rate of 0.2 mV/s at room temperature, display an oxidation peak and reduction peak, corresponding to the charge/discharge reactions of the Fe^{2+}/Fe^{3+} redox couple. The polycrystalline LFP sample (synthesized at 10 minutes) displayed a voltage hysteresis (ca. 0.28 V) and a higher peak current (0.14 A/g), while the single crystalline LFP specimen (synthesized at 900 minutes), had a voltage difference of 0.44 V and a peak current of 0.1 A/g). It is known that smaller voltage differences between the charge and discharge as well as higher peak currents indicate better electrode reaction kinetics, and thus better rate performance.[160, 197]

The results demonstrate that the polycrystalline materials with smaller crystallite sizes (< 40 nm along the [010] direction), yield enhanced kinetics (compared to single crystal particles) during the lithiation and delithiation. Cycling charge/discharge and rate profiles of electrodes with carbon-free (i.e., uncoated $LiFePO_4$) polycrystalline and single crystalline LFP (Figures 39B and 39C) demonstrate similar specific discharge capacities at C/10 (i.e., 109 and 101 mAh/g for polycrystalline or single crystalline LFP, respectively). Our materials show higher discharge capacity compared to the previous reported measurements of carbon free 50 nm LFP particles, which displayed a discharge capacity as low as 60 mAh/g at a C/10 rate.[101] Furthermore, at high rate capacities, polycrystalline specimens with smaller crystallite diameters yielded better electrode reaction kinetics and thus higher rate performance (Figure 39C).

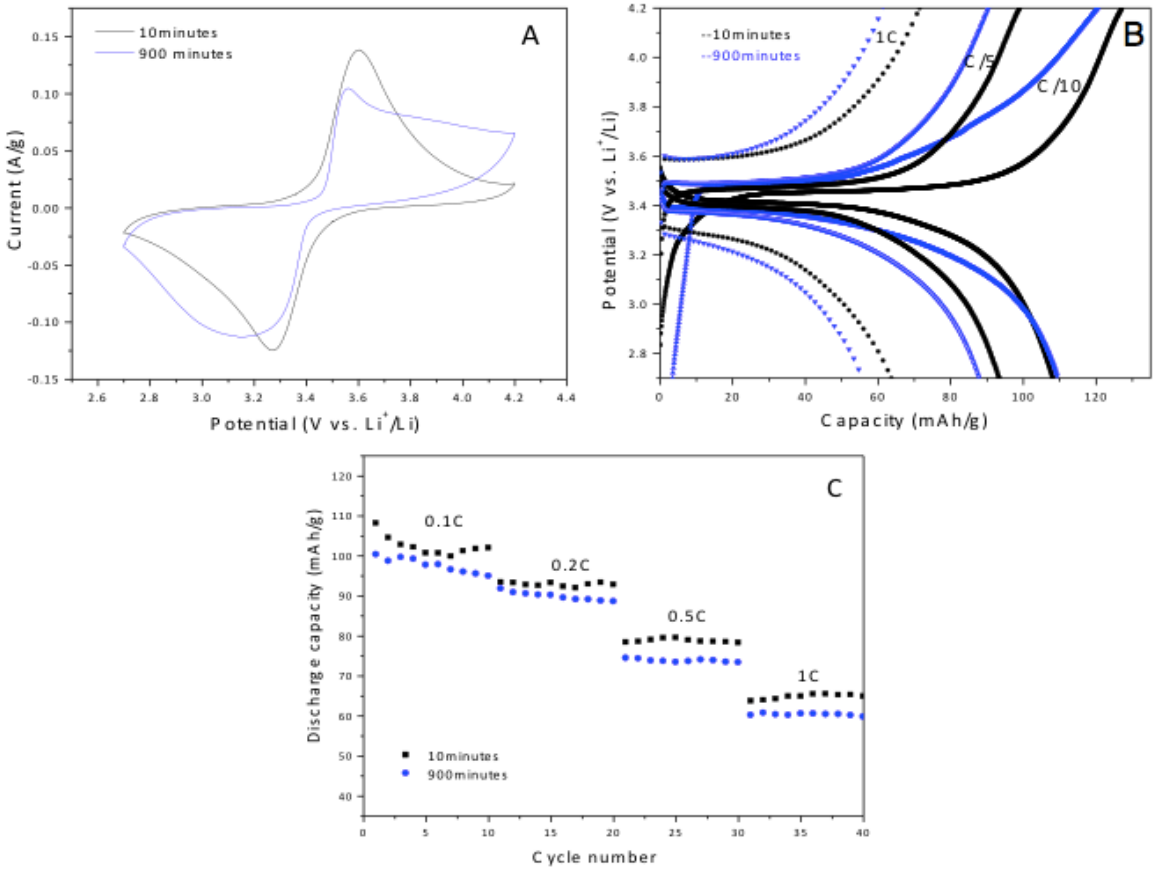

Figure 39. Electrochemical characterization of polycrystalline and single crystalline LFP. (A) CV profiles in the voltage range of 2.7-4.2 V at a scan rate of 0.2 mV/s, (B) Galvanostatic charge/discharge profiles and (C) Cycling performance at various current rates between 2.7 V and 4.2 V (vs. Li^+/Li).

However, neither of these materials have flat voltage plateaus, which is likely due to the absence of an electrically conductive carbon coating. In addition, it is likely that residual moisture, Fe (III) impurities (Figure 40), and less ordered surfaces may be responsible for reduced performance.

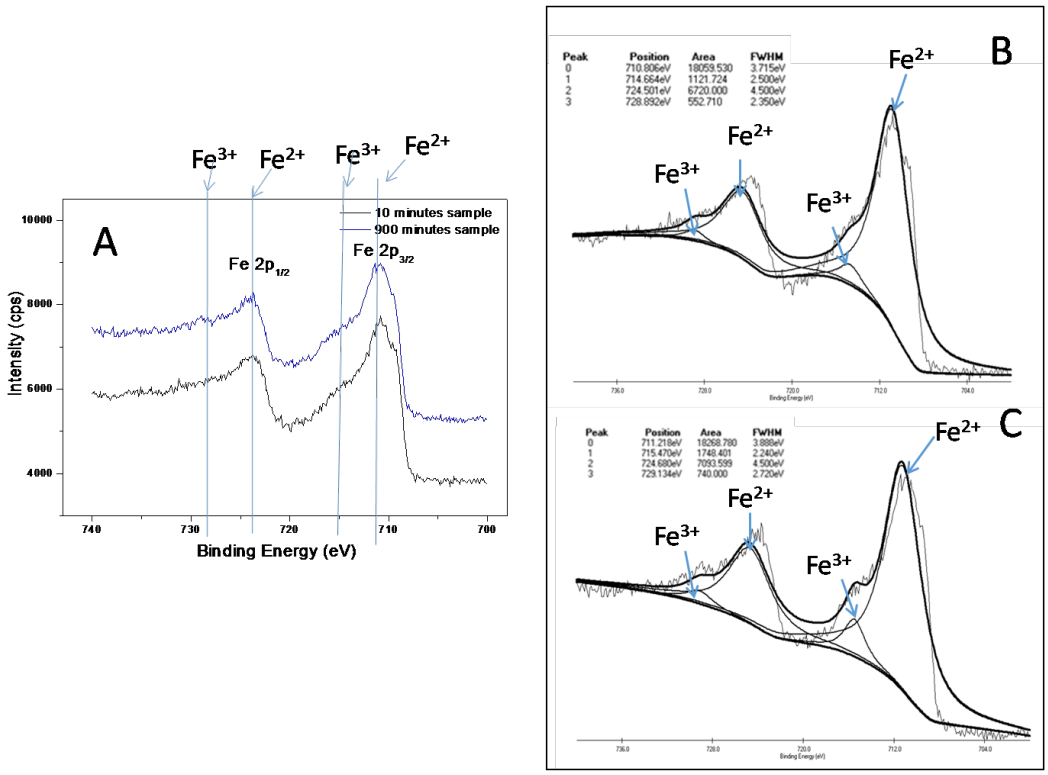

Figure 40. The XPS of Fe 2p for LFP (A) synthesized at 10 and 900 minutes at 160°C, both indicating small concentrations of Fe^{3+} impurities. (B) fitted curve for sample synthesized for 10 minutes and (C) fitted curve for sample synthesized for 900 minutes.

4.4 Conclusions

We have systematically investigated the crystal nucleation and morphological evolution of $LiFePO_4$ in a water-triethylene glycol system. $LiFePO_4$ first formed on the high energy surfaces of $Fe_3(PO_4)_2 \cdot 8H_2O$ platelets. As these primary particles are formed, the reaction pH decreases, which reduces the surface charge on $LiFePO_4$ primary particles. This reduction in surface charge enables the primary particles to approach each other and attach in an oriented manner to form secondary particles. These diamond-like LFP particles are oriented along the (010) plane and elongated in high surface energy direction of [001]. As the reaction proceeds, the pH decreases, promoting the further

crystallization and densification (Ostwald ripening, OR) of LFP due to the increased solubility of LFP. Electrochemical characterization of carbon free LFP materials demonstrate a discharge capacity of more than 100 mAh/g. Polycrystalline particles with smaller primary crystallite diameters afforded higher discharge capacity and better kinetics compared to the single crystalline particles. Based on our understanding of the formation mechanism and the structure-performance relationships in $LiFePO_4$ using an environmental friendly synthetic method, we will continue to produce the $LiFePO_4$ with shorter lithium diffusion paths to improve the battery performance.

4.5 Acknowledgement

This work was sponsored by Winston Chung Global Energy Center.

Chapter 5.

Conformal Carbon Coating of $LiFePO_4$ via Polymer Solution Method

In preparation

Jianxin Zhu, Kevin Yoo, Ibrahim El-halees, Juchen Guo and David Kisailus. Carbon Coating of $LiFePO_4$ via Polymer Solution Method. *In preparation*

ABSTRACT:

We report the synthesis of thin layer carbon coatings on polycrystalline $LiFePO_4$ via a polymer solution method. The annealing temperature was systematically investigated with polymer systems on $LiFePO_4$ based on TGA/DSC results. The crystal structure, crystal size and morphology were monitored and analyzed by X-ray diffraction (XRD) and scanning electron microscopy (SEM). Micro-Raman was used to interrogate the carbon coatings after heat-treatments. Electrochemical performances of coated materials were investigated by cyclic voltammograms (CVs) and galvanostatic charge-discharge analysis. The olivine structured $LiFePO_4$ remained stable up to 600°C, but underwent a rapid reduction reaction from $LiFePO_4$ to Fe_2P above 700°C. The good compatibility between one polymer, polyethylene glycol (PEG) and $LiFePO_4$ enabled the formation of core-shell structure, which was transformed into a thin layer carbon coating on $LiFePO_4$ after annealing. Both PEG and sucrose carbon-based sources yielded high quality of carbon coatings after annealing, as determined by the graphitic/disordered, G/D, ratios of 1.30 and 1.20, respectively. By producing more uniform and coherent coatings on $LiFePO_4$ particles, we were able to produce batteries with a discharge capacity of 80mAh/g at 2C with significantly less carbon (i.e., 0.41 wt.%) with comparable performance to traditionally synthesized carbon-coated $LiFePO_4$ with higher carbon loadings (ca. 2.64 wt.%). This will enable us to produce batteries with higher active material loading and therefore, significantly larger energy densities.

5.1 Introduction

Olivine-structured $LiFePO_4$ was invented and reported by Goodenough et al.[170] in 1996 as an excellent candidate for the next-generation large-scale lithium ion battery used for hybrid electric vehicles (HEVs) or electric vehicles (EVs) because of its low cost, nontoxic and environmentally benign nature, thermal and chemical stability as well as good cyclability. One drawback of using $LiFePO_4$ is its low rate capacity, which is due to the poor electronic conductivity and low lithium ion diffusivity. These disadvantages inhibit its commercial utilization. In order to overcome this inherent deficiency of $LiFePO_4$, the particle sizes of $LiFePO_4$ are being reduced to the nanoscale and the conductivity is modified (e.g., by additives such as carbon, silver, etc., or via cationic/anionic doping). Among all of the different surface modifications, carbon coated $LiFePO_4$ has been the most intensively studied. [95, 173, 198-201] Previous research on carbon coatings have proven successful to increase the performance. However, it has been pointed out that even small amounts of carbon additive will result in the unrealistically low practical energy density. As reported by Chen et al.,[95] the tap density would decrease from 1.9 to 1.05g/cm^3 with only 2.5% carbon added, thus the volumetric density for the industrial applications will be reduced by more than 40%. Therefore, low (less than 1%) carbon additives are desired for these practical applications. At the same time, the structure of carbon is another factor that can affect performance in batteries. The carbon structure with higher sp^2- coordination ratio to disordered carbon or sp^3-coordinated carbonaceous is of great benefit to electronic conductivity.[200] Thus, it is urgent to produce high quality carbon coatings with minimal loading. Figure 41 is the schematic of

the conventionally used (Figure 41B) and newly proposed carbon coating via polymer solution method (Figure 41C).

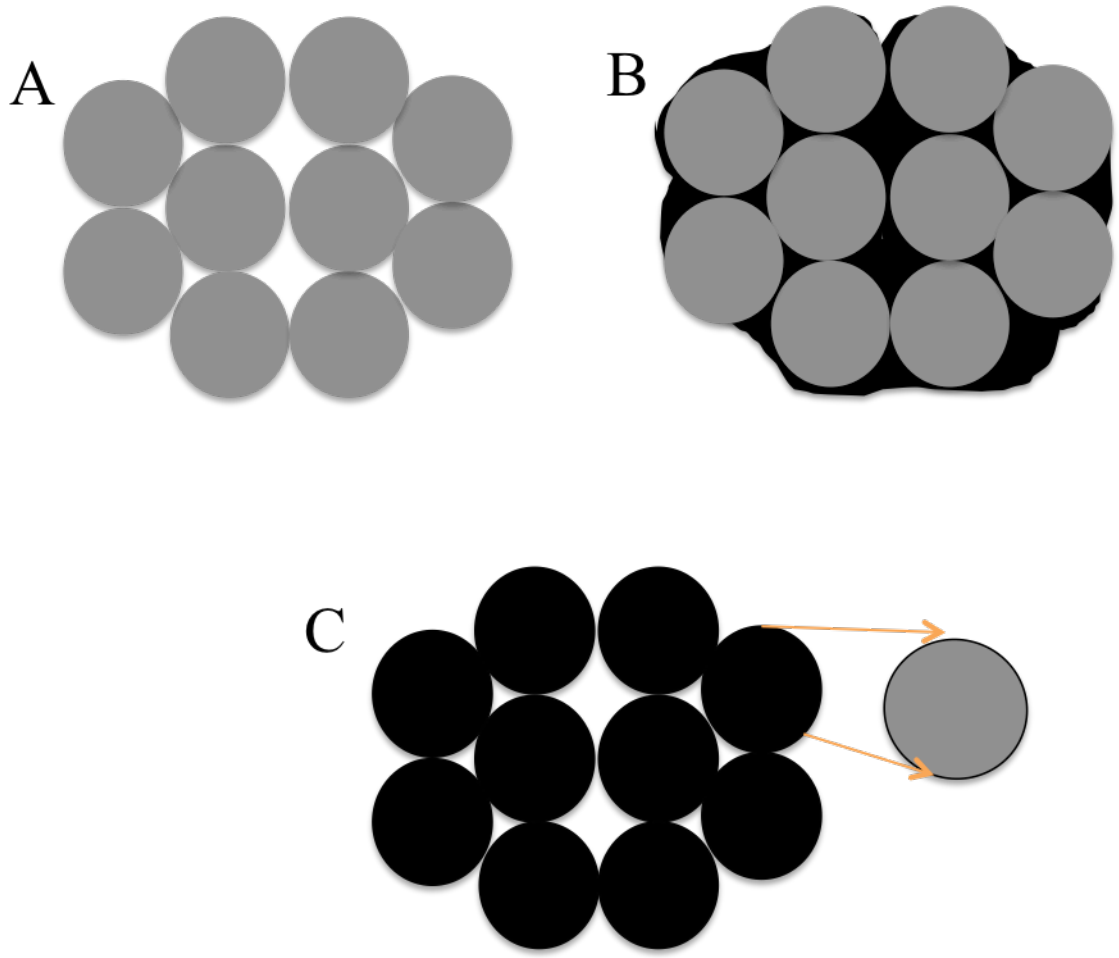

Figure 41. Schematic of carbon coating on $LiFePO_4$ (A) pure $LiFePO_4$ without any carbon coating, (B) carbon coated $LiFePO_4$ with conventionally used mechanical method, and (C) carbon coated $LiFePO_4$ with precisely controlled method.

Here, we utilized a polyethylene glycol polymer as the carbon source to coat the polycrystalline $LiFePO_4$ we previously described (Chapter 4). In recent years, polyethylene glycol aqueous solutions have been widely used in many different kinds of

reaction systems.[202] Their low-toxicity, low volatility, and biodegradability represent important environmentally benign characteristics, which are particularly attractive when combined with their relatively low cost as a bulk commodity chemical. Here we used PEG as a surfactant in the $LiFePO_4$ aqueous suspensions to form core-shell structures, and subsequently transforming this to a thin layer coating with very low (less than 0.5%) carbon content after annealing.

5.2 Experimental Section

5.2.1 Annealing of $LiFePO_4$ powders

The synthesized polycrystalline $LiFePO_4$ powders using hydro-solvothermal methods (described in section 4.2.1) were ground with a mortar and pestle for heat treatment preparation. The ground powder was placed in an alumina boat and annealed in a sealed tube furnace in 95% N_2/5% H_2 forming gas at temperatures from 200°C – 700°C for 3hours. The forming gas also helped in the reduction of Fe^{3+} to Fe^{2+} presented in the pristine $LiFePO_4$ (as discussed in section 4.3.2, Figure 40). The samples were taken out of the tube furnace after cooling to room temperature for subsequent characterization and electrochemical analysis.

5.2.2 Synthesis of carbon-coated $LiFePO_4$

Sample A represents the $LiFePO_4$ coated with carbon from the PEG source via the polymer solution method. Briefly, 10% PEG solution was prepared by dissolving a specific amount of polymer in degassed Milli-Q water until a clear solution is formed. At the same time, a 1% $LiFePO_4$ suspension was made by adding a specific amount of

$LiFePO_4$ powder (weight ratio of $LiFePO_4$ to polymer is 1:10) to degassed Milli-Q water and sonicating for 3 minutes. The $LiFePO_4$ suspension was then added to the prepared polymer solution (drop-by-drop), followed by magnetic stirring (600 rpm) at room temperature for 1 hour in order to completely mix the polymer and $LiFePO_4$ particles. Finally, the suspension was centrifuged at 8000 rpm for 5 minutes and dried in vacuum at 70°C for 5 hours. The dried samples were then placed in an alumina boat and annealed in a sealed tube furnace in 95% N_2/5% H_2 forming gas at 600^{o}C for 3 hours.

Sample B represents the $LiFePO_4$ coated with carbon from a sucrose source by a solid-state method. As synthesized $LiFePO_4$ powders and sucrose (10 wt.%) were weighed and mixed in a glass jar containing alumina beads (weight ratio of alumina beads: LFP/sucrose powder was 20:1). This mixture was mechanically ground for 30 hours using a rolling machine. After grinding, the mixture was annealed in a tube furnace in 95% N_2/5% H_2 at 600°C for 3hours (i.e., the same procedure as sample A).

Sample C is a control sample, not containing carbon. It is polycrystalline $LiFePO_4$ annealed at 600^{o}C in 95% N_2/5% H_2 for 3 hours as the control sample.

5.2.3 Material characterization

Phase identification was determined by X-ray diffraction analysis (XRD, Philips X'Pert) using Cu Kα radiation. Using the resulting XRD diffraction patterns, crystallite diameters were calculated based on the Scherer formula. Particle sizes and morphologies were observed using a scanning electron microscope (SEM, FEI XL30) at 10-20 kV accelerating voltage. A transmission electron microscope (TEM, FEI CM300), operated at 300 kV, was used to identify crystallite size, morphology and phase. Thermal and mass

analyses were performed using a thermal gravimetric analyzer/differential scanning calorimeter (TGA/DSC, TA Instruments Q600), annealed from 25°C - 700°C (heating rate of 10°C/min) with a 3 hour hold at 700°C in 95% N_2 / 5% H_2. This was done to investigate $LiFePO_4$ thermal behavior during annealing. Raman spectroscopy measurements were carried out at room temperature in an ambient atmosphere using a 532 nm laser as the excitation source with at 1mW power. The total carbon content of coated $LiFePO_4$ samples was analyzed using a Perkin Elmer 2400 II CHN analysis from Tucson Laboratory of ALS (Australian Laboratory Services) environmental center.

5.2.4 Electrochemical performance

As-prepared $LiFePO_4$ powders (either sample A, B or C), conductive carbon black (Super P), and polyvinylidene fluoride (PVDF, 78:14:8wt.%) were mixed in N-methylpyrrolidone (NMP) to produce a slurry. This viscous slurry was subsequently coated on an aluminum foil current collector. The coated film was dried in the vacuum oven at 100°C for 12 hours. Coin cells (R2032 type) were assembled in an argon-filled glove box, consisting of the prepared positive electrode, lithium metal foil as the negative electrode, Celgard polymer as a separator and 1.0 M $LiPF_6$ in ethylene carbonate (EC)–diethyl carbonate (DEC) (50:50 vol.%) as the electrolyte solution. The loading of the active material was 1.5-2 mg/cm^2. The cyclic performance and rate capability of $LiFePO_4$ batteries were tested using an Arbin battery test system (Arbin Instruments, Model BT2043). Cyclic voltammograms were run on a VMP3 multichannel electrochemical station.

5.3 Results and Discussion

5.3.1 Annealing parameters investigation

5.3.1.1 Pristine $LiFePO_4$ annealing study

In order to obtain an optimum annealing temperature for the carbon coating process, the thermal behavior of synthesized polycrystalline $LiFePO_4$ was investigated by TGA/DSC. Figure 42 shows the TGA/DSC curves of pristine $LiFePO_4$ heated from 25°C to 700°C at 20cc/min flow rate in 95% N_2 / 5% H_2 (with a 3 hours hold at 700°C). The first endothermic peak at 110°C, accompanied by a ~2% weight loss, is ascribed to water desorption. The other three consecutive endothermic peaks at 398°C, 505°C, and 570°C occurring without obvious mass change are likely due to a crystallization process. Interestingly, the immediate mass loss (5%) from 600°C to 700°C was observed, which indicated a reduction reaction of $LiFePO_4$ in 95% N_2 / 5% H_2.[203]

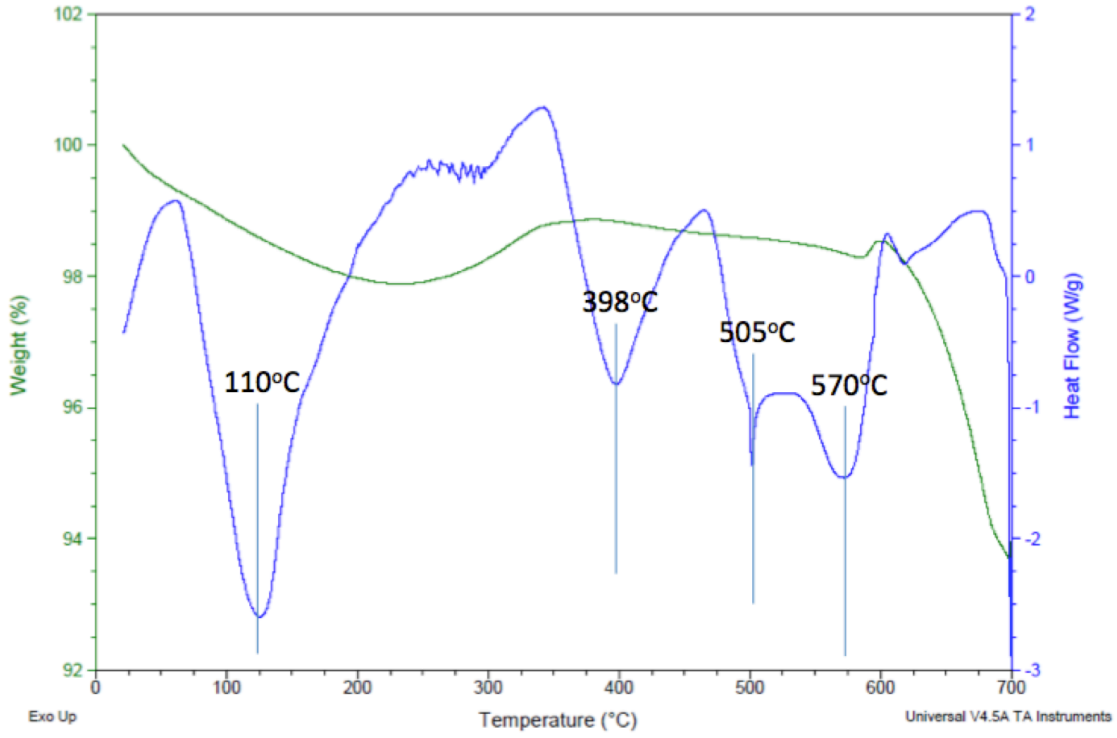

Figure 42. TGA/DSC of pristine $LiFePO_4$ from 25°C to 700°C at 20 cc/min flow rate in 95% N_2 / 5% H_2 with a 3 hour hold at 700°C.

After performing the TGA/DSC, we systematically investigated the resulting structures by annealing at different temperatures (i.e., from 200°C - 700°C). The XRD diffraction patterns in Figure 43 show the pristine $LiFePO_4$ annealed from 200°C to 700°C for 3 hours in 95% N_2 / 5% H_2 at 20 cc/min at a 10°C/min ramp rate. Between 200°C and 600°C, the olivine $LiFePO_4$ phase was stable but peak narrowing occurred between 500°C - 600°C. It is clear that the crystal size increased with increasing heat treatment (from 200°C to 700°C). The increase in crystalline size above 400°C is explained by the endothermic peaks at 398°C, 505°C and 570°C from the DSC curve in Figure 42. XRD for the sample annealed at 700°C for 3 hours identified the Fe_2P phase

(instead of $LiFePO_4$), reflecting the reduction of $LiFePO_4$ under N_2/H_2 at higher temperatures. Weight loss above 600°C from TGA confirmed this transformation.

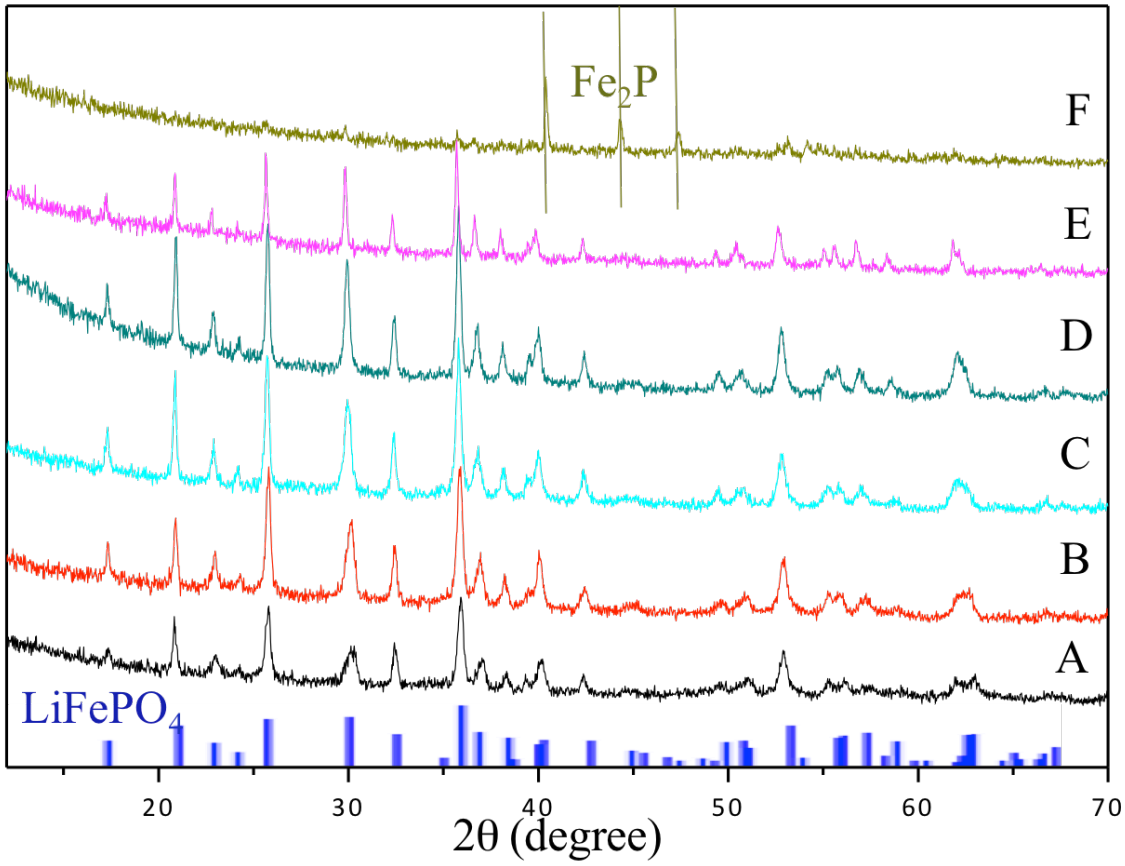

Figure 43. XRD diffraction patterns for pristine $LiFePO_4$ annealed for 3 hours in 95% N_2 / 5% H_2 at: (A) 200°C, (B) 300°C, (C) 400°C, (D) 500°C, (E) 600°C, and (F) 700°C.

Figure 44 depicts the morphological changes for samples heat-treated at various temperatures. By 400°C, smaller nanoparticles were not observed and the surfaces of larger particles became smoother, indicating grain boundary diffusion. By 500°C, particle sizes decreased with increasing crystallite size and the particles appeared more rounded. By 600°C, the diamond like morphology of particles was no longer evident and some faceting was evident. By 700°C, a clear change in particle size and morphology had

occurred. XRD of this sample (Figure 43F) confirmed the Fe_2P phase, explaining this significant change.

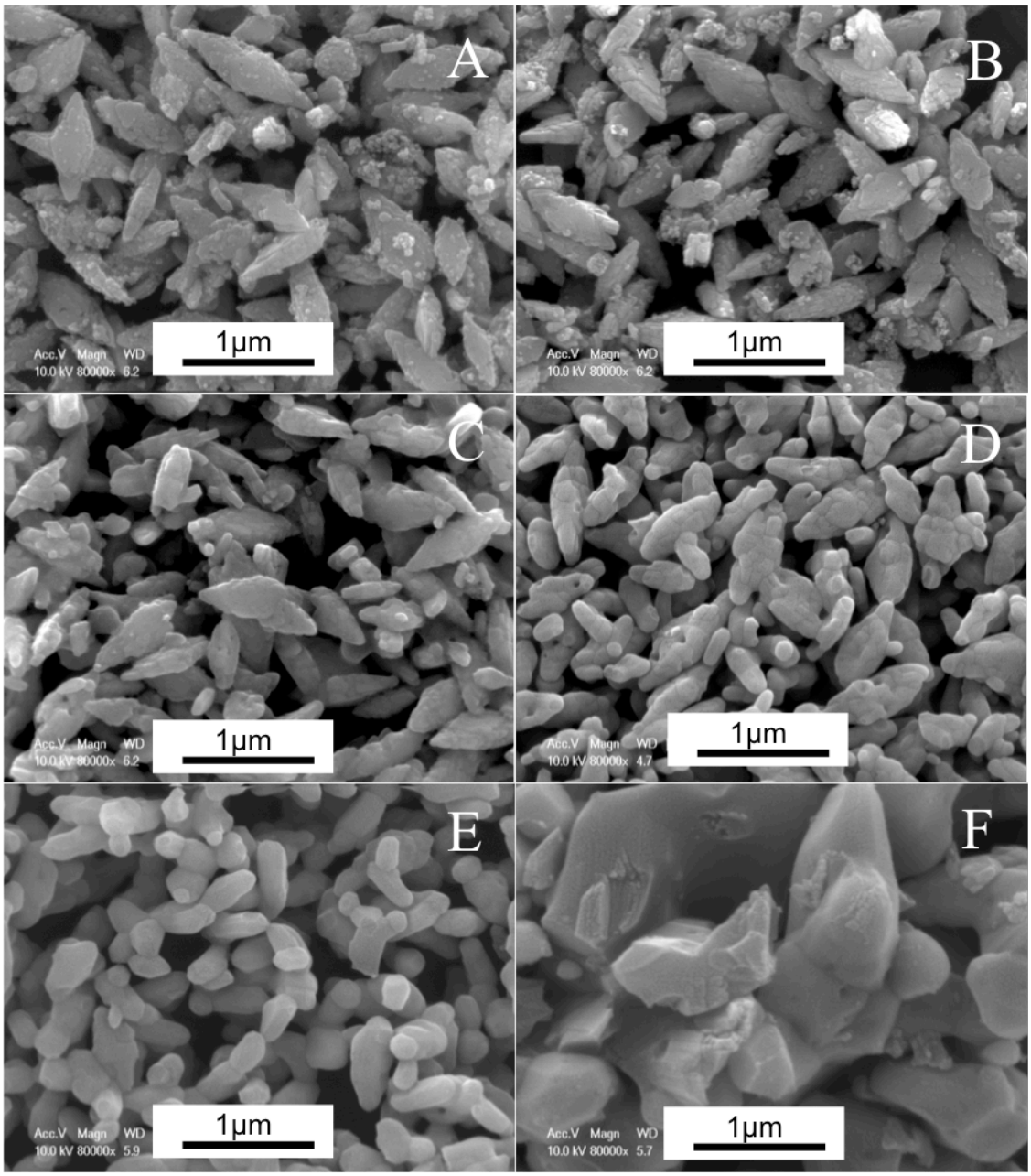

Figure 44. SEM micrographs of pristine $LiFePO_4$ annealed in 95% N_2 / 5% H_2 for 3 hours at: (A) 200°C, (B) 300°C, (C) 400°C, (D) 500°C, (E) 600°C, and (F) 700°C.

5.3.1.2 PEG and sucrose annealing study

The thermal analysis of polyethylene glycol in 95% N_2 / 5% H_2 from 25°C to 700°C was investigated using TGA/DSC (Figure 45A). The first two endothermic peaks before 200°C accompanying with 5% weight loss is due to the water desorption in the polymer. PEG started to decompose at ~225°C and finished at 450°C with only a small amount of carbon remaining (0.5 wt.%).[204] A similar endothermic peak before 200°C also was present for sucrose (Figure 45B), but required longer times for carbonization. To analyze the resulting carbon structure, we conducted micro-Raman analyses for residues after various heat treatments for both PEG and sucrose.

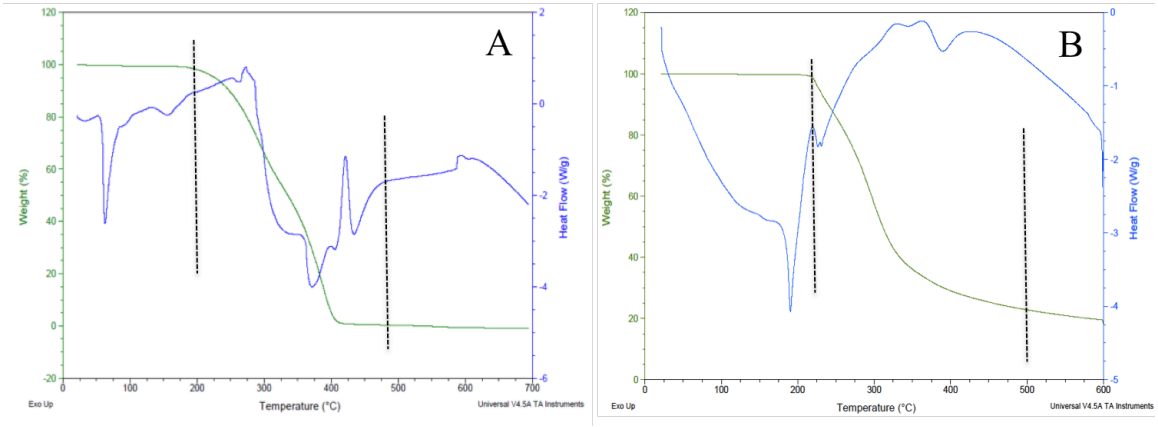

Figure 45. TGA/DSC curves for PEG and sucrose heated in 95% N_2 / 5% H_2 flowing at 20 cc/min. (A) PEG from 25°C to 700°C and held for 3 hours duration and (B) sucrose from room temperature to 600°C and held for 3 hours duration.

Raman has been widely used to detect and differentiate graphitic and disordered carbon. Graphitized carbon is known to have a better electronic conductivity compared to disordered carbon.[205-212] Based on our observations from TGA/DSC (Figure 45), we annealed PEG at four temperatures (i.e. 400, 500, 600 and 700°C) to investigate the resulting ordering in the carbon structures. The PEG was heat treated in 95% N_2 / 5% H_2

at 20 cc/min with a 10°C/min ramp rate from 25°C to the desired temperature, followed by a 3 hour hold time. As seen in Figure 46, all of the Raman spectra consist of two intense peaks at 1355 cm^{-1} and 1584 cm^{-1}, corresponding to the disordered (D) and graphitic (G) bands of carbon, respectively. The third broad peak at 2710 cm^{-1} is attributed to the 2D band (D peak overtone), which originates from a process where momentum conservation is satisfied by two phonons with opposite wave vectors.[213] It's clear that for all samples, the graphitic peak at 1584cm^{-1} showed higher intensities compared to the disordered carbon peak at 1355cm^{-1}, indicating a good expected electronic conductivity.[209, 211] Upon careful examination of these peaks, there is a trend in the ratio of G/D (Table 10). The G/D ratio increased from 400°C to 600°C, then decreased at 700°C. The decreased graphitic peak intensity ratio is due to the disruption of layered carbon structure at high temperatures in the forming gas (the exothermic peak around 600°C).[214]

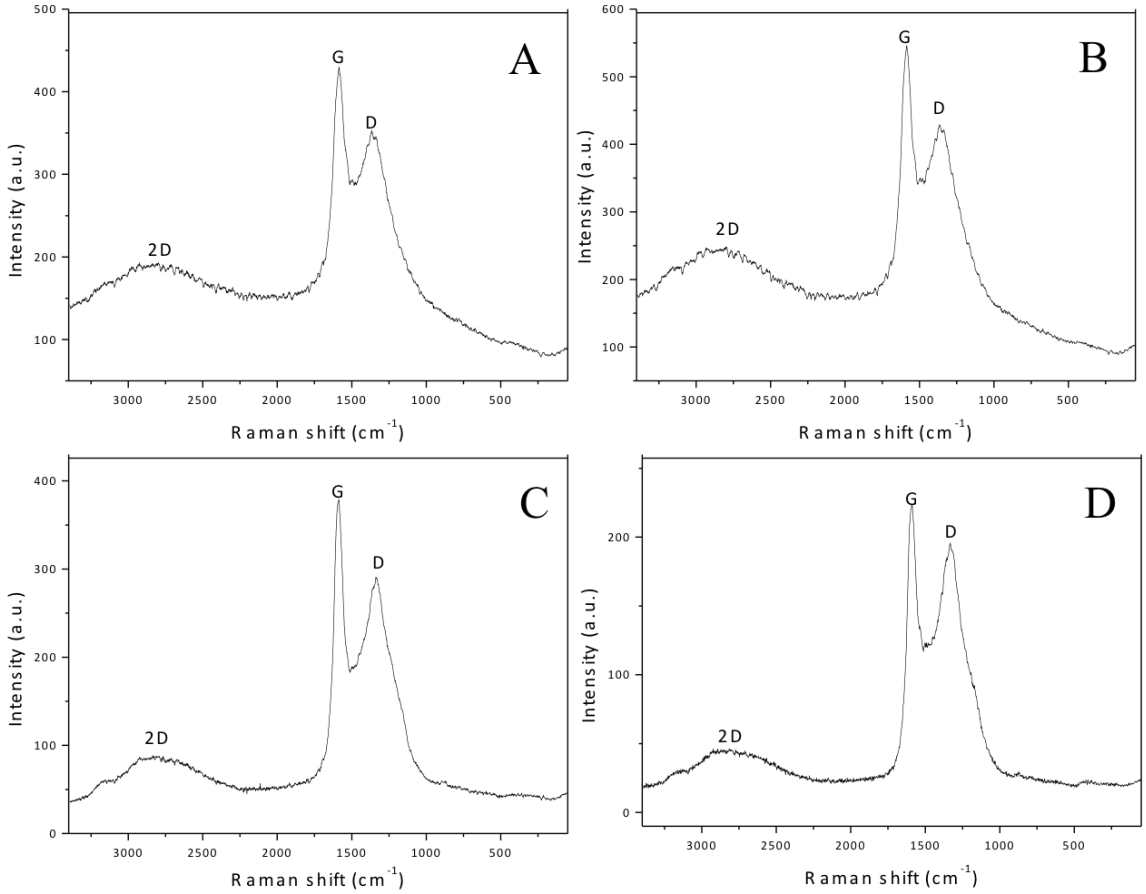

Figure 46. Raman spectroscopy of PEG annealed in 95% N_2 / 5% H_2 at 20cc/min for 3 hours duration at: (A) 400°C, (B) 500°C, (C) 600°C, and (D) 700°C.

Table 10. Structural Carbon Data from Annealed PEG and Sucrose Sources

Carbon Source	Annealing Temperature (°C)	Intensity ratio of G/D
PEG	400	1.30
PEG	500	1.36
PEG	600	1.36
PEG	700	1.15
Sucrose	500	1.20
Sucrose	600	1.43

Based on our observations of an increasing ratio of G/D from 500°C to 600°C, we selected our annealing temperature for PEG or sucrose coated $LiFePO_4$ to be 600°C.

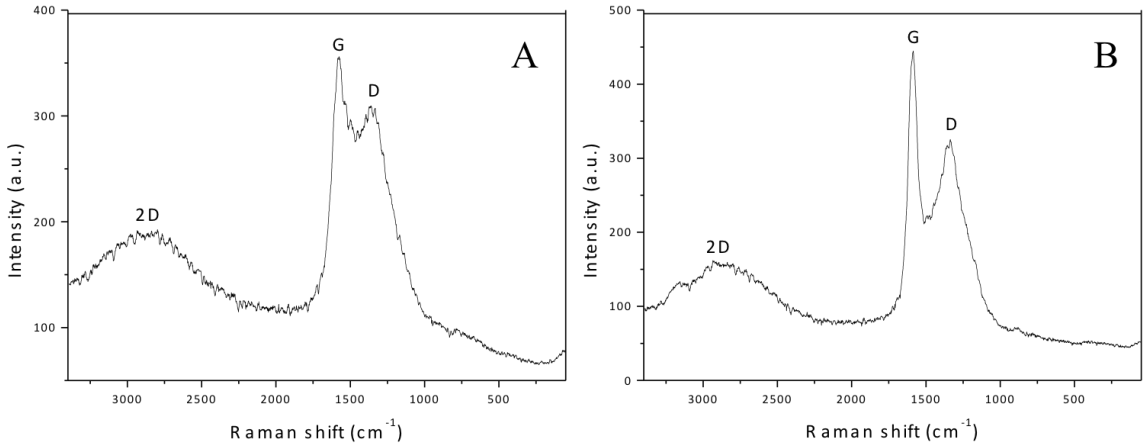

Figure 47. Raman spectroscopy of sucrose annealed under 95% N_2 / 5% H_2 at 20 cc/min for 3 hours duration at: (A) 500°C, (B) 600°C.

5.3.2 Carbon-coated $LiFePO_4$ from PEG (sample A)

5.3.2.1 Mixture of PEG solution and $LiFePO_4$ suspension

After mixing the as-synthesized polycrystalline $LiFePO_4$ suspension with polymer solution (as described in the experimental section 5.2.2), the mixture morphology was studied via SEM. Figure 48 reveals that the surfaces of $LiFePO_4$ were surrounded by a thin film (likely PEG). Upon heating, an evenly distributed carbon layer would likely be formed on the surfaces. The good compatibility between PEG and $LiFePO_4$ can be explained by their surface charges. The solution pH of 1 wt.% $LiFePO_4$ in water is ~ 10.5 (caused by the reaction of Li with water[215]). Thus, the surfaces of $LiFePO_4$ will be negatively charged (see Zeta potential curve, Figure 34A). Aqueous PEG solutions (10wt%) have a pH = 7.3. Based on the pKa value of PEG (14~16), we expect the polymers to be positively charged and can thus electrostatically bind with the $LiFePO_4$ surface.

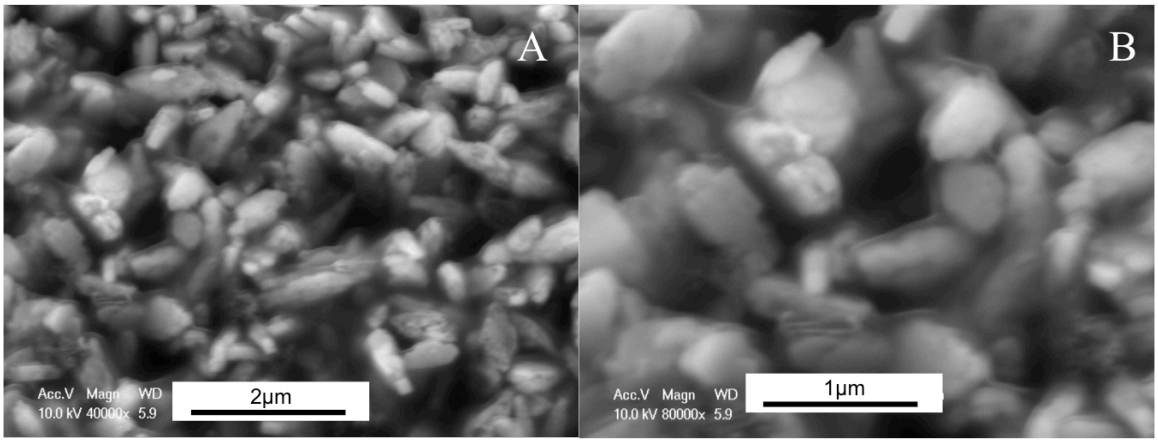

Figure 48. SEM micrographs for solution-coated PEG on $LiFePO_4$ after magnetically stirring for 1 hour.

5.3.2.2 Carbon-coated LFP from PEG

Based on our previous investigations (section 5.3.1), we selected 600°C as the annealing temperature for both PEG and sucrose coated $LiFePO_4$ systems. The SEM micrographs in Figure 49 displays a similar morphology as the pristine $LiFePO_4$ (as synthesized, Figure 33A) but shows a larger number of smaller nanoparticles. We believe this is due to break up of secondary particles under the magnetic stirring. XRD in Figure 50 shows pure $LiFePO_4$ phase without any detectable impurities (such as FeP or Fe_2P) and all of the peaks are indexed as an orthorhombic olivine-type structure (JCPDS# 81-1173).[216] The crystallite size of the LFP coated with polymer was calculated to be 52 nm using the Scherer equation (Table 11).

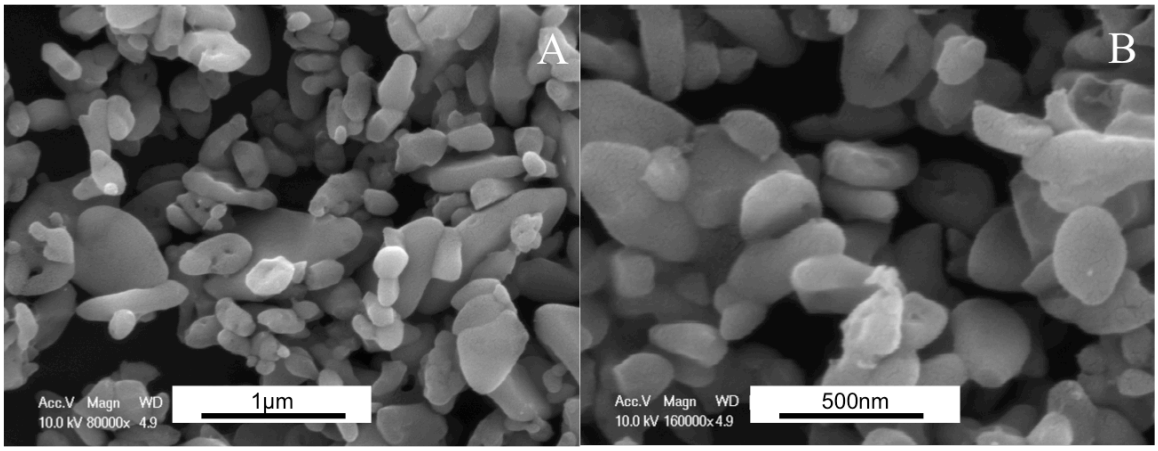

Figure 49. SEM micrographs for carbon-coated $LiFePO_4$ (from PEG) after annealing at 600°C for 3 hours in 95% N_2 /5% H_2 at 20 cc/min.

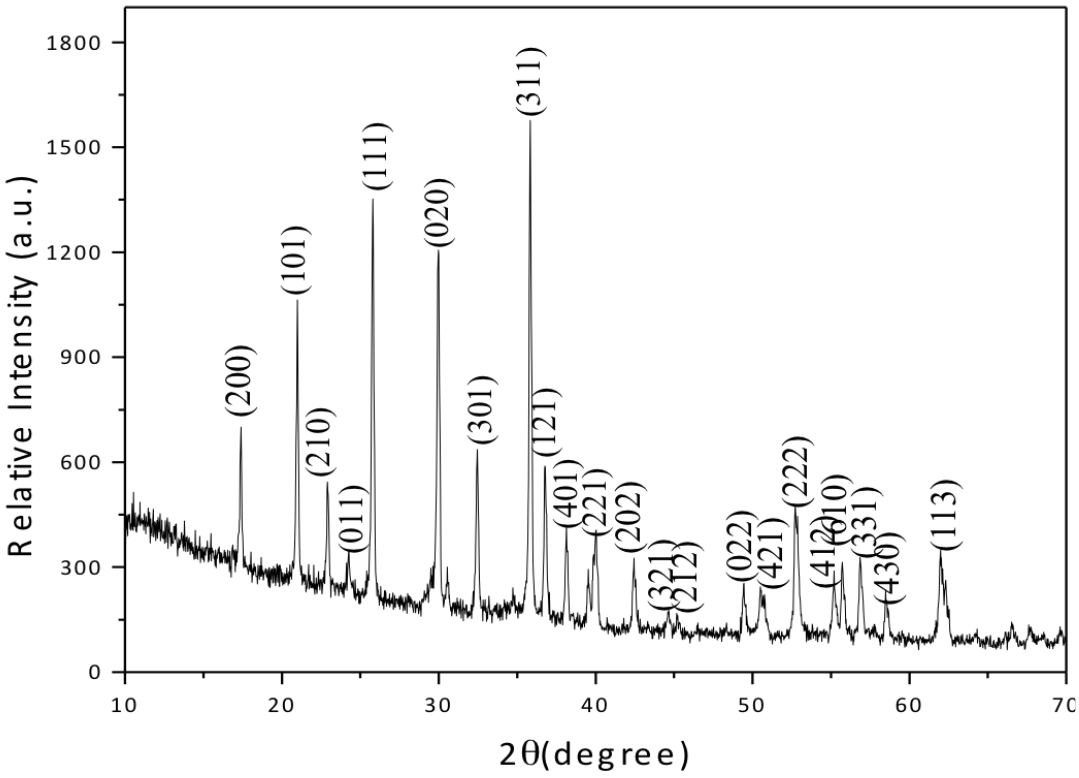

Figure 50. XRD diffraction pattern for carbon-coated $LiFePO_4$ (from PEG) after annealing at 600°C for 3 hours in 95% N_2 / 5% H_2 at 20 cc/min.

The Raman spectra in Figure 51 shows the resulting carbon structure for PEG-coated $LiFePO_4$ after annealing (under the same conditions as pure PEG and sucrose in

5.3.1.2, Figures 46 and 47). The ratio G/D peaks is the same (1.30) as pure PEG heat-treated under the same conditions and is comparable or even better than previous reports.[200, 217, 218] The smaller peak at 946cm^{-1} is ascribed to the symmetric vibration of the PO_4 groups in $LiFePO_4$.[217] Based on the high ratio of graphitic carbon, we suspect these coated $LiFePO_4$ particles to display good electronic conductivity, with better high rate discharge capacities in cells.

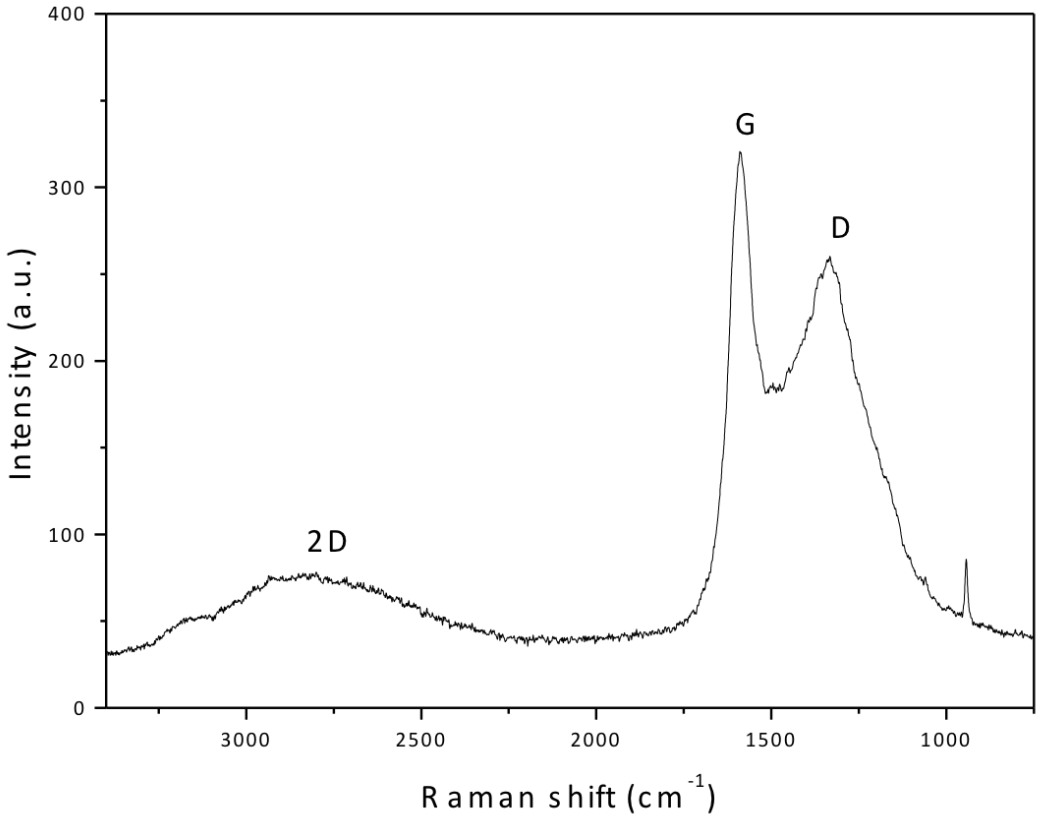

Figure 51. Raman spectroscopy of carbon-coated $LiFePO_4$ (from PEG) annealed at 600°C for 3 hours in 95% N_2 / 5% H_2 at 20 cc/min.

5.3.3 Carbon-coated $LiFePO_4$ from sucrose (sample B)

Sucrose, a commonly used source of carbon in battery materials, was also selected to investigate its effect as a carbon coating on our polycrystalline $LiFePO_4$. The

procedure (illustrated in the experimental section 5.2.2) uses a solid-state method to mechanically mix sucrose and $LiFePO_4$. After the same heat-treatment process as sample A, SEM was used to observe morphological changes and XRD to confirm the phase and crystallite sizes. Figure 52 shows that particles tend to be more aggregated compared to the PEG added $LiFePO_4$, which is likely due to heterogeneities from a solid-state mixing process (versus a solution method).

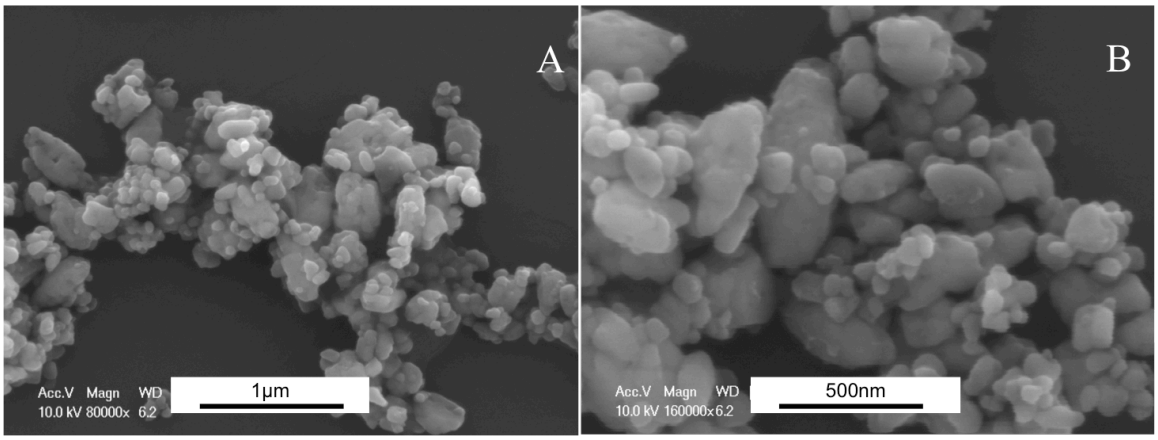

Figure 52. SEM micrographs for sucrose added $LiFePO_4$ mixture after annealing at 600°C for 3 hours in 95% N_2 / 5% H_2 at 20 cc/min.

The XRD pattern in Figure 53 confirmed pure $LiFePO_4$ phase without any detectable impurities. The crystal size calculated from the Scherer equation is 41nm (Table 11). It has a smaller crystal size compared to the PEG added $LiFePO_4$ (sample A). The difference in crystallite size in PEG-coated LFP and sucrose-coated LFP is likely due to the extra energy provided by the exothermic decomposition of PEG. Figures 45A and B show the TGA/DSC data for PEG and sucrose, respectively. It is clear that there is an exothermic peak at 425°C in PEG (and no exothermic peak observed in the decomposition of sucrose) which likely added energy for the crystal growth on $LiFePO_4$.

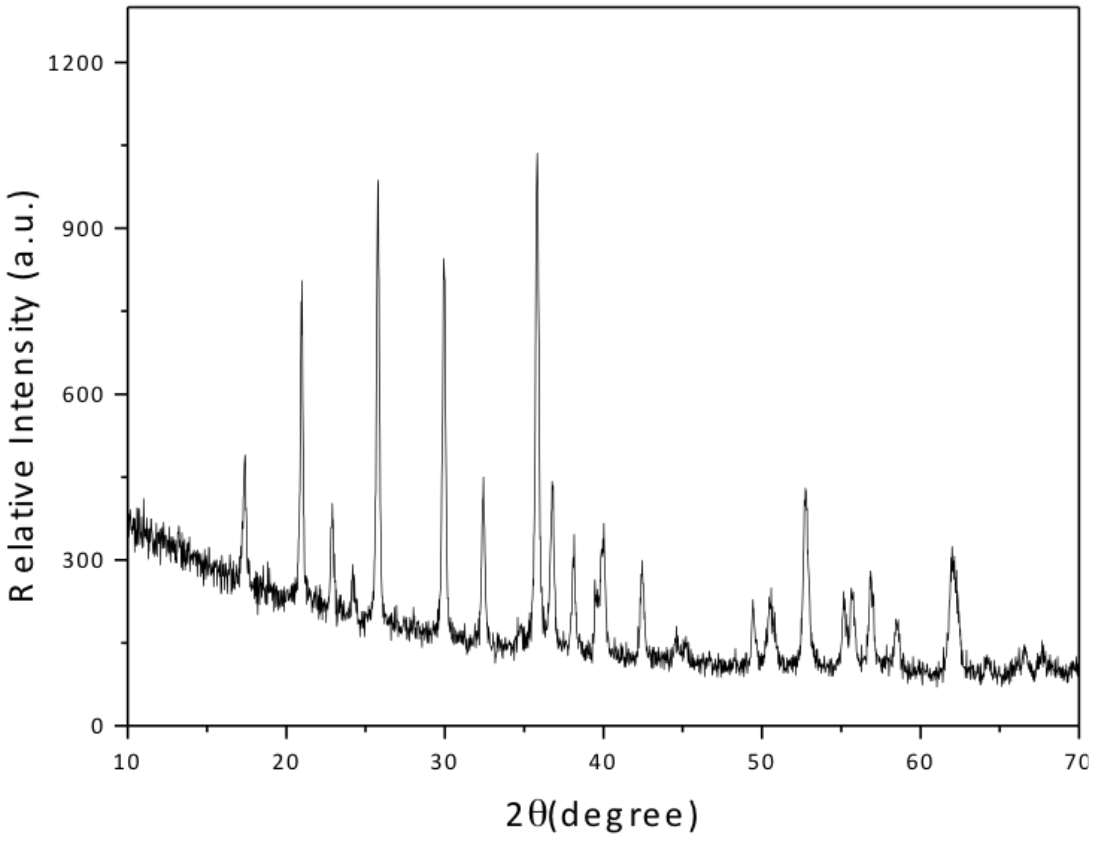

Figure 53. XRD diffraction pattern for sucrose added $LiFePO_4$ after annealing at 600°C for 3 hours in 95% N_2 /5% H_2 at 20 cc/min.

Raman spectroscopy (Figure 54) displays the carbon structure for sucrose added $LiFePO_4$ after annealing under the same condition of PEG added $LiFePO_4$ (sample A). The spectroscopy is very similar to sample A with a slightly lower G/D ratio of 1.20. The carbon analysis for samples A and B are listed in Table 11. The carbon content in sample A (PEG added $LiFePO_4$) is only 0.41wt% compared to sample B (sucrose added $LiFePO_4$) yielding 2.64wt% carbon. Based on the above analyses that show a high concentration of graphitic carbon, pure phase $LiFePO_4$ with small crystallite sizes and

evenly distributed particle sizes, we expect these samples will display excellent electrochemical performance. A carbon-free $LiFePO_4$ (sample C), heat-treated at 600°C for 3 hours in 95% N_2 /5% H_2 at 20 cc/min, was used as a control sample. The XRD in Figure 43E from this control sample confirmed the pure $LiFePO_4$ phase and a SEM micrograph in Figure 44E displayed a decreasing particle size along with an increasing crystal size, which shown in Table 11.

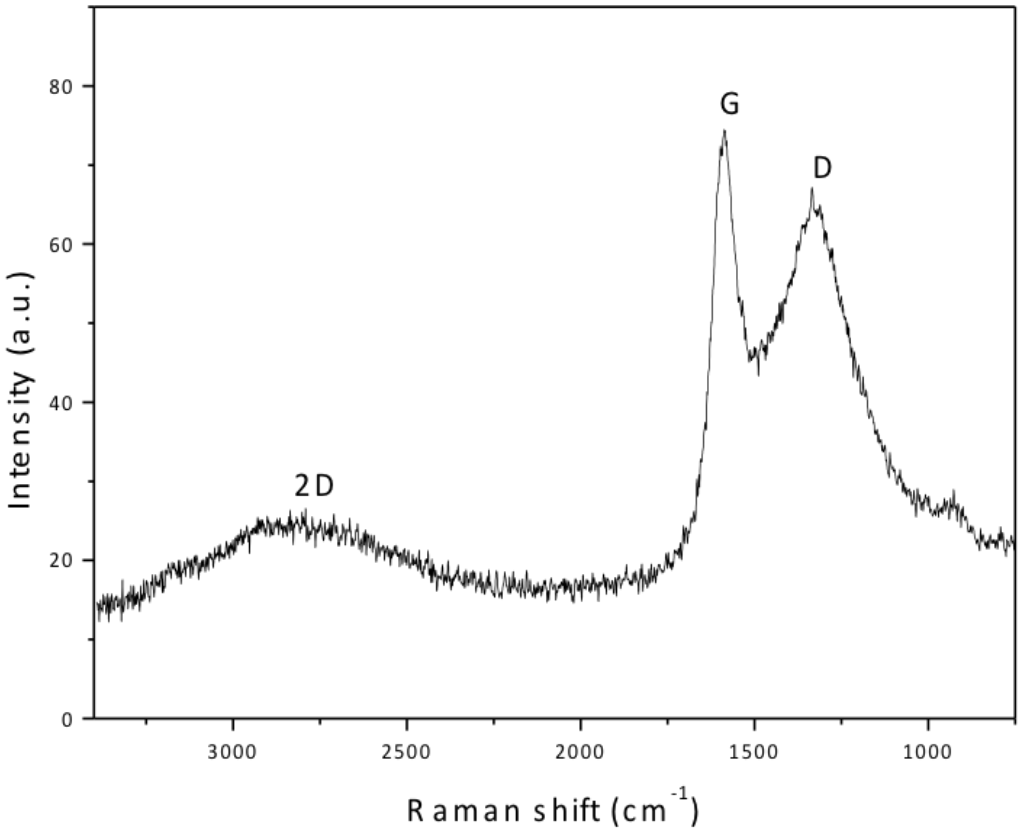

Figure 54. Raman spectroscopy of sucrose added LFP annealed at 600°C for 3 hours in 95% N_2 / 5% H_2 at 20cc/min.

Table 11. Crystal size and carbon content for samples A, B and C after heat-treatment at 600°C for 3hours.

Sample	Polymer added	Crystal size (nm)	Particle size (nm)	Carbon content after annealing (wt.%)
A	PEG added	52	457nm±154	0.41
B	Sucrose (wt.10%) added	41	340nm±180	2.64
C	Control (w/o polymer)	81	488nm±94	0

5.3.4 Electrochemical performance of $LiFePO_4$

5.3.4.1 CV curve

Cyclic voltammetry (CV) (Figure 55), which was performed at a scan rate of 0.1 mV/s at room temperature for three cycles, display an oxidation peak and reduction peak, corresponding to the charge/discharge reactions of the Fe^{2+}/Fe^{3+} redox couple. All of the second and third scans are the same as the first, suggesting the good reversibility of these cathodes. The carbon coated $LiFePO_4$ using PEG as the carbon source (sample A) displayed a voltage hysteresis (ca. 0.32 V) with peak current (0.23 A/g), while the carbon free $LiFePO_4$ (control sample C) specimen had a voltage difference of 0.60 V and a peak current of 0.11 A/g. It is known that smaller voltage differences between the charge and discharge, as well as higher peak currents, indicate better electrode reaction kinetics, and thus better rate performance. [160, 197] The results demonstrate that carbon coated $LiFePO_4$ show enhanced kinetics compared to carbon free $LiFePO_4$ during the lithiation and

delithiation due to the increased electronic conductivity through carbon additive. By looking at both carbon coated samples A and B, the voltage hysteresis is very close (0.32V for sample A and 0.31V for sample B) with the same peak current (0.23 A/g for both A and B), indicating the similar kinetics even though sample A (0.41%) has a much lower carbon content compared to B (2.64%). This demonstrates the advantages of our proposed method for the thin film carbon coating with enhanced tap density, thus higher volumetric energy density.

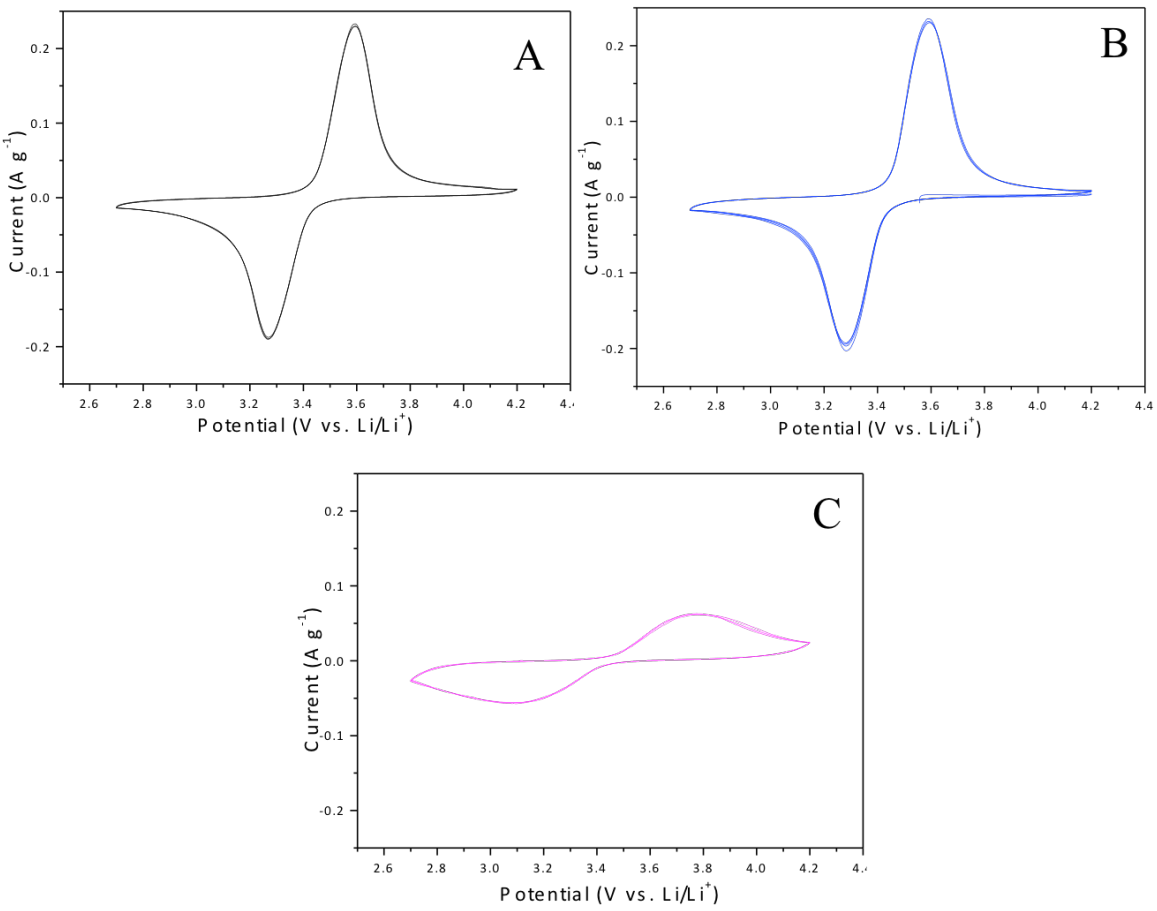

Figure 55. CV profiles of $LiFePO_4$ in the voltage range of 2.7-4.2 V at a scan rate of 0.1 mV/s for sample, (A) carbon coated $LiFePO_4$ using PEG as carbon source, (B) carbon coated $LiFePO_4$ using sucrose as carbon source, and (C) pure $LiFePO_4$ as control sample.

5.3.4.2 Charge/discharge capacities

Figure 56 shows the galvanostatic discharge capacity as a function of cycle number for carbon coated $LiFePO_4$ (sample A) at a current density of 16 mAh/g. The cells can delivery 130 mAh/g capacity after 70 cycles with ~ 92% capacity retention (Figure 56B), indicating the excellent storage ability. It was reported that very small (<2%) amounts of carbon can effectively increase the capacity retention.[218] Here, with less than 0.5% carbon in our $LiFePO_4$, the capacity retention was increased dramatically.

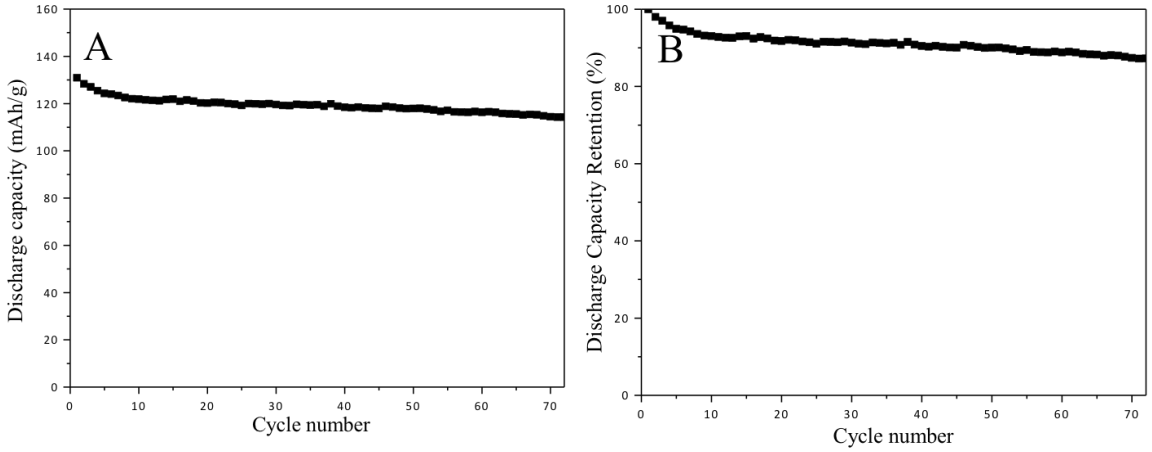

Figure 56. Discharge capacity vs. cycles for carbon coated $LiFePO_4$ using PEG as the carbon source, (A) cycling performance at 0.1C between 2.7 V and 4.2 V (vs. Li^+/Li) for 70 cycles, (B) discharge capacity retention.

Figure 57 shows the specific discharge capacity at different current rates (from 16 mAh/g to 320 mAh/g) for samples A, B and C. Our synthesized $LiFePO_4$ without carbon additive (sample C) delivers 115 mAh/g at 0.1C, which is better than the other reported data for carbon free $LiFePO_4$ (60 mAh/g at 0.1C).[101] After coating with 0.41% carbon, the capacity increased greatly (black square). The remarkable advantage of this carbon-coated material is its high rate capability (80 mAh/g at 2C) with extremely low carbon content. Its performance is comparable with the 2.64% coated $LiFePO_4$ (blue circle).

Thus, with low quantities of carbon additive, the tap density of $LiFePO_4$ increased from 1.1 to 1.8 g/cm^3 with the volumetric density increased by 40%.

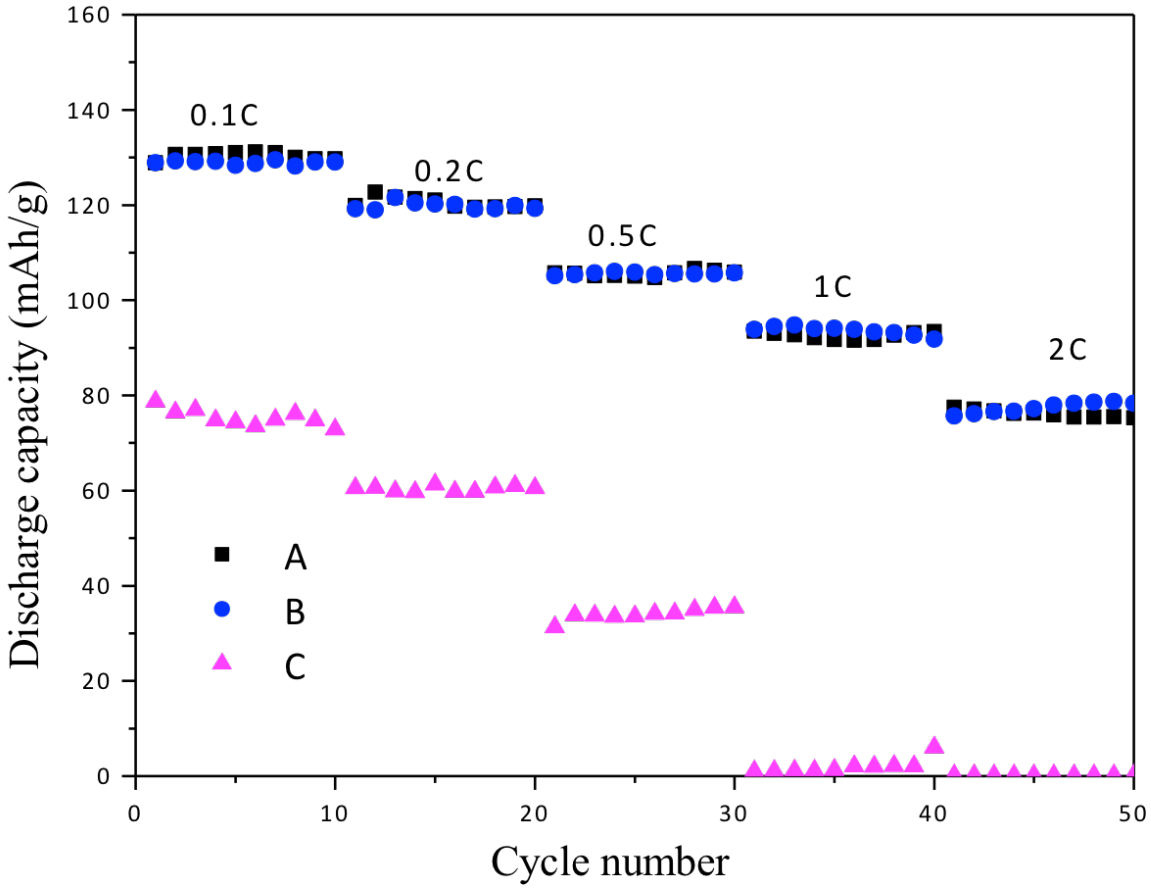

Figure 57. Carbon-coated and carbon-free $LiFePO_4$ cycling performance at various current rates between 2.7 V and 4.2 V (vs. Li^+/Li), (A) carbon coated $LiFePO_4$ using PEG as carbon source, (B) carbon coated $LiFePO_4$ using sucrose as carbon source, and (C) pure $LiFePO_4$ as a control sample.

5.4 Conclusions

We have successfully applied thin layer carbon coating on $LiFePO_4$ via a polyethylene glycol solution method. The core-shell structure was formed due to electrostatic absorption of the polymer onto $LiFePO_4$ particles and was subsequently transformed into a thin layer carbon-coated $LiFePO_4$ upon heat treatment in N_2/H_2. Less

than 0.5 wt. % of a multi-layer graphitic coating greatly increased the electronic conductivity and therefore the enhanced electrochemical performance. It is very promising for many applications since the carbon additive does not affect the theoretical volumetric energy and has an increased tap density compared to other high carbon content (~3 wt.%) cathodes.

Chapter 6.

Conclusions

The objective of this doctoral work was to investigate high efficiency lithium ion batteries used in both portable devices and hybrid electric vehicles through investigation of the structure-function relationships from a fundamental aspect. As one of the most important components in lithium ion batteries, cathodes play a key role to affect the whole cell parameters such as cell voltage, discharge capacity, and cycle life, etc. Therefore, they are extremely crucial and have received much attention in recent years. Both layered $Li[Ni_{1/3}Co_{1/3}Mn_{1/3}]O_2$ (NCM) structure and olivine $LiFePO_4$ structured materials are promising cathodes as they can provide high power and high energy.

As one of the promising cathodes that used in portable devices, $Li(Ni_{1/3}Co_{1/3}Mn_{1/3})O_2$ (NCM) has drawn much attention as it exhibits much higher capacity with enhanced safety compared to traditionally used $LiCoO_2$. However, there are some factors that limit the performance of this material such as relatively large particle sizes, inhomogeneous particle size distributions, and low packing densities. The particle size and distributions are strongly dependent on the synthesis methods and annealing processes. Consequently, a thorough understanding of the nucleation and growth of these materials in the synthesis process is of fundamental importance. At the same time, a thorough investigation of the performance-structure relationship is important and necessary to uncover the factors that caused the capacity fade, which will in turn guide our design for high efficiency lithium ion batteries.

Olivine $LiFePO_4$ (LFP) has been considered as the most promising cathode candidate for the next-generation large-scale lithium ion battery used for hybrid electric vehicles (HEVs) or electric vehicles (EVs). However, the application is hindered by a

low rate capacity due to the poor electronic conductivity and low lithium ion diffusivity. A various solutions have been applied to overcome this inherent deficiency of LFP such as size tailoring, conductive agents (carbon, silver, etc.) addition and cationic or anionic doping. In the process of all the above solutions, it is important to use a non-toxic and low cost synthesis system. Thus, it is necessary to understand the formation mechanism from the fundamental aspect for future cell design with further improved performance. In addition, decreasing the carbon coating is desired to improve the volumetric capacity while increasing the conductivity of LFP, which affect rate performance for the large applications in HEVs and EVs.

Chapter 2 reveals the fundamental crystal growth behavior of $Li(Ni_{1/3}Co_{1/3}Mn_{1/3})O_2$ cathode during the annealing process in a two-step synthesis route. Crystalline $Li(Ni_{1/3}Co_{1/3}Mn_{1/3})O_2$ started to form at 200°C from the mixture of $(Ni_{1/3}Co_{1/3}Mn_{1/3})(OH)_2$ and $LiOH{\cdot}H_2O$ precursors and was completed at 600°C as a pure phase with the α-$NaFeO_2$ structure. Above 700°C, significant crystal growth occurs with the presence of doublet peaks for the (006)/(102) at 37°(2θ) and the (108)/(110) reflections at 65°(2θ), which is an indication of an ordered hexagonal layered structure that enables the reduction of cationic mixing during intercalation and de-intercalation of lithium ions inside the host matrix. Three separate growth regimes during the $Li(Ni_{1/3}Co_{1/3}Mn_{1/3})O_2$ annealing process were observed from 600°C to 1000°C. At temperatures below 750 °C, surface diffusion is expected to be the dominant growth mechanism based on minimal crystal growth and a small rate-controlling exponent 1/n. At the annealing temperatures from 800^{o}C and 900^{o}C, crystal growth is controlled by the

volume diffusion, while grain boundary diffusion is the predominant mechanism for the temperature range of 900^{o}C – 1000^{o}C. The information revealed by this study will help develop guidelines to control the size and morphological features more precisely, and will help create design strategies for cathodes that will enable efficient lithium ion transport and extended lifetime batteries.

Chapter 3 studied effects of crystal structure and size effects on the performance degradation of $Li(Ni_{1/3}Co_{1/3}Mn_{1/3})O_2$. The cation ordering and crystal sizes increased with increasing annealing temperature from 750°C to 1000°C. The higher cationic ordering yielded better performance for crystal sizes less than 500 nm. Beyond that, crystal size had a key effect on the electrochemical performance, especially for the high current density and discharge capacity. These cathodes underwent a lattice parameter increase and volume expansion after cycling for all samples with various crystal sizes (28 nm, 166 nm, 458 nm and 850 nm). The sample with biggest crystal size showed the highest change due to the lower strain accommodation at 1000°C. The lattice parameter "c" displayed a larger change compared to "a", indicating an anisotropic microstructural degradation preference.

Chapter 4 uncovered the formation mechanism of $LiFePO_4$ nanostructures in a water-triethylene glycol system and investigated the relationship between the resulting structures and performance. Initially, thin (100 nm) platelets of $Fe_3(PO_4)_2 \cdot 8H_2O$ (vivianite, VTE) formed at short reaction times followed by the nucleation of LFP (20 nm particles) on the metastable high energy VTE surfaces. As these primary particles are formed, the reaction pH decreased, which reduced the surface charge on $LiFePO_4$

primary particles. This reduction in surface charge enabled the primary particles to approach each other and attach in an oriented manner to form secondary particles. These diamond-like LFP particles are oriented along the (010) plane and elongated in the high surface energy direction of [001]. With increasing reaction duration, the pH further decreased, promoting crystallization and densification (Ostwald ripening, OR) of LFP due to its increased solubility. Electrochemical characterization of carbon-free LFP materials demonstrated a discharge capacity of more than 100 mAh/g. Polycrystalline particles with smaller primary crystallite diameters afforded a higher discharge capacity and better kinetics compared to the single crystalline particles. Based on our understanding of the formation mechanism and the structure-performance relationships in $LiFePO_4$ using an environmental friendly synthetic method, we will continue to produce the $LiFePO_4$ with shorter lithium diffusion paths to improve the battery performance.

Chapter 5 studied the effective carbon coatings of LFP via a polymer solution method. Pristine olivine structured $LiFePO_4$ remained stable up to 600°C, but underwent a rapid reduction reaction from $LiFePO_4$ to Fe_2P above 700°C. The LFP core – carbon shell structure was formed due to electrostatic absorption of the polymer onto $LiFePO_4$ particles and was subsequently transformed into a thin layer carbon-coated $LiFePO_4$ upon heat treatment in N_2/H_2. Less than 0.5 wt. % of a multi-layer graphitic coating greatly increased the electronic conductivity and therefore the enhanced electrochemical performance. Both PEG and sucrose carbon-based sources yielded high quality carbon coatings after annealing, as determined by the graphitic/disordered, G/D, ratios of 1.30 and 1.20, respectively. By producing more uniform and coherent coatings on $LiFePO_4$

particles, we were able to produce batteries with a discharge capacity of 80mAh/g at 2C with significantly less carbon (i.e., 0.41 wt.%) with comparable performance to traditionally synthesized carbon-coated $LiFePO_4$ with higher carbon loadings (ca. 2.64 wt.%). This will enable us to produce batteries with higher active material loading and therefore, significantly larger energy densities.

References

1. Holdren, J. P., Energy and Sustainability. *Science* 2007, 315, 737.
2. Ginley, D.; Green, M. A.; Collins, R., Solar Energy Conversion Toward 1 Terawatt. *MRS Bulletin* 2008, 33, 355-364.
3. Goodenough, J. B.; Kim, Y., Challenges for Rechargeable Li Batteries. *Chem. Mater.* 2009, 22, 587-603.
4. Simon, P.; Gogotsi, Y., Materials for electrochemical capacitors. *Nature Materials* 2008, 7, 845-854.
5. Soon-Ki, J.; Inaba, M.; Abe, T.; Ogumi, Z., Surface film formation on graphite negative electrode in lithium-ion batteries: AFM study in an ethylene carbonate-based solution. *J. Electrochem. Soc.* 2001, 148, A989-93.
6. Obrovac, M. N.; Christensen, L.; Le, D. B.; Dahnb, J. R., Alloy design for lithium-ion battery anodes. *J. Electrochem. Soc.* 2007, 154, A849-A855.
7. Flandrois, S.; Simon, B., Carbon materials for lithium-ion rechargeable batteries. *Carbon* 1999, 37, 165-180.
8. Scrosati, B., Recent advances in lithium ion battery materials. *Electrochim. Acta* 2000, 45, 2461-2466.
9. Idota, Y.; Kubota, T.; Matsufuji, A.; Maekawa, Y.; Miyasaka, T., Tin-based amorphous oxide: A high-capacity lithium-ion-storage material. *Science* 1997, 276, 1395-1397.
10. Kepler, K. D.; Vaughey, J. T.; Thackeray, M. M., Li(x)Cu(6)Sn(5) ($0 < x < 13$): An intermetallic insertion electrode for rechargeable lithium batteries. *Electrochemical and Solid State Letters* 1999, 2, 307-309.
11. Sreeraj, P.; Wiemhoefer, H.-D.; Hoffmann, K.-D.; Walter, J.; Kirfel, A.; Poettgen, R., Neutron diffraction and electrochemical studies on $Li_{1-x}Ag_2Sn$. *Solid State Sciences* 2006, 8, 843-848.
12. Gholam-Abbas Nazri, G. P., *Lithium battery science and technology*. Springer: 2009; p 708.
13. Chen, C. H.; Vaughey, J. T.; Jansen, A. N.; Dees, D. W.; Kahaian, A. J.; Goacher, T.; Thackeray, M. M., Studies of Mg-substituted $Li_{4-x}Mg_xTi_5O_{12}$ spinel electrodes ($0 <= x <= 1$) for lithium batteries. *J. Electrochem. Soc.* 2001, 148, A102-A104.
14. Ferg, E.; Gummow, R. J.; Dekock, A.; Thackeray, M. M., SPINEL ANODES FOR LITHIUM-ION BATTERIES. *J. Electrochem. Soc.* 1994, 141, L147-L150.
15. Li, S.; Jiaping, W.; Kaili, J.; Shoushan, F., Mesoporous $Li_4Ti_5O_{12}$ nanoclusters as high performance negative electrodes for lithium ion batteries. *J. Power Sources* 2014, 248, 265-72.
16. Zaghib, K.; Simoneau, M.; Armand, M.; Gauthier, M., Electrochemical study of $Li_4Ti_5O_{12}$ as negative electrode for Li-ion polymer rechargeable batteries. *J. Power Sources* 1999, 81, 300-305.
17. Kim, J. H.; Kang, Y. C., Electrochemical Properties of Nano-sized $Li_4Ti_5O_{12}$ Powders Prepared by Flame Spray Pyrolysis. *International Journal of Electrochemical Science* 2013, 8, 3379-3389.

18. Wu, H.; Huang, Y.; Jia, D.; Guo, Z.; Miao, M., Preparation and characterization of spinel $Li_4Ti_5O_{12}$ nanoparticles anode materials for lithium ion battery. *Journal of Nanoparticle Research* 2012, 14.
19. Shin, J.-W.; Ryu, J. H.; Jeong, J.; Yoon, D.-H., Effects of post-treatments on the electrochemical properties of solid-state reacted $Li_4Ti_5O_{12}$-high energy milling and annealing. *Journal of Electroceramics* 2012, 28, 178-184.
20. Zheng, X.-D.; Dong, C.-C.; Huang, B.; Lu, M., High-rate $Li_4Ti_5O_{12}$/C composites as anode for lithium-ion batteries. *Ionics* 2013, 19, 385-389.
21. Yin, Y.; Li, S.; Cao, Z.; Yue, H.; Ding, X.; Yang, S., Preparation of $Li_4Ti_5O_{12}$/C composites using gel-cast method and its electrochemical performance. *Solid State Ionics* 2013, 241, 1-4.
22. Fang, W.; Zuo, P.; Ma, Y.; Cheng, X.; Liao, L.; Yin, G., Facile preparation of $Li_4Ti_5O_{12}$/AB/MWCNTs composite with high-rate performance for lithium ion battery. *Electrochim. Acta* 2013, 94, 294-299.
23. Dominko, R.; Bele, M.; Kokalj, A.; Gaberscek, M.; Jamnik, J., Li_2MnSiO_4 as a potential Li-battery cathode material. *J. Power Sources* 2007, 174, 457-461.
24. Qingtang, Z.; Yongle, Z.; Ce, S.; Mingyang, L., Nano/Micro Lithium Transitionmetal (Fe, Mn, Co and Ni) Silicate Cathode Materials for Lithium Ion Batteries. *Recent Patents on Nanotechnology* 2011, 5, 225-33.
25. Seo, D.-H.; Park, Y.-U.; Kim, S.-W.; Park, I.; Shakoor, R. A.; Kang, K., First-principles study on lithium metal borate cathodes for lithium rechargeable batteries. *Phys. Rev. B* 2011, 83.
26. Cheng, W. D.; Zhang, H.; Lin, Q. S.; Zheng, F. K.; Chen, J. T., Syntheses, crystal and electronic structures, and linear optics of $LiMBO_3$ (M = Sr, Ba) orthoborates. *Chem. Mater.* 2001, 13, 1841-1847.
27. Tripathi, R.; Gardiner, G. R.; Islam, M. S.; Nazar, L. F., Alkali-ion Conduction Paths in $LiFeSO_4F$ and $NaFeSO_4F$ Tavorite-Type Cathode Materials. *Chem. Mater.* 2011, 23, 2278-2284.
28. Mueller, T.; Hautier, G.; Jain, A.; Ceder, G., Evaluation of Tavorite-Structured Cathode Materials for Lithium-Ion Batteries Using High-Throughput Computing. *Chem. Mater.* 2011, 23, 3854-3862.
29. Guo, Y.-G.; Hu, J.-S.; Wan, L.-J., Nanostructured materials for electrochemical energy conversion and storage devices. *Advanced Materials* 2008, 20, 2878-2887.
30. Shao-Horn, Y.; Croguennec, L.; Delmas, C.; Nelson, E. C.; O'Keefe, M. A., Atomic resolution of lithium ions in $LiCoO_2$. *Nat Mater* 2003, 2, 464-467.
31. Mizushima, K.; Jones, P. C.; Wiseman, P. J.; Goodenough, J. B., Li_xCoO_2: A new cathode material for batteries of high energy density. *Mater. Res. Bull.* 1980, 15, 783-789.
32. Shao-Horn, Y.; Levasseur, S.; Weill, F.; Delmas, C., Probing lithium and vacancy ordering in O3 layered Li_xCoO_2 (x approximate to 0.5) - An electron diffraction study. *J. Electrochem. Soc.* 2003, 150, A366-A373.
33. Amatucci, G. G.; Tarascon, J. M.; Klein, L. C., Cobalt dissolution in $LiCoO_2$-based non-aqueous rechargeable batteries. *Solid State Ionics* 1996, 83, 167-173.

34. Mladenov, M.; Stoyanova, R.; Zhecheva, E.; Vassilev, S., Effect of Mg doping and MgO-surface modification on the cycling stability of $LiCoO_2$ electrodes. *Electrochem. Commun.* 2001, 3, 410-416.
35. Kweon, H. J.; Kim, S. J.; Park, D. G., Modification of $Li_xNi_{1-y}Co_yO_2$ by applying a surface coating of MgO. *J. Power Sources* 2000, 88, 255-261.
36. Chen, Z. H.; Dahn, J. R., Effect of a ZrO_2 coating on the structure and electrochemistry of Li_xCoO_2 when cycled to 4.5 V. *Electrochemical and Solid State Letters* 2002, 5, A213-A216.
37. Ohzuku, T.; Ueda, A.; Nagayama, M.; Iwakoshi, Y.; Komori, H., Comparative-study of $LiCoO_2$, $LiNi_{1/2}Co_{1/2}O_2$ and $LiNiO_2$ for 4-volt secondary lithium cells. *Electrochim. Acta* 1993, 38, 1159-1167.
38. Dahn, J. R.; Vonsacken, U.; Michal, C. A., Structure and electrochemistry of $Li_{1\pm y}NiO_2$ and a new Li_2NiO_2 phase with the $Ni(OH)_2$ structure. *Solid State Ionics* 1990, 44, 87-97.
39. Li, W.; Reimers, J. N.; Dahn, J. R., In-situ X-Ray diffraction and electrochemical studies of $Li_{1-x}NiO_2$. *Solid State Ionics* 1993, 67, 123-130.
40. Rougier, A.; Gravereau, P.; Delmas, C., Optimization of the composition of the $Li_{1-z}Ni_{1+z}O_2$ electrode materials: Structural, magnetic, and electrochemical studies. *J. Electrochem. Soc.* 1996, 143, 1168-1175.
41. Liu, H. S.; Zhang, Z. R.; Gong, Z. L.; Yang, Y., Origin of deterioration for $LiNiO_2$ cathode material during storage in air. *Electrochemical and Solid State Letters* 2004, 7, A190-A193.
42. Delmas, C.; Peres, J. P.; Rougier, A.; Demourgues, A.; Weill, F.; Chadwick, A.; Broussely, M.; Perton, F.; Biensan, P.; Willmann, P., On the behavior of the Li_xNiO_2 system: an electrochemical and structural overview. *J. Power Sources* 1997, 68, 120-125.
43. Kim, J.; Amine, K., A comparative study on the substitution of divalent, trivalent and tetravalent metal ions in $LiNi_{1-x}M_xO_2$ ($M = Cu^{2+}$, Al^{3+} and Ti^{4+}). *J. Power Sources* 2002, 104, 33-39.
44. Ohzuku, T.; Makimura, Y., Layered lithium insertion material of $LiCo_{1/3}Ni_{1/3}Mn_{1/3}O_2$ for lithium-ion batteries. *Chemistry Letters* 2001, 642-643.
45. Choi, J.; Manthiram, A., Role of chemical and structural stabilities on the electrochemical properties of layered $LiCo_{1/3}Ni_{1/3}Mn_{1/3}O_2$ cathodes. *J. Electrochem. Soc.* 2005, 152, A1714-A1718.
46. Shaju, K. M.; Bruce, P. G., Macroporous $LiCo_{1/3}Ni_{1/3}Mn_{1/3}O_2$: A high-power and high-energy cathode for rechargeable lithium batteries. *Advanced Materials* 2006, 18, 2330.
47. Yabuuchi, N.; Makimura, Y.; Ohzuku, T., Solid-state chemistry and electrochemistry of $LiCo_{1/3}Ni_{1/3}Mn_{1/3}O_2$ for advanced lithium-ion batteries III. Rechargeable capacity and cycleability. *J. Electrochem. Soc.* 2007, 154, A314-A321.
48. Lu, Z. H.; MacNeil, D. D.; Dahn, J. R., Layered $LiNi_xCo_{1-2x}Mn_xO_2$ cathode materials for lithium-ion batteries. *Electrochemical and Solid State Letters* 2001, 4, A200-A203.

49. Hwang, B. J.; Tsai, Y. W.; Carlier, D.; Ceder, G., A Combined Computational/Experimental Study on $LiCo_{1/3}Ni_{1/3}Mn_{1/3}O_2$. *Chem. Mater.* 2003, 15, 3676-3682.
50. Belharouak, I.; Sun, Y. K.; Liu, J.; Amine, K., $LiNi_{1/3}Co_{1/3}Mn_{1/3}O_2$ as a suitable cathode for high power applications. *J. Power Sources* 2003, 123, 247-252.
51. Ren, H.; Mu, X.; Huang, Y.; Li, Z.; Wang, Y.; Cai, P.; Peng, Z.; Zhou, Y., Effects of Sn doping on electrochemical characterizations of $LiNi_{1/3}Co_{1/3}Mn_{1/3}O_2$ cathode material. *Ionics* 2010, 16, 497-502.
52. Kim, S. H.; Shim, K. B.; Han, K. R.; Kim, C.-S., Electrochemical properties of Al doped $LiCo_{1/3}Ni_{1/3}Mn_{1/3}O_2$. In *Advances in Nanomaterials and Processing, Pts 1 and 2*, Ahn, B. T.; Jeon, H.; Hur, B. Y.; Kim, K.; Park, J. W., Eds. 2007; Vol. 124-126, pp 1023-1026.
53. Yang, S.-y.; Wang, X.-y.; Liu, Z.-l.; Chen, Q.-q.; Yang, X.-k.; Wei, Q.-l., Influence of pretreatment process on structure, morphology and electrochemical properties of $LiNi_{1/3}Co_{1/3}Mn_{1/3}O_2$ cathode material. *Transactions of Nonferrous Metals Society of China* 2011, 21, 1995-2001.
54. Lin, B.; Wen, Z.; Gu, Z.; Huang, S., Morphology and electrochemical performance of $LiNi_{1/3}Co_{1/3}Mn_{1/3}O_2$ cathode material by a slurry spray drying method. *J. Power Sources* 2008, 175, 564-569.
55. Yun, S. H.; Park, K.-S.; Park, Y. J., The electrochemical property of ZrF_x-coated $LiNi_{1/3}Co_{1/3}Mn_{1/3}O_2$ cathode material. *J. Power Sources* 2010, 195, 6108-6115.
56. Lin, B.; Wen, Z.; Han, J.; Wu, X., Electrochemical properties of carbon-coated $LiNi_{1/3}Co_{1/3}Mn_{1/3}O_2$ cathode material for lithium-ion batteries. *Solid State Ionics* 2008, 179, 1750-1753.
57. Huang, Y.; Chen, J.; Cheng, F.; Wan, W.; Liu, W.; Zhou, H.; Zhang, X., A modified Al_2O_3 coating process to enhance the electrochemical performance of $LiNi_{1/3}Co_{1/3}Mn_{1/3}O_2$ and its comparison with traditional Al_2O_3 coating process. *J. Power Sources* 2010, 195, 8267-8274.
58. Xia, Y. Y.; Zhou, Y. H.; Yoshio, M., Capacity fading on cycling of 4 V $Li/LiMn_2O_4$ cells. *J. Electrochem. Soc.* 1997, 144, 2593-2600.
59. Tarascon, J. M.; Wang, E.; Shokoohi, F. K.; McKinnon, W. R.; Colson, S., The spinel phase of $LiMn_2O_4$ as a cathode in secondary lithium cells. *J. Electrochem. Soc.* 1991, 138, 2859-2864.
60. Liu, W.; Farrington, G. C.; Chaput, F.; Dunn, B., Synthesis and electrochemical studies of spinel phase $LiMn_2O_4$ cathode materials prepared by the Pechini process. *J. Electrochem. Soc.* 1996, 143, 879-884.
61. Lee, S.; Oshima, Y.; Hosono, E.; Zhou, H.; Kim, K.; Chang, H. M.; Kanno, R.; Takayanagi, K., In Situ TEM Observation of Local Phase Transformation in a Rechargeable $LiMn_2O_4$ Nanowire Battery. *Journal of Physical Chemistry C* 2013, 117, 24236-24241.
62. Hong, H. P.; Kim, M. S.; Lee, Y. H.; Yu, J. S.; Lee, C. J.; Min, N. K., Spray deposition of $LiMn_2O_4$ nanoparticle-decorated multiwalled carbon nanotube films as cathode material for lithium-ion batteries. *Thin Solid Films* 2013, 547, 68-71.

63. Park, S. B.; Shin, H. C.; Lee, W.-G.; Cho, W. I.; Jang, H., Improvement of capacity fading resistance of $LiMn_2O_4$ by amphoteric oxides. *J. Power Sources* 2008, 180, 597-601.
64. Fu, M. H.; Huang, K. L.; Liu, S. Q.; Liu, J. S.; Li, Y. K., Lithium difluoro(oxalato)borate/ethylene carbonate plus propylene carbonate plus ethyl(methyl) carbonate electrolyte for $LiMn_2O_4$ cathode. *J. Power Sources* 2010, 195, 862-866.
65. Thackeray, M. M.; David, W. I. F.; Bruce, P. G.; Goodenough, J. B., Lithium insertion into manganese spinels. *Mater. Res. Bull.* 1983, 18, 461-472.
66. Winter, M.; Besenhard, J. O.; Spahr, M. E.; Novak, P., Insertion electrode materials for rechargeable lithium batteries. *Advanced Materials* 1998, 10, 725-763.
67. Nakayama, M.; Nogami, M., A first-principles study on phase transition induced by charge ordering of Mn^{3+}/Mn^{4+} in spinel $LiMn_2O_4$. *Solid State Commun.* 2010, 150, 1329-1333.
68. Terada, Y.; Nishiwaki, Y.; Nakai, I.; Nishikawa, F., Study of Mn dissolution from $LiMn_2O_4$ spinel electrodes using in situ total reflection X-ray fluorescence analysis and fluorescence XAFS technique. *J. Power Sources* 2001, 97-8, 420-422.
69. Amatucci, G. G.; Schmutz, C. N.; Blyr, A.; Sigala, C.; Gozdz, A. S.; Larcher, D.; Tarascon, J. M., Materials' effects on the elevated and room temperature performance of C/ $LiMn_2O_4$ Li-ion batteries. *J. Power Sources* 1997, 69, 11-25.
70. Capsoni, D.; Bini, M.; Chiodelli, G.; Massarotti, V.; Mozzati, M. C.; Azzoni, C. B., Structural transition in Mg-doped $LiMn_2O_4$: a comparison with other M-doped Li-Mn spinels. *Solid State Commun.* 2003, 125, 179-183.
71. Xiao, L.; Zhao, Y.; Yang, Y.; Cao, Y.; Ai, X.; Yang, H., Enhanced electrochemical stability of Al-doped $LiMn_2O_4$ synthesized by a polymer-pyrolysis method. *Electrochim. Acta* 2008, 54, 545-550.
72. Zhang, Z.; Chen, M.; Xiang, M.; Feng, L.; Zhang, Y.; Guo, J., Effect of Cr Doping on Electrochemical Performance of $LiMn_2O_4$. In *Advances in Materials and Materials Processing, Pts 1-3*, Jiang, Z. Y.; Liu, X. H.; Jiao, S. H.; Han, J. T., Eds. 2013; Vol. 652-654, pp 848-852.
73. Xu, Y.; Chen, G.; Fu, E.; Zhou, M.; Dunwell, M.; Fei, L.; Deng, S.; Andersen, P.; Wang, Y.; Jia, Q.; Luo, H., Nickel substituted $LiMn_2O_4$ cathode with durable high-rate capability for Li-ion batteries. *Rsc Advances* 2013, 3, 18441-18445.
74. Jayaprakash, N.; Kalaiselvi, N.; Gangulibabu; Bhuvaneswari, D., Effect of mono- (Cr) and bication (Cr, V) substitution on $LiMn_2O_4$ spinel cathodes. *Journal of Solid State Electrochemistry* 2011, 15, 1243-1251.
75. Liu, W.; Kowal, K.; Farrington, G. C., Electrochemical characteristics of spinel phase $LiMn_2O_4$-based cathode materials prepared by the Pechini process - Influence of firing temperature and dopants. *J. Electrochem. Soc.* 1996, 143, 3590-3596.
76. Yi, T.-F.; Yin, L.-C.; Ma, Y.-Q.; Shen, H.-Y.; Zhu, Y.-R.; Zhu, R.-S., Lithium-ion insertion kinetics of Nb-doped $LiMn_2O_4$ positive-electrode material. *Ceramics International* 2013, 39, 4673-4678.
77. Khedr, A. M.; Abou-Sekkina, M. M.; El-Metwaly, F. G., Synthesis, Structure, and Electrochemistry of Sm-Modified $LiMn_2O_4$ Cathode Materials for Lithium-Ion Batteries. *Journal of Electronic Materials* 2013, 42, 1275-1281.

78. Kim, J. H.; Myung, S. T.; Sun, Y. K., Molten salt synthesis of $LiNi_{0.5}Mn_{1.5}O_4$ spinel for 5 V class cathode material of Li-ion secondary battery. *Electrochim. Acta* 2004, 49, 219-227.
79. Lee, Y. S.; Sun, Y. K.; Ota, S.; Miyashita, T.; Yoshi, M., Preparation and characterization of nano-crystalline $LiNi_{0.5}Mn_{1.5}O_4$ for 5 V cathode material by composite carbonate process. *Electrochem. Commun.* 2002, 4, 989-994.
80. Myung, S. T.; Komaba, S.; Kumagai, N.; Yashiro, H.; Chung, H. T.; Cho, T. H., Nano-crystalline $LiNi_{0.5}Mn_{1.5}O_4$ synthesized by emulsion drying method. *Electrochim. Acta* 2002, 47, 2543-2549.
81. Sun, Y. K.; Hong, K. J.; Prakash, J.; Amine, K., Electrochemical performance of nano-sized ZnO-coated $LiNi_{0.5}Mn_{1.5}O_4$ spinel as 5 V materials at elevated temperatures. *Electrochem. Commun.* 2002, 4, 344-348.
82. Xu, B.; Qian, D.; Wang, Z.; Meng, Y. S., Recent progress in cathode materials research for advanced lithium ion batteries. *Materials Science & Engineering R-Reports* 2012, 73, 51-65.
83. Prosini, P. P.; Lisi, M.; Zane, D.; Pasquali, M., Determination of the chemical diffusion coefficient of lithium in $LiFePO_4$. *Solid State Ionics* 2002, 148, 45-51.
84. Chung, S. Y.; Bloking, J. T.; Chiang, Y. M., Electronically conductive phospho-olivines as lithium storage electrodes. *Nature Materials* 2002, 1, 123-128.
85. Li, G. H.; Azuma, H.; Tohda, M., $LiMnPO_4$ as the cathode for lithium batteries. *Electrochemical and Solid State Letters* 2002, 5, A135-A137.
86. Amine, K.; Yasuda, H.; Yamachi, M., Olivine $LiCoPO_4$ as 4.8 V electrode material for lithium batteries. *Electrochemical and Solid State Letters* 2000, 3, 178-179.
87. Wolfenstine, J.; Allen, J., Ni^{3+}/Ni^{2+} redox potential in LiNiPO4. *J. Power Sources* 2005, 142, 389-390.
88. Saravanan, K.; Vittal, J. J.; Reddy, M. V.; Chowdari, B. V. R.; Balaya, P., Storage performance of $LiFe_{1-x}Mn_xPO_4$ nanoplates (x=0, 0.5, and 1). *Journal of Solid State Electrochemistry* 2010, 14, 1755-1760.
89. Shu, H.; Wang, X.; Wu, Q.; Hu, B.; Yang, X.; Wei, Q.; Liang, Q.; Bai, Y.; Zhou, M.; Wu, C.; Chen, M.; Wang, A.; Jiang, L., Improved electrochemical performance of $LiFePO_4$/C cathode via Ni and Mn co-doping for lithium-ion batteries. *J. Power Sources* 2013, 237, 149-155.
90. Lu, Y.; Shi, J.; Guo, Z.; Tong, Q.; Huang, W.; Li, B., Synthesis of $LiFe_{1-x}Ni_xPO_4$/C composites and their electrochemical performance. *J. Power Sources* 2009, 194, 786-793.
91. Ge, Y.; Yan, X.; Liu, J.; Zhang, X.; Wang, J.; He, X.; Wang, R.; Xie, H., An optimized Ni doped $LiFePO_4$/C nanocomposite with excellent rate performance. *Electrochim. Acta* 2010, 55, 5886-5890.
92. Zhao, R.-r.; Hung, I. M.; Li, Y.-T.; Chen, H.-y.; Lin, C.-P., Synthesis and properties of Co-doped $LiFePO_4$ as cathode material via a hydrothermal route for lithium-ion batteries. *Journal of Alloys and Compounds* 2012, 513, 282-288.
93. Hautier, G.; Jain, A.; Ong, S. P.; Kang, B.; Moore, C.; Doe, R.; Ceder, G., Phosphates as Lithium-Ion Battery Cathodes: An Evaluation Based on High-Throughput ab Initio Calculations. *Chem. Mater.* 2011, 23, 3495-3508.

94. Ravet, N.; Chouinard, Y.; Magnan, J. F.; Besner, S.; Gauthier, M.; Armand, M., Electroactivity of natural and synthetic triphylite. *J. Power Sources* 2001, 97–98, 503-507.
95. Chen, Z. H.; Dahn, J. R., Reducing carbon in $LiFePO_4$/C composite electrodes to maximize specific energy, volumetric energy, and tap density. *J. Electrochem. Soc.* 2002, 149, A1184-A1189.
96. Park, K. S.; Son, J. T.; Chung, H. T.; Kim, S. J.; Lee, C. H.; Kang, K. T.; Kim, H. G., Surface modification by silver coating for improving electrochemical properties of $LiFePO_4$. *Solid State Commun.* 2004, 129, 311-314.
97. Liu, H.; Wang, G. X.; Wexler, D.; Wang, J. Z.; Liu, H. K., Electrochemical performance of $LiFePO_4$ cathode material coated with ZrO_2 nanolayer. *Electrochem. Commun.* 2008, 10, 165-169.
98. Islam, M. S.; Driscoll, D. J.; Fisher, C. A. J.; Slater, P. R., Atomic-Scale Investigation of Defects, Dopants, and Lithium Transport in the $LiFePO_4$ Olivine-Type Battery Material. *Chem. Mater.* 2005, 17, 5085-5092.
99. Morgan, D.; Van der Ven, A.; Ceder, G., Li conductivity in Li_xMPO_4 (M = Mn, Fe, Co, Ni) olivine materials. *Electrochemical and Solid State Letters* 2004, 7, A30-A32.
100. Fisher, C. A. J.; Hart Prieto, V. M.; Islam, M. S., Lithium Battery Materials $LiMPO_4$ (M = Mn, Fe, Co, and Ni): Insights into Defect Association, Transport Mechanisms, and Doping Behavior. *Chem. Mater.* 2008, 20, 5907-5915.
101. Yang, S.; Zhou, X.; Zhang, J.; Liu, Z., Morphology-controlled solvothermal synthesis of $LiFePO_4$ as a cathode material for lithium-ion batteries. *J. Mater. Chem.* 2010, 20, 8086-8091.
102. Malik, R.; Burch, D.; Bazant, M.; Ceder, G., Particle Size Dependence of the Ionic Diffusivity. *Nano Letters* 2010, 10, 4123-4127.
103. Ramesh, T. N.; Lee, K. T.; Ellis, B. L.; Nazar, L. F., Tavorite Lithium Iron Fluorophosphate Cathode Materials: Phase Transition and Electrochemistry of $LiFePO_4F$-Li_2FePO_4F. *Electrochemical and Solid State Letters* 2010, 13, A43-A47.
104. Dominko, R., Li_2MSiO_4 (M = Fe and/or Mn) cathode materials. *J. Power Sources* 2008, 184, 462-468.
105. Muraliganth, T.; Stroukoff, K. R.; Manthiram, A., Microwave-Solvothermal Synthesis of Nanostructured Li_2MSiO_4/C (M = Mn and Fe) Cathodes for Lithium-Ion Batteries. *Chem. Mater.* 2010, 22, 5754-5761.
106. Arroyo-de Dompablo, M. E.; Armand, M.; Tarascon, J. M.; Amador, U., On-demand design of polyoxianionic cathode materials based on electronegativity correlations: An exploration of the Li_2MSiO_4 system (Fe, Mn, Co, Ni). *Electrochem. Commun.* 2006, 8, 1292-1298.
107. Arroyo-de Dompablo, M. E.; Armand, M.; Tarascon, J. M.; Amador, U., On-demand design of polyoxianionic cathode materials based on electronegativity correlations: An exploration of the Li_2MSiO_4 system (M = Fe, Mn, Co, Ni). *Electrochem. Commun.* 2006, 8, 1292-1298.
108. Ozawa, K., Lithium ion rechargeable batteries with $LiCoO_2$ and carbon electrodes-the $LiCoO_2$ C system. *Solid State Ionics* 1994, 69, 212-221.

109. Shaju, K. M.; Rao, G. V. S.; Chowdari, B. V. R., Performance of layered $Li(Ni_{1/3}Co_{1/3}Mn_{1/3})O_2$ as cathode for Li-ion batteries. *Electrochim. Acta* 2002, 48, 145-151.
110. Cho, T. H.; Park, S. M.; Yoshio, M., Preparation of layered $Li(Ni_{1/3}Co_{1/3}Mn_{1/3})O_2$ as a cathode for lithium secondary battery by carbonate coprecipitation method. *Chemistry Letters* 2004, 33, 704-705.
111. Lee, M. H.; Kang, Y.; Myung, S. T.; Sun, Y. K., Synthetic optimization of $Li(Ni_{1/3}Co_{1/3}Mn_{1/3})O_2$ via co-precipitation. *Electrochim. Acta* 2004, 50, 939-948.
112. Yabuuchi, N.; Ohzuku, T., Novel lithium insertion material of $LiCo_{1/3}Ni_{1/3}Mn_{1/3}O_2$ for advanced lithium-ion batteries. *J. Power Sources* 2003, 119, 171-174.
113. Zhang, L.; Wang, X.; Muta, T.; Li, D.; Noguchi, H.; Yoshio, M.; Ma, R.; Takada, K.; Sasaki, T., The effects of extra Li content, synthesis method, sintering temperature on synthesis and electrochemistry of layered $Li(Ni_{1/3}Co_{1/3}Mn_{1/3})O_2$. *J. Power Sources* 2006, 162, 629-635.
114. Cho, T. H.; Park, S. M.; Yoshio, M.; Hirai, T.; Hideshima, Y., Effect of synthesis condition on the structural and electrochemical properties of $Li(Ni_{1/3}Co_{1/3}Mn_{1/3})O_2$ prepared by carbonate co-precipitation method. *J. Power Sources* 2005, 142, 306-312.
115. Guo, J.; Jiao, L. F.; Yuan, H. T.; Li, H. X.; Zhang, M.; Wang, Y. M., Effect of synthesis condition on the structural and electrochemical properties of $Li(Ni_{1/3}Co_{1/3}Mn_{1/3})O_2$ prepared by the metal acetates decomposition method. *Electrochim. Acta* 2006, 51, 3731-3735.
116. Guo, R.; Shi, P. F.; Cheng, X. Q.; Du, C. Y., Synthesis and characterization of carbon-coated $Li(Ni_{1/3}Co_{1/3}Mn_{1/3})O_2$ cathode material prepared by polyvinyl alcohol pyrolysis route. *Journal of Alloys and Compounds* 2009, 473, 53-59.
117. Kim, S. K.; Jeong, W. T.; Lee, H. K.; Shim, J., Characteristics of $Li(Ni_{1/3}Co_{1/3}Mn_{1/3})O_2$ Cathode Powder Prepared by Different Method in Lithium Rechargeable Batteries. *International Journal of Electrochemical Science* 2008, 3, 1504-1511.
118. Cahill, L. S.; Yin, S. C.; Samoson, A.; Heinmaa, I.; Nazar, L. F.; Goward, G. R., Li-6 NMR studies of cation disorder and transition metal ordering in $Li(Ni_{1/3}Co_{1/3}Mn_{1/3})O_2$ using ultrafast magic angle spinning. *Chem. Mater.* 2005, 17, 6560-6566.
119. Idemoto, Y.; Matsui, T., Thermodynamic stability, crystal structure, and cathodic performance of $Li(Mn_{1/3}Co_{1/3}Ni_{1/3})O_2$ depend on the synthetic process and Li content. *Solid State Ionics* 2008, 179, 625-635.
120. Atkinson, H. V., Theries of normal grain growth in pure single phase systems. *Acta Metallurgica* 1988, 36, 469-491.
121. Weaire, D.; Rivier, N., Soap, cells and statistics-random patterns in 2 dimensions. *Contemporary Physics* 1984, 25, 59-99.
122. Alexander, L.; Klug, H. P., Determination of Crystallite Size with the X-Ray Spectrometer. *Journal of Applied Physics* 1950, 21, 137-142.
123. Sun, Y. K.; Myung, S. T.; Kim, M. H.; Prakash, J.; Amine, K., Synthesis and characterization of $Li[(Ni_{0.8}Co_{0.1}Mn_{0.1})_{(0.8)}(Ni_{0.5}Mn_{0.5})_{(0.2)}]O_2$ with the microscale core-

shell structure as the positive electrode material for lithium batteries. *Journal of the American Chemical Society* 2005, 127, 13411-13418.
124. Reimers, J. N.; Dahn, J. R.; Greedan, J. E.; Stager, C. V.; Liu, G.; Davidson, I.; Vonsacken, U., Spin glass behavior in the frustrated antiferromagnetic $LiNiO_2$. *Journal of Solid State Chemistry* 1993, 102, 542-552.
125. Ngala, J. K.; Chernova, N. A.; Ma, M.; Mamak, M.; Zavalij, P. Y.; Whittingham, M. S., The synthesis, characterization and electrochemical behavior of the layered $LiNi_{0.4}Mn_{0.4}Co_{0.2}O_2$ compound. *J. Mater. Chem.* 2004, 14, 214-220.
126. Kim, G. H.; Myung, S. T.; Bang, H. J.; Prakash, J.; Sun, Y. K., Synthesis and electrochemical properties of LiNi(1/3)Co(1/)3Mn((1/3-x))Mg-xO2-yFy via coprecipitation. *Electrochemical and Solid State Letters* 2004, 7, A477-A480.
127. Luo, X. F.; Wang, X. Y.; Liao, L.; Gamboa, S.; Sebastian, P. J., Synthesis and characterization of high tap-density layered $Li(Ni_{1/3}Co_{1/3}Mn_{1/3})O_2$ cathode material via hydroxide co-precipitation. *J. Power Sources* 2006, 158, 654-658.
128. Li, H.; Chen, G.; Zhang, B.; Xu, J., Advanced electrochemical performance of Li Ni(1/3-x)FexCo1/3Mn1/3 O-2 as cathode materials for lithium-ion battery. *Solid State Commun.* 2008, 146, 115-120.
129. Grigorova, E.; Mandzhukova, T. S.; Khristov, M.; Yoncheva, M.; Stoyanova, R.; Zhecheva, E., Soft mechanochemically assisted synthesis of nano-sized LiCoO(2) with a layered structure. *J. Mater. Sci.* 2011, 46, 7106-7113.
130. Delmas, C.; Menetrier, M.; Croguennec, L.; Saadoune, I.; Rougier, A.; Pouillerie, C.; Prado, G.; Grune, M.; Fournes, L., An overview of the Li(Ni,M)O-2 systems: syntheses, structures and properties. *Electrochim. Acta* 1999, 45, 243-253.
131. Jouybari, Y. H.; Asgari, S., Synthesis and electrochemical properties of LiNi(0.8)Co(0.2)O(2) nanopowders for lithium ion battery applications. *J. Power Sources* 2011, 196, 337-342.
132. Antolini, E., Effect of lithium doping on microstructure development and phase transition of CoO. *Nuovo Cimento Della Societa Italiana Di Fisica D-Condensed Matter Atomic Molecular and Chemical Physics Fluids Plasmas Biophysics* 1998, 20, 1735-1743.
133. Lifshitz, I. M.; Slyozov, V. V., The kinetics of precipitation from supersaturated solid solutions. *Journal of Physics and Chemistry of Solids* 1961, 19, 35-50.
134. Wagner, R. S.; Ellis, W. C., Vapor-Liquid-Solid mechanism of single crystal growth (New method growth catalysis from impurity whiker epitaxial large cystals) *Applied Physics Letters* 1964, 4, 89-&.
135. Hillert, M., On theory of normal and abnormal grain growth. *Acta Metallurgica* 1965, 13, 227-232.
136. Greenwood, G. W., The growth of dispersed precipitates in solutions. *Acta Metallurgica* 1956, 4, 243-248.
137. Higgins, G. T., Grain-boundary migration and grain growth. *Metal Science* 1974, 8, 143-50.
138. Huang, F.; Zhang, H. Z.; Banfield, J. F., Two-stage crystal-growth kinetics observed during hydrothermal coarsening of nanocrystalline ZnS. *Nano Letters* 2003, 3, 373-378.

139. Kisailus, D.; Choi, J. H.; Lange, F. F., GaN nanocrystals from oxygen and nitrogen-based precursors. *Journal of Crystal Growth* 2003, 249, 106-120.
140. Schoeman, B. J.; Sterte, J.; Otterstedt, J. E., Analysis of ther crystal growth of TPA-Silicalite-1. *Zeolites* 1994, 14, 568-575.
141. Dannenberg, R.; Stach, E.; Groza, J. R.; Dresser, B. J., TEM annealing study of normal grain growth in silver thin films. *Thin Solid Films* 2000, 379, 133-138.
142. Gil, F. X.; Rodriguez, D.; Planell, J. A., Grain growth kinetics of pure titanium. *Scripta Metallurgica Et Materialia* 1995, 33, 1361-1366.
143. Kirchner, H. O., Coarsening of grain boundary precipitates. *Metallurgical Transactions* 1971, 2, 2861.
144. Speight, M. V., Growth kinetics of grain boundary precipitates. *Acta Metallurgica* 1968, 16, 133-&.
145. Wagner, C., Theorie der alterung von niederschlagen dorch umlosen (Ostwald reifung). *Zeitschrift Fur Elektrochemie* 1961, 65, 581-591.
146. Wu, F.; Wang, M.; Su, Y.; Bao, L.; Chen, S., A novel method for synthesis of layered $LiNi_{1/3}Mn_{1/3}Co_{1/3}O_2$ as cathode material for lithium-ion battery. *J. Power Sources* 2010, 195, 2362-2367.
147. Lee, M. H.; Kang, Y. J.; Myung, S. T.; Sun, Y. K., Synthetic optimization of $LiNi_{1/3}Mn_{1/3}Co_{1/3}O_2$ via co-precipitation. *Electrochim. Acta* 2004, 50, 939-948.
148. Ding, Y.; Zhang, P.; Jiang, Y.; Gao, D., Effect of rare earth elements doping on structure and electrochemical properties of $LiNi_{1/3}Mn_{1/3}Co_{1/3}O_2$ for lithium-ion battery. *Solid State Ionics* 2007, 178, 967-971.
149. Guo, J.; Jiao, L. F.; Yuan, H.; Wang, L. Q.; Li, H. X.; Zhang, M.; Wang, Y. M., Effect of structural and electrochemical properties of different Cr-doped contents of $LiNi_{1/3}Mn_{1/3}Co_{1/3}O_2$. *Electrochim. Acta* 2006, 51, 6275-6280.
150. Xie, J.; Huang, X.; Zhu, Z.; Dai, J., Hydrothermal synthesis of $LiNi_{1/3}Co_{1/3}Mn_{1/3}O_2$ for lithium rechargeable batteries. *Ceramics International* 2010, 36, 2485-2487.
151. Venkateswara Rao, C.; Leela Mohana Reddy, A.; Ishikawa, Y.; Ajayan, P. M., $LiNi_{1/3}Co_{1/3}Mn_{1/3}O_2$–Graphene Composite as a Promising Cathode for Lithium-Ion Batteries. *ACS Applied Materials & Interfaces* 2011, 3, 2966-2972.
152. Guo, R.; Shi, P.; Cheng, X.; Du, C., Synthesis and characterization of carbon-coated $LiNi_{1/3}Co_{1/3}Mn_{1/3}O_2$cathode material prepared by polyvinyl alcohol pyrolysis route. *Journal of Alloys and Compounds* 2009, 473, 53-59.
153. Choi, J.; Manthiram, A., Investigation of the Irreversible Capacity Loss in the Layered $LiNi_{1/3}Mn_{1/3}Co_{1/3}O_2$Cathodes. *Electrochemical and solid-state letters* 2005, 8, C102-C105.
154. Kabi, S.; Ghosh, A., Microstructure of $LiMn_{1/3}Ni_{1/3}Co_{1/3}O_2$ cathode material for lithium ion battery: Dependence of crystal structure on calcination and heat-treatment temperature. *Mater. Res. Bull.* 2013, 48, 3405-3410.
155. Zhu, J.; Vo, T.; Li, D.; Lu, R.; Kinsinger, N. M.; Xiong, L.; Yan, Y.; Kisailus, D., Crystal Growth of $LiNi_{1/3}Co_{1/3}Mn_{1/3}O_2$ as a Cathode Material for High-Performance Lithium Ion Batteries. *Crystal Growth & Design* 2012, 12, 1118-1123.

156. Kim, J. M.; Chung, H. T., Role of transition metals in layered Li[Ni,Co,Mn]O2 under electrochemical operation. *Electrochim. Acta* 2004, 49, 3573-3580.
157. Wu, F.; Wang, M.; Su, Y.; Chen, S., Surface modification of Li $Co_{1/3}Ni_{1/3}Mn_{1/3}O_2$ with Y_2O_3 for lithium-ion battery. *J. Power Sources* 2009, 189, 743-747.
158. Gopukumar, S.; Chung, K. Y.; Kim, K. B., Novel synthesis of layered $LiN_{i1/2}Mn_{1/2}O_2$ as cathode material for lithium rechargeable cells. *Electrochim. Acta* 2004, 49, 803-810.
159. He, Y.-S.; Ma, Z.-F.; Liao, X.-Z.; Jiang, Y., Synthesis and characterization of submicron-sized $LiNi_{1/3}Co_{1/3}Mn_{1/3}O_2$ by a simple self-propagating solid-state metathesis method. *J. Power Sources* 2007, 163, 1053-1058.
160. Lan, Y.; Wang, X.; Zhang, J.; Zhang, J.; Wu, Z.; Zhang, Z., Preparation and characterization of carbon-coated $LiFePO_4$ cathode materials for lithium-ion batteries with resorcinol–formaldehyde polymer as carbon precursor. *Powder Technology* 2011, 212, 327-331.
161. Zhu, J.; Fiore, J.; Li, D.; Kinsinger, N. M.; Wang, Q.; DiMasi, E.; Guo, J.; Kisailus, D., Solvothermal Synthesis, Development, and Performance of $LiFePO_4$ Nanostructures. *Crystal Growth & Design* 2013, 13, 4659-4666.
162. Gao, P.; Li, Y. H.; Liu, H. D.; Pinto, J.; Jiang, X. F.; Yang, G., Improved High Rate Capacity and Lithium Diffusion Ability of $LiNi_{1/3}Co_{1/3}Mn_{1/3}O_2$ with Ordered Crystal Structure. *J. Electrochem. Soc.* 2012, 159, A506-A513.
163. Hsieh, C.-T.; Mo, C.-Y.; Chen, Y.-F.; Chung, Y.-J., Chemical-wet Synthesis and Electrochemistry of $LiNi_{1/3}Co_{1/3}Mn_{1/3}O_2$ Cathode Materials for Li-ion Batteries. *Electrochim. Acta* 2013, 106, 525-533.
164. Liu, X. H.; Zhong, L.; Huang, S.; Mao, S. X.; Zhu, T.; Huang, J. Y., Size-Dependent Fracture of Silicon Nanoparticles During Lithiation. *Acs Nano* 2012, 6, 1522-1531.
165. Ge, M.; Rong, J.; Fang, X.; Zhou, C., Porous Doped Silicon Nanowires for Lithium Ion Battery Anode with Long Cycle Life. *Nano Letters* 2012, 12, 2318-2323.
166. Bower, A. F.; Guduru, P. R.; Sethuraman, V. A., A finite strain model of stress, diffusion, plastic flow, and electrochemical reactions in a lithium-ion half-cell. *Journal of the Mechanics and Physics of Solids* 2011, 59, 804-828.
167. Shenouda, A. Y.; Liu, H. K., Studies on electrochemical behaviour of zinc-doped LiFePO4 for lithium battery positive electrode. *Journal of Alloys and Compounds* 2009, 477, 498-503.
168. Wohlfahrt-Mehrens, M.; Vogler, C.; Garche, J., Aging mechanisms of lithium cathode materials. *J. Power Sources* 2004, 127, 58-64.
169. Rydh, C. J.; Sandén, B. A., Energy analysis of batteries in photovoltaic systems. Part I: Performance and energy requirements. *Energy Convers. Manage.* 2005, 46, 1957-1979.
170. Padhi, A. K.; Nanjundaswamy, K. S.; Goodenough, J. B., Phospho-olivines as positive-electrode materials for rechargeable lithium batteries. *J. Electrochem. Soc.* 1997, 144, 1188-1194.

171. Kim, D.-K.; Park, H.-M.; Jung, S.-J.; Jeong, Y. U.; Lee, J.-H.; Kim, J.-J., Effect of synthesis conditions on the properties of LiFePO4 for secondary lithium batteries. *J. Power Sources* 2006, 159, 237-240.
172. Gu, Y.-H.; Zeng, C.-S.; Wu, H.-K.; Cui, H.-Z.; Huang, X.-W.; Liu, X.-B.; Wang, C.-L.; Yang, Z.-N.; Liu, H., Enhanced cycling performance and high energy density of LiFePO4 based lithium ion batteries. *Mater. Lett.* 2007, 61, 4700-4702.
173. Dominko, R.; Bele, M.; Gaberscek, M.; Remskar, M.; Hanzel, D.; Pejovnik, S.; Jamnik, J., Impact of the carbon coating thickness on the electrochemical performance of LiFePO4/C composites. *J. Electrochem. Soc.* 2005, 152, A607-A610.
174. Yang, M.-R.; Ke, W.-h.; Wu, S.-h., Improving electrochemical properties of lithium iron phosphate by addition of vanadium. *J. Power Sources* 2007, 165, 646-650.
175. Wang, D. Y.; Li, H.; Shi, S. Q.; Huang, X. J.; Chen, L. Q., Improving the rate performance of LiFePO4 by Fe-site doping. *Electrochim. Acta* 2005, 50, 2955-2958.
176. Liu, H.; Li, C.; Zhang, H. P.; Fu, L. J.; Wu, Y. P.; Wu, H. Q., Kinetic study on $LiFePO_4$/C nanocomposites synthesized by solid state technique. *J. Power Sources* 2006, 159, 717-720.
177. Kang, H.-C.; Jun, D.-K.; Jin, B.; Jin, E. M.; Park, K.-H.; Gu, H.-B.; Kim, K.-W., Optimized solid-state synthesis of $LiFePO_4$ cathode materials using ball-milling. *J. Power Sources* 2008, 179, 340-346.
178. Hsu, K.-F.; Tsay, S.-Y.; Hwang, B.-J., Synthesis and characterization of nano-sized $LiFePO_4$ cathode materials prepared by a citric acid-based sol-gel route. *J. Mater. Chem.* 2004, 14, 2690-2695.
179. Lee, M.-H.; Kim, T.-H.; Kim, Y. S.; Song, H.-K., Precipitation Revisited: Shape Control of $LiFePO_4$ Nanoparticles by Combinatorial Precipitation. *J. Phys. Chem. C* 2011, 115, 12255-12259.
180. Yang, H.; Wu, X.-L.; Cao, M.-H.; Guo, Y.-G., Solvothermal Synthesis of $LiFePO_4$ Hierarchically Dumbbell-Like Microstructures by Nanoplate Self-Assembly and Their Application as a Cathode Material in Lithium-Ion Batteries. *J. Phys. Chem. C* 2009, 113, 3345-3351.
181. Muraliganth, T.; Stroukoff, K. R.; Manthiram, A., Microwave-Solvothermal Synthesis of Nanostructured Li(2)MSiO(4)/C (M = Mn and Fe) Cathodes for Lithium-Ion Batteries. *Chem. Mater.* 2010, 22, 5754-5761.
182. Fey, G. T.-K.; Huang, K.-P.; Kao, H.-M.; Li, W.-H., A polyethylene glycol-assisted carbothermal reduction method to synthesize $LiFePO_4$ using industrial raw materials. *J. Power Sources* 2011, 196, 2810-2818.
183. Wang, L. N.; Zhang, Z. G.; Zhang, K. L., A simple, cheap soft synthesis routine for LiFeP04 using iron(III) raw material. *J. Power Sources* 2007, 167, 200-205.
184. Xu, Z.; Xu, L.; Lai, Q.; Ji, X., A PEG assisted sol–gel synthesis of $LiFePO_4$ as cathodic material for lithium ion cells. *Mater. Res. Bull.* 2007, 42, 883-891.
185. Lim, J.-S.; Kim, D.-H.; Mathew, V.; Ahn, D.-C.; Kim, J.-K., Synthesis of $LiFePO_4$ Nanoparticles by Solvothermal Process Using Various Polyol Media and Their Electrochemical Properties. *J. Nanosci. Nanotechno.* 2011, 11, 1451-1454.

186. Lu, Z.; Chen, H.; Robert, R.; Zhu, B. Y. X.; Deng, J.; Wu, L.; Chung, C. Y.; Grey, C. P., Citric Acid- and Ammonium-Mediated Morphological Transformations of Olivine $LiFePO_4$ Particles. *Chem. Mater.* 2011, 23, 2848-2859.
187. Rosenqvist, I. T., Formation of vivianite in holocene clay sediments. *Lithos* 1970, 3, 327-334.
188. Fagel, N.; Alleman, L. Y.; Granina, L.; Hatert, F.; Thamo-Bozso, E.; Cloots, R.; André, L., Vivianite formation and distribution in Lake Baikal sediments. *Global Planet. Change* 2005, 46, 315-336.
189. Ou, X.; Gu, H.; Wu, Y.; Lu, J.; Zheng, Y., Chemical and morphological transformation through hydrothermal process for $LiFePO_4$ preparation in organic-free system. *Electrochimica Acta* 2013, 96, 230-236.
190. Chen, J. J.; Whittingham, M. S., Hydrothermal synthesis of lithium iron phosphate. *Electrochem. Commun.* 2006, 8, 855-858.
191. Jaffar, S.; Nam, K. T.; Khademhosseini, A.; Xing, J.; Langer, R. S.; Belcher, A. M., Layer-by-Layer Surface Modification and Patterned Electrostatic Deposition of Quantum Dots. *Nano Letters* 2004, 4, 1421-1425.
192. Peng, C.; Thio, Y. S.; Gerhardt, R. A., Effect of Precursor-Layer Surface Charge on the Layer-by-Layer Assembly of Polyelectrolyte/Nanoparticle Multilayers. *Langmuir* 2011, 28, 84-91.
193. Wang, L.; Zhou, F.; Meng, Y. S.; Ceder, G., First-principles study of surface properties of $LiFePO_4$: Surface energy, structure, Wulff shape, and surface redox potential. *Phys. Rev. B* 2007, 76, 165435.
194. Fisher, C. A. J.; Islam, M. S., Surface structures and crystal morphologies of $LiFePO_4$: relevance to electrochemical behaviour. *J. Mater. Chem.* 2008, 18, 1209-1215.
195. Kanamura, K.; Koizumi, S.; Dokko, K., Hydrothermal synthesis of $LiFePO_4$; as a cathode material for lithium batteries. *J. Mater. Sci.* 2008, 43, 2138-2142.
196. Finnegan, M. P.; Zhang, H.; Banfield, J. F., Anatase Coarsening Kinetics under Hydrothermal Conditions As a Function of Ph and Temperature. *Chem. Mater.* 2008, 20, 3443-3449.
197. Xia, Y.; Zhang, W.; Huang, H.; Gan, Y.; Tian, J.; Tao, X., Self-assembled mesoporous $LiFePO_4$ with hierarchical spindle-like architectures for high-performance lithium-ion batteries. *J. Power Sources* 2011, 196, 5651-5658.
198. Wu, X.-L.; Jiang, L.-Y.; Cao, F.-F.; Guo, Y.-G.; Wan, L.-J., $LiFePO_4$ Nanoparticles Embedded in a Nanoporous Carbon Matrix: Superior Cathode Material for Electrochemical Energy-Storage Devices. *Advanced Materials* 2009, 21, 2710.
199. Yuan, L.-X.; Wang, Z.-H.; Zhang, W.-X.; Hu, X.-L.; Chen, J.-T.; Huang, Y.-H.; Goodenough, J. B., Development and challenges of $LiFePO_4$ cathode material for lithium-ion batteries. *Energy & Environmental Science* 2011, 4, 269-284.
200. Doeff, M. M.; Hu, Y. Q.; McLarnon, F.; Kostecki, R., Effect of surface carbon structure on the electrochemical performance of $LiFePO_4$. *Electrochemical and Solid State Letters* 2003, 6, A207-A209.
201. Belharouak, I.; Johnson, C.; Amine, K., Synthesis and electrochemical analysis of vapor-deposited carbon-coated $LiFePO_4$. *Electrochem. Commun.* 2005, 7, 983-988.

202. Chen, J.; Spear, S. K.; Huddleston, J. G.; Rogers, R. D., Polyethylene glycol and solutions of polyethylene glycol as green reaction media. *Green Chemistry* 2005, 7, 64-82.
203. Rho, Y.-H.; Nazar, L. F.; Perry, L.; Ryan, D., Surface chemistry of $LiFePO_4$ studied by mossbauer and X-ray photoelectron spectroscopy and its effect on electrochemical properties. *J. Electrochem. Soc.* 2007, 154, A283-A289.
204. Fan, M.; Liang, Y.; Zhou, F.; Liu, W., Dramatically improved friction reduction and wear resistance by in situ formed ionic liquids. *Rsc Advances* 2012, 2, 6824-6830.
205. Ferrari, A. C., Raman spectroscopy of graphene and graphite: Disorder, electron–phonon coupling, doping and nonadiabatic effects. *Solid State Commun.* 2007, 143, 47-57.
206. Goli, P.; Legedza, S.; Dhar, A.; Salgado, R.; Renteria, J.; Balandin, A. A., Graphene-enhanced hybrid phase change materials for thermal management of Li-ion batteries. *J. Power Sources* 2014, 248, 37-43.
207. Shahil, K. M. F.; Balandin, A. A., Thermal properties of graphene and multilayer graphene: Applications in thermal interface materials. *Solid State Commun.* 2012, 152, 1331-1340.
208. Balandin, A. A.; Ghosh, S.; Bao, W.; Calizo, I.; Teweldebrhan, D.; Miao, F.; Lau, C. N., Superior thermal conductivity of single-layer graphene. *Nano Letters* 2008, 8, 902-907.
209. Calizo, I.; Balandin, A. A.; Bao, W.; Miao, F.; Lau, C. N., Temperature dependence of the Raman spectra of graphene and graphene multilayers. *Nano Letters* 2007, 7, 2645-2649.
210. Guo, S.; Ghazinejad, M.; Qin, X.; Sun, H.; Wang, W.; Zaera, F.; Ozkan, M.; Ozkan, C. S., Tuning Electron Transport in Graphene‐Based Field‐Effect Devices using Block Co‐polymers. *Small* 2012.
211. Guo, S.; Wang, W.; Ozkan, C. S.; Ozkan, M., Assembled graphene oxide and single-walled carbon nanotube ink for stable supercapacitors. *Journal of Materials Research* 2013, 28, 918-926.
212. Wang, W.; Guo, S.; Bozhilov, K. N.; Yan, D.; Ozkan, M.; Ozkan, C. S., Intertwined Nanocarbon and Manganese Oxide Hybrid Foam for High‐Energy Supercapacitors. *Small* 2013, 9, 3714-3721.
213. Ferrari, A. C.; Basko, D. M., Raman spectroscopy as a versatile tool for studying the properties of graphene. *Nature Nanotechnology* 2013, 8, 235-246.
214. Wood, B. J.; Wise, H., Reaction kinetics of gaseous hydrogen atoms with graphite. *The Journal of Physical Chemistry* 1969, 73, 1348-1351.
215. Zaghib, K.; Dontigny, M.; Charest, P.; Labrecque, J. F.; Guerfi, A.; Kopec, M.; Mauger, A.; Gendron, F.; Julien, C. M., Aging of $LiFePO_4$ upon exposure to H_2O. *J. Power Sources* 2008, 185, 698-710.
216. Gangulibabu; Kalaiselvi, N.; Bhuvaneswari, D.; Doh, C. H., On the Synergistic Effect of Carbonate Anion Directed Shape Controlled Morphology and Super P Carbon in Preparing $LiFePO_4$/C Cathode With Improved Lithium Intercalation Behavior. *International Journal of Electrochemical Science* 2010, 5, 1597-1604.

217. Lin, Y.; Gao, M. X.; Zhu, D.; Liu, Y. F.; Pan, H. G., Effects of carbon coating and iron phosphides on the electrochemical properties of $LiFePO_4$/C. *J. Power Sources* 2008, 184, 444-448.
218. Hong, S.-A.; Kim, S. J.; Kim, J.; Lee, B. G.; Chung, K. Y.; Lee, Y.-W., Carbon coating on lithium iron phosphate ($LiFePO_4$): Comparison between continuous supercritical hydrothermal method and solid-state method. *Chemical Engineering Journal* 2012, 198, 318-326.